INTEGRATION OF ARSENIC TRISULFIDE AND

TITANIUM DIFFUSED LITHIUM NIOBATE WAVEGUIDES

A Dissertation

by

MEHMET ERTUGRUL SOLMAZ

Submitted to the Office of Graduate Studies of
Texas A&M University
in partial fulfillment of the requirements for the degree of

DOCTOR OF PHILOSOPHY

May 2010

Major Subject: Electrical Engineering

INTEGRATION OF ARSENIC TRISULFIDE AND

TITANIUM DIFFUSED LITHIUM NIOBATE WAVEGUIDES

A Dissertation

by

MEHMET ERTUGRUL SOLMAZ

Submitted to the Office of Graduate Studies of
Texas A&M University
in partial fulfillment of the requirements for the degree of

DOCTOR OF PHILOSOPHY

Approved by:

Chair of Committee,	Christi K. Madsen
Committee Members,	Ohannes Eknoyan
	Robert Nevels
	Alvin Yeh
Head of Department,	Costas Georghiades

May 2010

Major Subject: Electrical Engineering

ABSTRACT

Integration of Arsenic Trisulfide and Titanium Diffused

Lithium Niobate Waveguides. (May 2010)

Mehmet Ertugrul Solmaz, B.S., Sabanci University, Istanbul-Turkey

Chair of Advisory Committee: Dr. Christi K. Madsen

A chalcogenide glass (arsenic-trisulfide, As_2S_3) optical waveguide is vertically integrated onto titanium-diffused lithium-niobate ($Ti:LiNbO_3$) waveguides to add optical feedback paths and to create more compact optical circuits. Lithium-niobate waveguides are commonly used as building blocks for phase and amplitude modulators in high speed fiber communication networks due to its high electrooptic coefficient and low mode coupling loss to single-mode optical fibers. Although it can easily be modulated using an RF signal to create optical modulators, it lacks the intrinsic trait to create optical feedback loops due to its low core-to-cladding index contrast. Ring resonators are main building blocks of many chip-scale optical filters that require these feedback loops and are already demonstrated with other material systems. We have, for the first time, incorporated As_2S_3 as a guiding material on $Ti:LiNbO_3$ and fabricated s-bends and ring resonators. We have examined As_2S_3-on-$Ti:LiNbO_3$ waveguides at simulation, microfabrication, and optical characterization levels.

To my family

ACKNOWLEDGEMENTS

TABLE OF CONTENTS

LIST OF FIGURES

FIGURE   Page

LIST OF TABLES

CHAPTER I

INTRODUCTION

1.1   Background

Optics is a key science for 21st century that has an impact on our daily lives. Cameras, barcode scanners, DVD players, and optical disks are few recognizable consumer products that take advantage of basic optical phenomena such as diffraction, reflection, and interference. Although not at the consumer end, optical systems also serve everyday needs for data transmission over long distances, i.e. fiber optic communication networks. The invention of fiber optic cable in the 1970s and fiber amplifiers in the 1980s led to high data rate long distance communications. Many independent signals are propagated at enormously high speeds without interfering with each other. The electric signal is converted to an optical signal which is transmitted over a distance in a fiber optic cable before being converted back to electrical in order to further process it at the receiver end. High speed optical signal generators (lasers, modulators) and detectors are designed to meet the increase data demand, but are still not enough.

The research on integrated optics started out to meet redundant telecommunication system's needs to minimize the size and increase the functionality of optical systems. Integrated optics or microphotonics has an advantage over systems based solely on either bulk or fiber optics. The purpose of microphotonic circuits is to integrate several active and passive components onto the same monolithic chip. Some

_____
This dissertation follows the format of *IEEE Journal of Lightwave Technology.*

passive optical components are power splitters, reflectors, polarizers, switches, and bends. On the other side, active components include lasers, modulators, amplifiers, and non-linear frequency converters. Optical waveguides are key passive components of integrated optical systems as the light is confined in their core with respect to their claddings. They are fabricated on a variety of substrates such as silicon, silica, silicon nitride, III-V elements, and $LiNbO_3$. $LiNbO_3$, which is a ferroelectric material, possesses s relatively large electro-optic coefficient that is advantageous if the application needs much faster modulation or tuning speeds. All the semiconductor waveguides, on the other hand, are thermally tuned except some III-V materials such as GaAs and InP that possess significant Pockel's effect. $LiNbO_3$ is still the substrate of choice for amplitude and phase modulators to be used in telecommunication applications. In 2007, lithium-niobate held 33.8% of the market share for external modulators [1] and research on this unique material has steadily continued since its introduction in 1970s as a possible waveguide material. Semiconductor waveguides have some advantages over its ferroelectric counterparts. They are easily integrated with electronic ICs and can perform distinct filtering functions that $LiNbO_3$ cannot achieve. The most well known characteristic of semiconductor waveguides are their much smaller size and high core confinement dependent on the design compared to $LiNbO_3$ waveguides. Since the light is much more confined in a much smaller area, less loss is induced around tight bending structures [2-3]. For instance, feedback filters requires creating 180° and 360° bends as opposed to feed-forward filters that can be fabricated with very small S-shaped bent

waveguides (Fig. 1.1). The distinct materials and various design core-to-cladding refractive index difference or contrast are extracted from several references in Table 1.
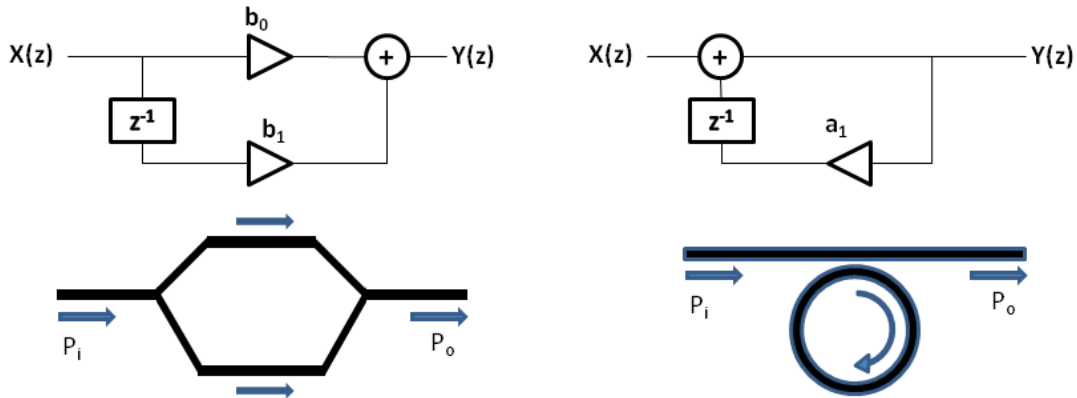
Figure 1.1. Illustration of feed-back and feed-forward filters in the digital (top) and the optical domain (bottom), a) Mach-Zehnder Interferometer; b) Single-stage optical ring resonator.

Table 1.1. Index contrast and waveguide dimensions as figures of merit.

	Silicon, [4]	Ge-SiO$_2$, [5]	Si$_x$N$_y$, [6]	III-V, [7]	LiNbO$_3$, [8]	Polymer, [9]
Index Contrast	~60%	3.5%	~30%	~70%	<0.03%	~10%
Waveguide size	<1µm	~3µm	~0.6x1µm	0.45x2µm	~8-10µm	<3µm

1.2   Motivation

All the materials listed above have intrinsic ability to support bent modes of tight structures with the exception of LiNbO$_3$. Several centimeters of bend radii are needed for a titanium diffused waveguide ring resonator to function properly [10]. Changing the source of dopant to protons (H$^+$) yields higher index waveguides but not enough to create sub-centimeter bent structures [11]. Other researchers also

incorporated two different dopants to achieve millimeter scale bends [12]. Yet recent research showed promise to solve this problem and still take advantage of the electro-optic effect. Further etching after diffusion to create rib waveguides and re-deposition of $LiNbO_3$ waveguide material to create a better index contrast have recently been explored [13-14]. While not as a waveguiding region, blanket chalcogenide glasses on top of $LiNbO_3$ have been investigated as a means to modify the mode profile for phase tuning couplers [15], and grating structures [16]. Chalcogenide glasses as a superimposed bent waveguide on $LiNbO_3$ was never studied, even though the possibility of using these interesting materials on $LiNbO_3$ was established a long time ago. The following dissertation explores this possibility and demonstrates how we can compensate for the biggest drawback of $Ti:LiNbO_3$ waveguides, which is to support micrometer-scale bent structures.

1.3 Organization of Thesis

This dissertation is on the development of As_2S_3-on-$Ti:LiNbO_3$ waveguides for microphotonic applications and is organized in four chapters. Development includes extensive work on waveguide device and photomask design, optimization of fabrication processes (deposition, lithography, dry etching), materials characterization, and efficient optical testing methods.

Chapter I is the introduction and motivation to the research presented in this dissertation.

Chapter II gives the basic theory behind As_2S_3-on-Ti:LiNbO$_3$ waveguides for the purpose of preparing the reader to chapters afterwards. The theory includes solving optical waveguides using Maxwell equations, power coupling between waveguides, bent waveguide modes, basic ring resonator equations, and optical measurement setups. Although this chapter is a compilation of theory, it still presents some simulation results that are unique and key to understand the whole thesis.

Chapter III presents our fabrication process development of As_2S_3-on-Ti:LiNbO$_3$ waveguides. Although titanium diffused waveguides had already been established in our research lab, we had to improve key qualities in order to easily integrate As_2S_3 on top of it. The most important aspect of fabrication is fabrication low-loss, highly confined As_2S_3 waveguides, and the process parameters had to be developed and optimized over time.

Chapter IV is a compilation of both simulation and fabrication results. As_2S_3-on-Ti:LiNbO$_3$ S-shaped bends and ring resonators are successfully fabricated and the results are presented. Furthermore, more in depth analysis of the taper structure is given to support and compare to fabricated results.

Chapter V is the conclusion remarks to the research presented in this dissertation.

CHAPTER II

THEORETICAL REVIEW

This chapter summarizes the basic theory of As_2S_3-on-Ti:$LiNbO_3$ waveguides. Starting with Maxwell's equations, the solutions to ridge (As_2S_3) and diffused (Ti:$LiNbO_3$) waveguides are given, and the mode transfer between the waveguides are explained on the basis of coupled-mode theory and its interpretation with the taper structure. 2D and 3D simulations have been applied to show the mode transfer phenomena.

2.1   Wave Theory of As_2S_3-on-Ti:$LiNbO_3$ Waveguides

The differential form of Maxwell's equations are written in terms of the electric (**E,** V/m) and magnetic (**H,** A/m) fields in homogeneous, source-free and lossless dielectric medium [17]

$$\nabla \times \boldsymbol{E} = -\mu \frac{\partial \boldsymbol{H}}{\partial t} \tag{2.1}$$

$$\nabla \times \boldsymbol{H} = \mathbf{J} + \varepsilon \frac{\partial \boldsymbol{E}}{\partial t} \tag{2.2}$$

$$\nabla . \boldsymbol{D} = \rho \tag{2.3}$$

$$\nabla . \boldsymbol{B} = 0 \tag{2.4}$$

where ε and μ denote the permittivity and permeability of the medium. **J**=0 and ρ=0 in mediums free of sources. **D**=ε_0**E**+**P** is displacement or electric flux density where **P** is the polarization; **B**=μ_0**H**+**M** is the magnetic flux density and **M** is magnetization. ε and μ are

related to their respective values in vacuum ε_0=8.854x10^{-12} [F/m] and μ_0=4π x 10^{-7}

[H/m] by

$$\varepsilon = \varepsilon_0 n^2 \qquad (2.5)$$

$$\mu = \mu_0 \qquad (2.6)$$

where n is the refractive index.

It is noticeable that the electric field and magnetic field in equations (2.1) and

(2.2), i.e., Faraday's law and Ampere's law, are tied to each other. If we get the curl of

(2.1), and incorporate (2.2), we can proceed as follows:

$$\nabla \times \nabla \times \boldsymbol{E} = \nabla \times \left(\mu_0 \frac{\partial \boldsymbol{H}}{\partial t}\right)$$
$$= \mu_0 \frac{\partial}{\partial t}(\nabla \times \boldsymbol{H})$$
$$= \mu_0 \frac{\partial}{\partial t}\left(\varepsilon_0 n^2 \frac{\partial \boldsymbol{E}}{\partial t}\right)$$
$$= \mu_0 \, \varepsilon_0 n^2 \frac{\partial^2 \boldsymbol{E}}{\partial t^2} \, . \qquad (2.7)$$

Using the equality, $\nabla \times \nabla \times \boldsymbol{A} = \nabla(\nabla \cdot \boldsymbol{A}) - \nabla^2 \boldsymbol{A}$, $c = \frac{1}{\sqrt{\varepsilon_0 \mu_0}}$, and the equation (2.3,

$\nabla \cdot \boldsymbol{E} = 0$), the wave equation becomes

$$\nabla^2 \boldsymbol{E} - \frac{n^2}{c^2}\frac{\partial^2 \boldsymbol{E}}{\partial t^2} = 0. \qquad (2.8)$$

We can do the same procedure for equation (2.2) and arrive at

$$\nabla^2 \boldsymbol{H} - \frac{n^2}{c^2}\frac{\partial^2 \boldsymbol{H}}{\partial t^2} = 0. \qquad (2.9)$$

Equations (2.8) and (2.9) are also known as Helmholtz equations. Optical field

solutions are harmonic fields that vary sinusoidally in time. For simplicity, let the

electromagnetic wave be composed of single frequency and the harmonic field be

represented by complex fields. We define the space and time dependent field propagating in *z* direction with propagation constant β as follows

$$E(\mathbf{r},\mathrm{t}) = E(\mathbf{r})e^{j(\beta z - wt)} .$$ (2.10)

Rewriting equations (2.8) and (2.9), and replacing $k = \frac{w \cdot n}{c}$, we get

$$\nabla^2 E + (\mathrm{k}^2 - \beta^2)E = 0$$ (2.11)

$$\nabla^2 H + (\mathrm{k}^2 - \beta^2)H = 0.$$ (2.12)

2.1.1 Step-index Slab Waveguides

Solving equations (2.11) and (2.12) for a simple slab waveguide (Fig. 2.1) will give us the basic equations, and the guided mode conditions will be obtained. *E* and *H* have *x*, *y*, *z* components and a solution should involve E_x, E_y, E_z, H_x, H_y, H_z in order to be valid.
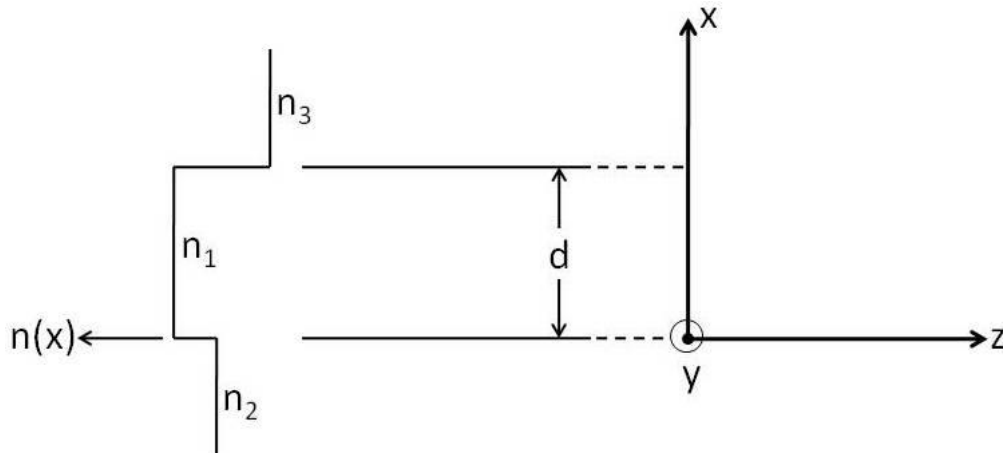
Figure 2.1. Step-index planar waveguide.

In the z-propagating slab waveguide, the fields **E** and **H** do not have y and z dependency due to no boundaries. For transverse-electric (TE) modes of a planar waveguide, E_z=0, and E_x=H_y=0 due to $\frac{\partial H_z}{\partial y} = 0$. So, equation (2.11) becomes

$$\frac{\partial^2 E_y}{\partial x^2} + (k^2 - \beta^2)E_y = 0 \tag{2.13}$$

H_x and H_z can be obtained using equations (2.1) and (2.2), in terms of E_y

$$H_x = -\frac{\beta}{\omega\mu}E_y \tag{2.14}$$

$$H_z = -\frac{1}{i\omega\mu}\frac{\partial E_y}{\partial x} \tag{2.15}$$

For transverse-magnetic (TM) modes of a planar waveguide, H_z=0, and H_x=E_y=0 due to, $\frac{\partial E_z}{\partial y} = 0$. So equation (2.12) becomes

$$\frac{\partial^2 H_y}{\partial x^2} + (k^2 - \beta^2)H_y = 0 \tag{2.16}$$

E_x and E_z can be obtained using equations (2.1) and (2.2), in terms of H_y

$$E_x = \frac{\beta}{\omega\varepsilon}H_y \tag{2.17}$$

$$E_z = \frac{1}{i\omega\varepsilon}\frac{\partial H_y}{\partial x} \tag{2.18}$$

For a slab waveguide, solving E_y for TE and H_y for TM is convenient, i.e. equations (2.13) and (2.16) respectively. For TE mode, E_y, H_x , and H_z are continuous at the interfaces x=±d/2. Since n_1>n_2>n_3, we can define h_1, γ_2, and γ_3 as follows

$$h_1 = \sqrt{k_1^2 - \beta^2} \tag{2.19}$$

$$\gamma_2 = \sqrt{\beta^2 - k_2{}^2} \qquad\qquad (2.20)$$

$$\gamma_3 = \sqrt{\beta^2 - k_3{}^2} \qquad\qquad (2.21)$$

$\gamma's$ are the attenuation coefficients in while h_1 is the transverse wavevector. $\beta = \frac{2\pi n_{eff}}{\lambda}$

where n_{eff} is the effective refractive index of a guided mode corresponding to β. For a

guided mode, we have $k_1 > \beta > k_2 > k_3$ or $n_1 > n_{eff} > n_2 > n_3$. The solution to (2.13) can be

written as follows

$$E_y = C \begin{cases} \cos\left(\frac{h_1 d}{2} - \phi\right) e^{\left[\gamma_3\left(\frac{d}{2}-x\right)\right]}, \text{x > d/2,} \\ \cos(h_1 x - \phi), \text{-d/2 < x < d/2,} \\ \cos\left(\frac{h_1 d}{2} + \phi\right) e^{\left[\gamma_2\left(\frac{d}{2}+x\right)\right]}, \text{x < -d/2} \end{cases} \qquad (2.22)$$

where ϕ is the phase shift associated with the reflections at the boundaries. The

electric field E_y and the magnetic field H_z should both be continuous at x=±d/2

according to the boundary conditions. Using equations (2.15) and (2.22), we can obtain

$$\tan(h_1 d + \phi) = \frac{\gamma_3}{h_1} \qquad\qquad (2.23)$$

$$\tan(h_1 d - \phi) = \frac{\gamma_2}{h_1} \, . \qquad\qquad (2.24)$$

And from equations (2.23) and (2.24), the eigenvalue equations are written as

$$\tan(h_1 d) = \frac{h_1(\gamma_2 + \gamma_3)}{h_1^2 - \gamma_2\gamma_3} \qquad\qquad (2.25a)$$

$$\tan(2\phi) = \frac{h_1(\gamma_2 - \gamma_3)}{h_1^2 + \gamma_2\gamma_3}. \qquad\qquad (2.25b)$$

Solving the first eigenvalue equation provides us with n_{eff} and hence β, which in

turn lets us plot electric field. Finding the roots of equation (2.25a) can be done

numerically. Another easy way of solving for n_{eff} is to use a graphical approach where both sides of the eigenvalue equation are plotted for values of h_i and the crossing points are determined (Fig. 2.2).
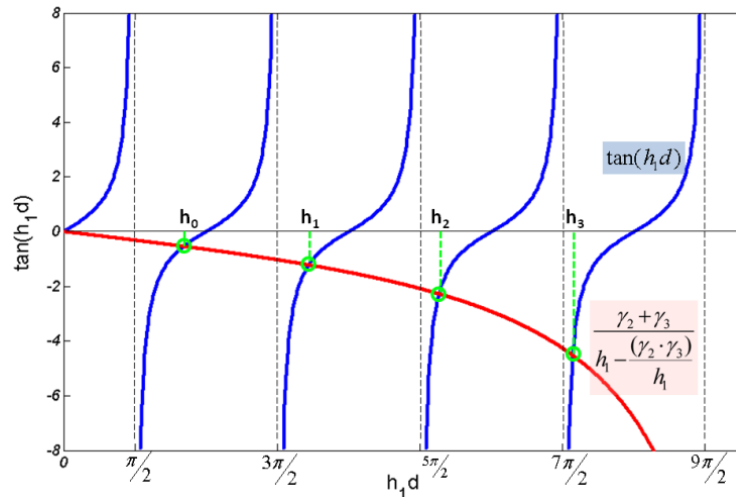
Figure 2.2. Both sides of the eigenvalue equation are plotted and the crossing points are identified.

Although the graph for tangent side never changes, the right side may change according to the waveguide dimensions and refractive indices. After finding the corresponding n_{eff} values for optical modes of different orders, one can use equation (2.22) and plot the electric field for guided modes (Fig. 2.3).
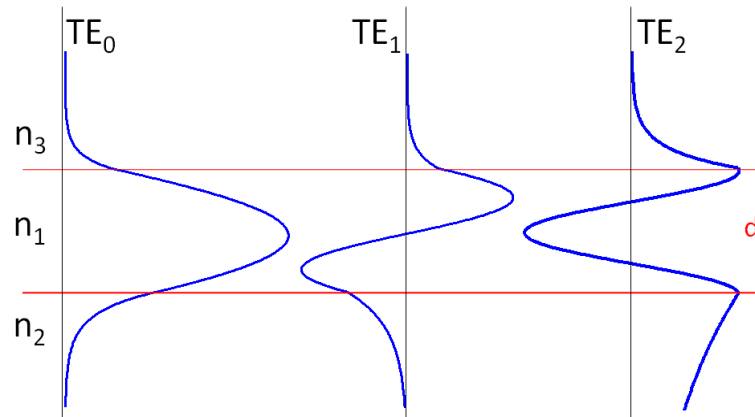
Figure 2.3. Optical electric field distributions for first three TE modes of an asymmetric slab waveguide.

The optical mode experiences an exponential decay after the boundaries in the cladding regions. Since $n_2 > n_3$, there is even a sharper roll-off in the region with the lowest refractive index, which indicates an asymmetric waveguide. The TE field components H_x and H_z can be plotted using E_y accordingly. As for TM polarization, H_y, after solving the eigenvalue equation, can be used to plot E_x and E_z.

The time average power is written as

$$P = \iint_S \frac{1}{2}(\overline{E} \times \overline{H^*}) \cdot \overline{u}_z \, ds \tag{2.26}$$

where *ds* represents a differential surface of the power flow. The power confinement factor (Γ) indicates the amount of power that is present in the core at a given time. If the total power in a waveguide is the sum of core (P_{core}) and cladding (P_{clad1}, P_{clad2}) powers, the confinement factor can be written as

$$\Gamma = \frac{P_{core}}{P_{core} + P_{clad\ 1} + P_{clad\ 2}} \tag{2.27}$$

2.1.2   Rectanguler Shaped Waveguides

Planar waveguides are not used in practical applications due to the infinite extent along y direction. Rectangular shaped waveguides (Fig. 2.4) are preferred since the optical mode is confined at all boundaries and there is no leakage if the waveguides are bent to slightly steer the optical mode and change its direction. As_2S_3 waveguides fabricated in our facilities are indeed of rectangular shape after etching the excessive film on the sides. The waveguides have step-index profile. The equations we derived for slab waveguides can be used to analytically solve effective indices of the optical modes in step-index rectangular shaped optical waveguides. The basic method to solve a 3D waveguide is called the effective index method where the original waveguide is divided into two 2D waveguides (Fig. 2.4).
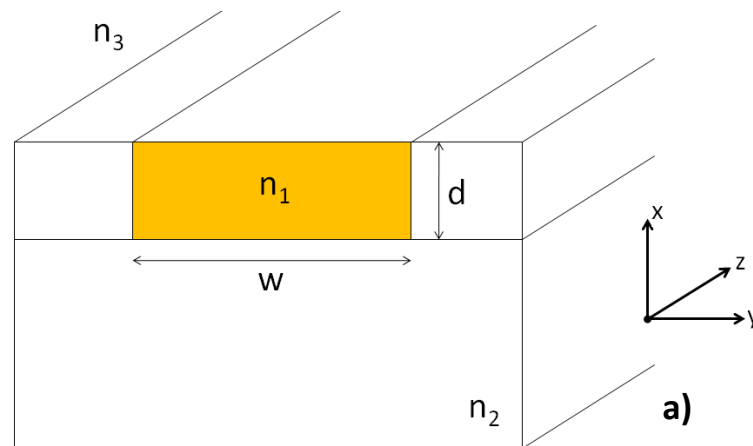
Figure 2.4. a) 3D view of rectangular waveguide; n_2 and n_3 are cladding refractive indices; b) 2D slab waveguide in vertical direction; c) 2D slab waveguide with core effective index N_1 derived from first 2D waveguide.
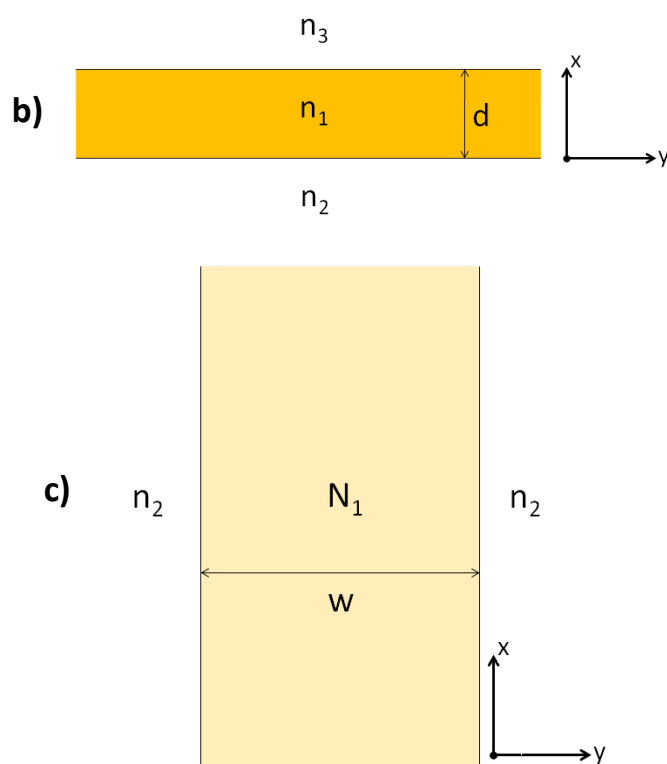
Figure 2.4. Continued.

The starting waveguide is covered with second cladding (n_2) from left, right and bottom while upper cladding has a refractive index of n_3. The solved modes have specific mode indices, *m* and *n*, that define the order of modes polarized in x and y direction respectively. After choosing the specific mode, TE_{mn} or TM_{mn}, the waveguide where the light confinement is in the x direction is solved for effective index N_1 (Fig. 2.4.b). The second planar waveguide sees N_1 as the index of the guiding layer (Fig. 2.4.c) and the final effective index of the desired mode is found. The waveguide mode with its dominant electric field component in the y direction is called TE while the one with its electric field direction mostly in the x direction is called TM mode.

Although the effective index method is a fast way of determining if a ridge shaped waveguide supports the desired mode, it is rather inaccurate to be used in waveguides of real applications. Commercial softwares are available to calculate and plot mode profiles of interest with great accuracy and speed. The software package (Fimmwave) from Photon Design Inc. is used for simulations presented in this dissertation [18].

As_2S_3 has a higher refractive index than bulk $LiNbO_3$ and this can easily be seen in the refractive index plot (Fig. 2.5). Due to the birefringence of $LiNbO_3$, there is ~0.07 index difference between ordinary and extraordinary indices at 1550nm. The refractive index of As_2S_3 is taken from [19] and is close to the manufacturer's bulk value of 2.43. It is essential to note that the refractive index of deposited As_2S_3 thin film is different from the bulk index. Assuming chalcogenide glass does not have a cladding layer and sits on top of $LiNbO_3$, the 2D intensity profile of a 3μm wide 0.45μm thick waveguide can be obtained for TE_{11} and TM_{11} modes (Fig. 2.6).
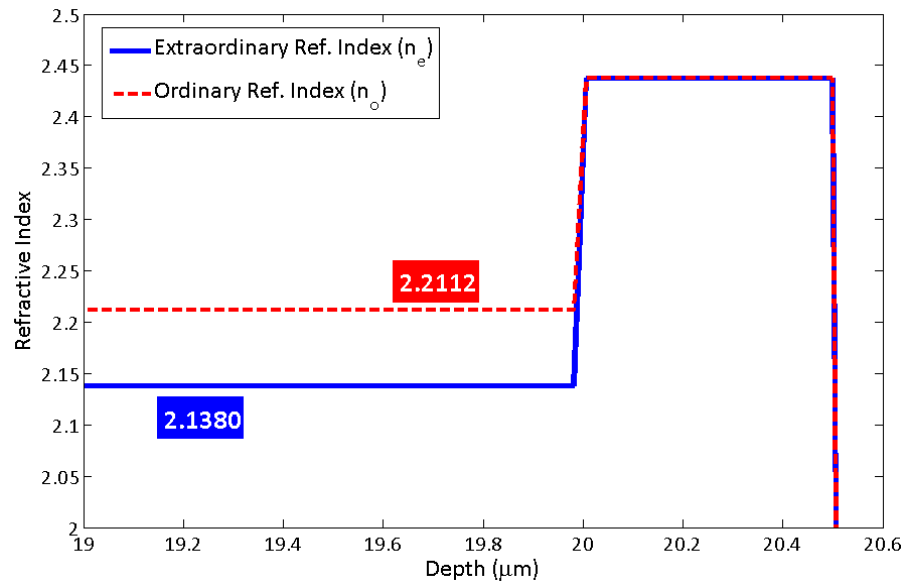
Figure 2.5. Refractive index profile of As$_2$S$_3$ on x-cut y-propagating LiNbO$_3$.
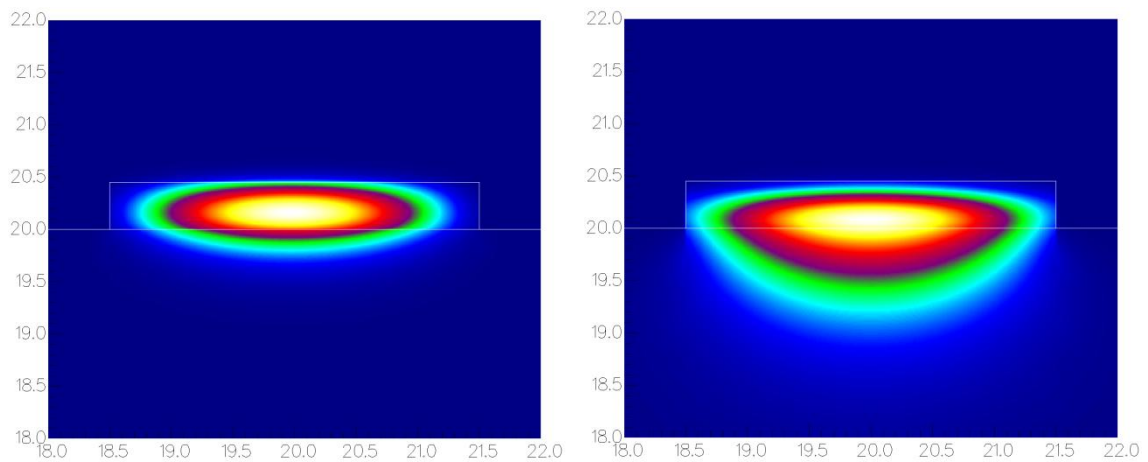
Figure 2.6. Intensity profiles of As$_2$S$_3$ (3x0.45μm) on LiNbO$_3$ substrate. a) TE$_{11}$ polarization; b) TM$_{11}$ polarization.

The confinement factor of TE$_{11}$ mode is 65% while TM$_{11}$ mode has 29.5% confinement in the same waveguide. It is necessary to obtain a thicker waveguide for TM polarization to have the same amount of confinement as TE polarization.

Waveguide thickness has a significant impact on the mode confinement while increasing waveguide width does not affect it after some time as it saturates at larger widths (Fig. 2.7).
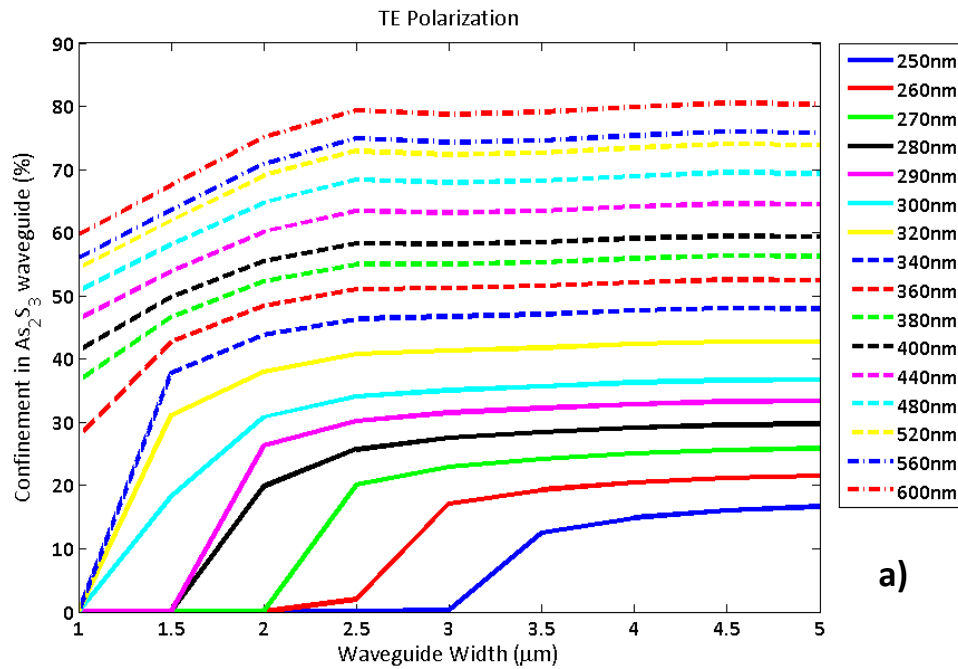
Figure 2.7. Mode intensity confinements for several waveguide heights. a) TE_{11}; b) TM_{11}.
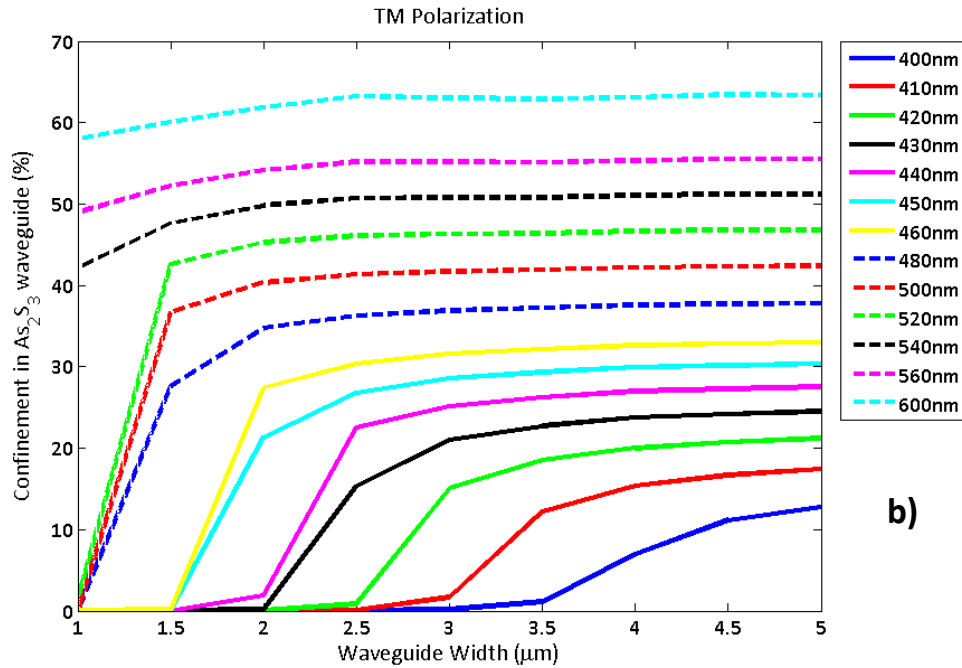
Figure 2.7. Continued.

2.1.3 Graded-index Waveguides

While most practical waveguides have step-index nature, some waveguides have varying refractive index along vertical and horizontal directions. Titanium diffused lithium-niobate waveguides (Ti:LiNbO$_3$) are a good example of this kind of waveguides. When diffusion takes place, titanium atoms penetrate into LiNbO$_3$ and create a refractive index gradient (Fig. 2.8). Assuming anisotropic diffusion, the two-dimensional concentration profile of an x-cut y-propagating waveguide can be written as

$$c(x, z) = c_0 \cdot f(x) \cdot g(z) \tag{2.28}$$

where f(x) is a Gaussian and g(z) is an Error (erf) function in Ti:LiNbO$_3$ waveguides [20].
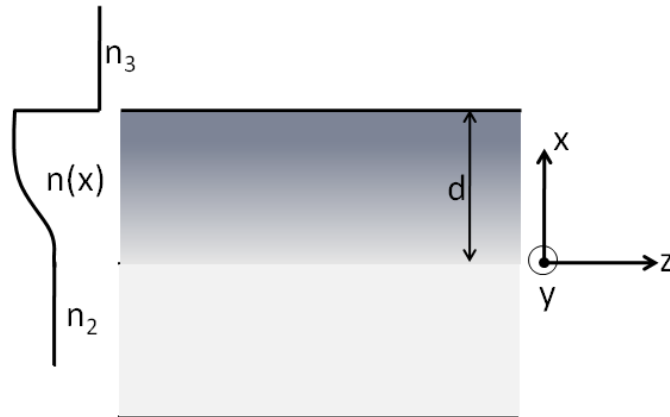
Figure 2.8. Index distribution of a graded index waveguide along vertical x direction.

Instead of equation 2.13, the wave equation for a polarization along z axis is written as

$$\left(\frac{\partial^2}{\partial x^2}+\frac{\partial^2}{\partial z^2}\right)E_z + (k_0{}^2 n^2(x,z) - \beta^2)E_z = 0 \tag{2.29}$$

by including the change in 2D refractive index. Refractive index has x and z dependence since titanium diffuses both vertically and horizontally and anisotropy introduces different vertical and lateral diffusion coefficients. The refractive index can be written as

$$n(x,z) = n_s + \Delta n \cdot f(x) \cdot g(z) \tag{2.30}$$

where Δn is maximum index change, and f(x) and g(z) come from concentration profile. Both functions have minimum and maximum limits of 0 and 1. Assuming a surface index change of ~10^{-3} after titanium diffusion and incorporating equations 2.28 and 2.30, it is possible to plot refractive index profile of a TE polarized modes in Ti:LiNbO$_3$ waveguides (Fig. 2.9). The bulk refractive index of LiNbO$_3$ is 2.138 at the wavelength of 1550nm for extraordinary refractive index in z-direction as per Fig.2.8.
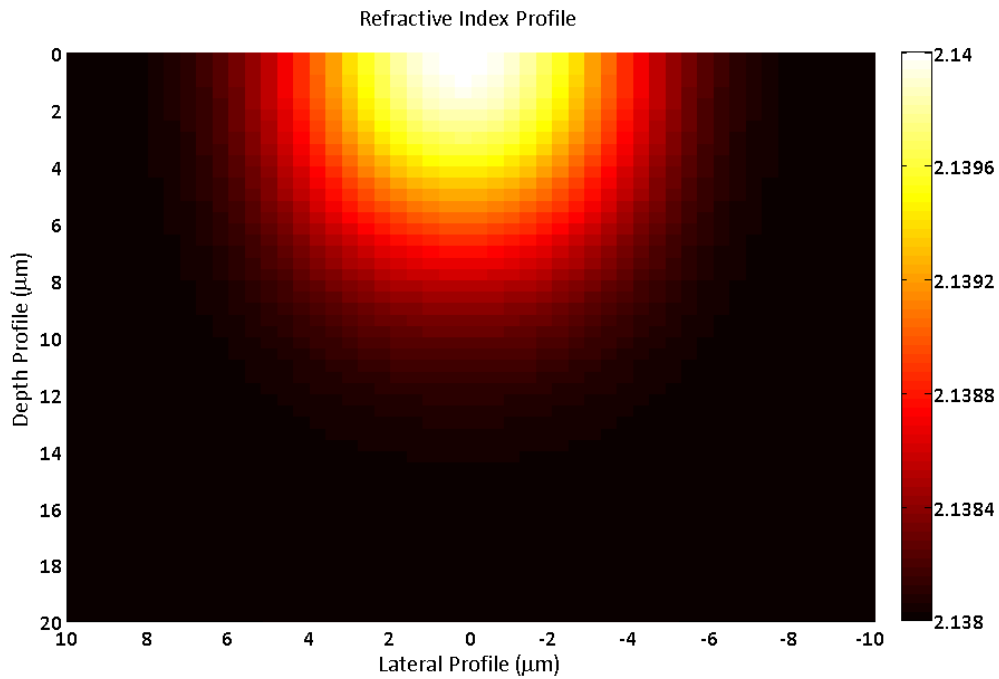
Figure 2.9. Refractive index profile of LiNbO$_3$ after Ti diffusion.

The maximum refractive index is on the surface and the optical mode is contained inside the diffusion region. It is necessary to introduce boundaries to a diffused waveguide in order to solve the wave equation and this always introduces a small inaccuracy. The optical ray in a step-index waveguide reflects off of the boundaries at constant angles on a straight path whereas the critical angle (θ_c) of a ray in a diffused waveguide changes along the depth (Fig. 2.10).
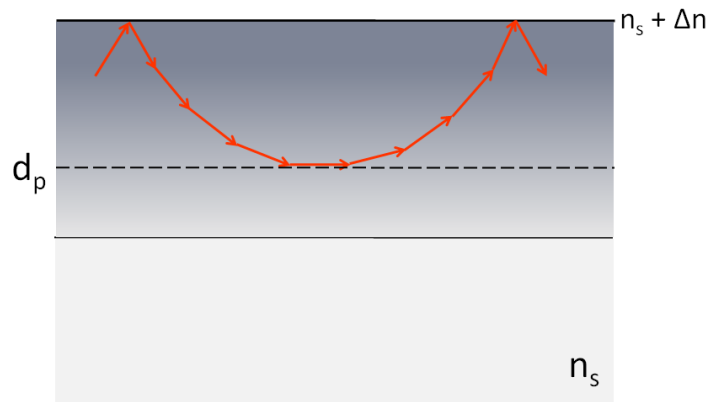
Figure 2.10. The trace of the optical ray in a diffused waveguide.

The depth (d_p) is where the incoming wave is totally reflected, which occurs before the diffusion depth. The equation 2.29 can be solved using a commercial software and the first order TE and TM modes can be plotted (Fig. 2.11).
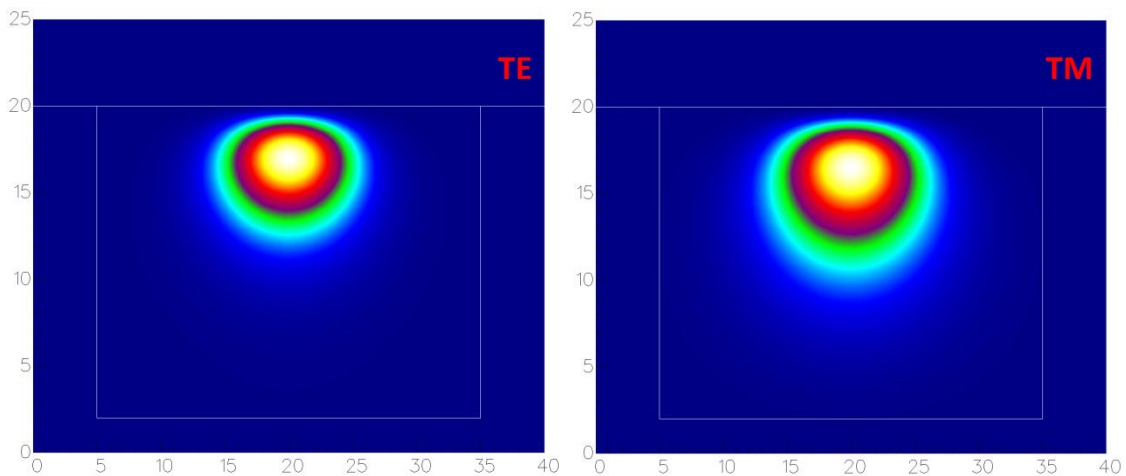
Figure 2.11. Optical intensity profiles of fundamental TE and TM modes.

The modes have different effective mode indices (2.1386 for TE, 2.2113 for TM) for each polarization and the mode size of TM polarization is slightly bigger than the TE polarized mode.

2.2   Coupled-mode Theory

Coupled mode theory explains the coupling of spatial modes among each other. In the case of As_2S_3-on-Ti:LiNbO$_3$ waveguides, we are interested in coupling between two unidentical waveguides in terms of size and refractive index: As_2S_3 with small size and higher index and lower index Ti:LiNbO$_3$ with its much larger size (Fig. 2.12). This type of coupling is called asymmetric coupling where the mode amplitudes and indices of two waveguides are not identical. The coupled mode equations between two modes with amplitudes A and B can be written as follows [21].

$$\pm \frac{dA}{dz} = i\kappa_{aa} A + i\kappa_{ab} B e^{i(\beta_b - \beta_a)z}, \qquad (2.31)$$

$$\pm \frac{dB}{dz} = i\kappa_{bb} B + i\kappa_{ba} A e^{i(\beta_a - \beta_b)z}. \qquad (2.32)$$

The equations 2.31 and 2.32 include self coupling terms. The coupling coefficient (κ_{ab}) between mode a and mode b is given by

$$\kappa_{ab} = \omega \iint\limits_{-\infty}^{\infty} \mathcal{E}_a^* \cdot \Delta\epsilon \cdot \mathcal{E}_b \, dxdy \qquad (2.33)$$

where $\mathcal{E}_a, \mathcal{E}_b$ are normalized mode fields. Equation 2.33 includes the dielectric coefficient difference between the perturbed and unperturbed waveguide cross section ($\Delta\epsilon$) represented as a tensor to include the coupling between anisotropic waveguides. Since dielectric tensor ($\Delta\epsilon$) is not a function of distance (z), the coupled mode equations can be solved analytically.
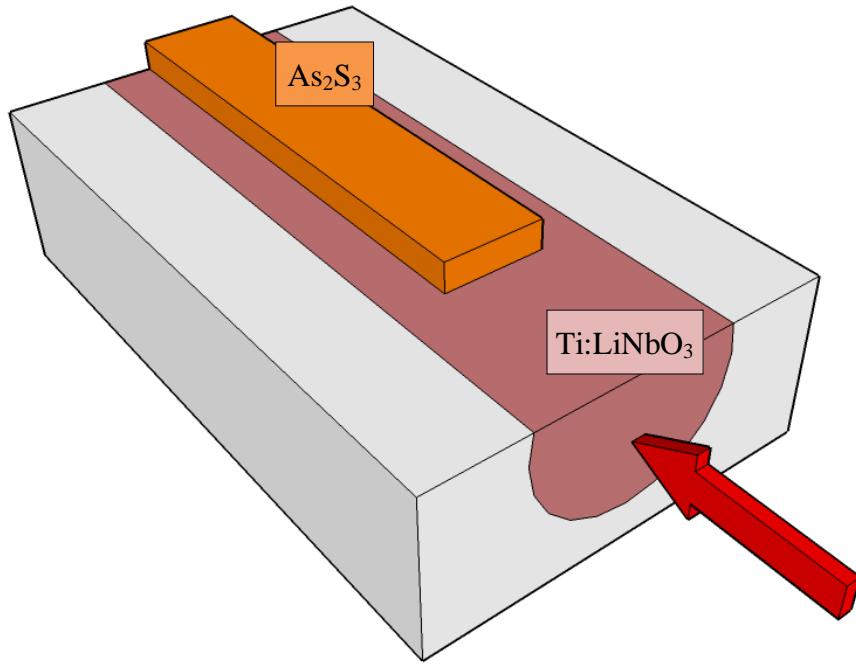
Figure 2.12. As$_2$S$_3$-on-Ti:LiNbO$_3$ codirectional coupler.

For simplicity, self coupling terms (κ_{aa}, κ_{bb}) will be neglected and $\kappa_{ab} = \kappa_{ba}^* = \kappa$ will be set. The general solutions to the field quantities are written

$$A(z) = (a_1 e^{-qz} + a_2 e^{+qz})e^{-i\Delta z} \qquad (2.34)$$

$$B(z) = (b_1 e^{-qz} + b_2 e^{+qz})e^{-i\Delta z} \qquad (2.35)$$

where $q = \pm\sqrt{\Delta^2 + \kappa^2}$, $a_1 + a_2 = A(0)$, and $b_1 + b_2 = B(0)$. In most cases the light is coupled into one waveguide where the boundary conditions are, A(0) =1 and B(0)=0 at the starting point z=0. Plugging equations 2.36 and 2.37 into 2.31 and 2.32, we get A(z) and B(z) as

$$A(z) = \left[\cos(qz) + i\frac{\Delta}{q}\sin(qz)\right]e^{-i\Delta z} \qquad (2.36)$$

$$B(z) = -i\frac{\Delta}{q}\sin(qz)\,e^{+i\Delta z} \qquad (2.37)$$

The amount of power coupled to the adjacent waveguide, $\frac{|B(z)|^2}{|A(0)|^2}$, and the power

remaining in the input waveguide, $\frac{|A(z)|^2}{|A(0)|^2}$, can be plotted as a function of qz and Δ (Fig.

2.13). For symmetric waveguides, full power is transferred at a certain length whereas

only a portion of the input power is coupled for asymmetric waveguides. The maximum

coupling occurs at a length, $L_c = \frac{\pi}{2q}$.
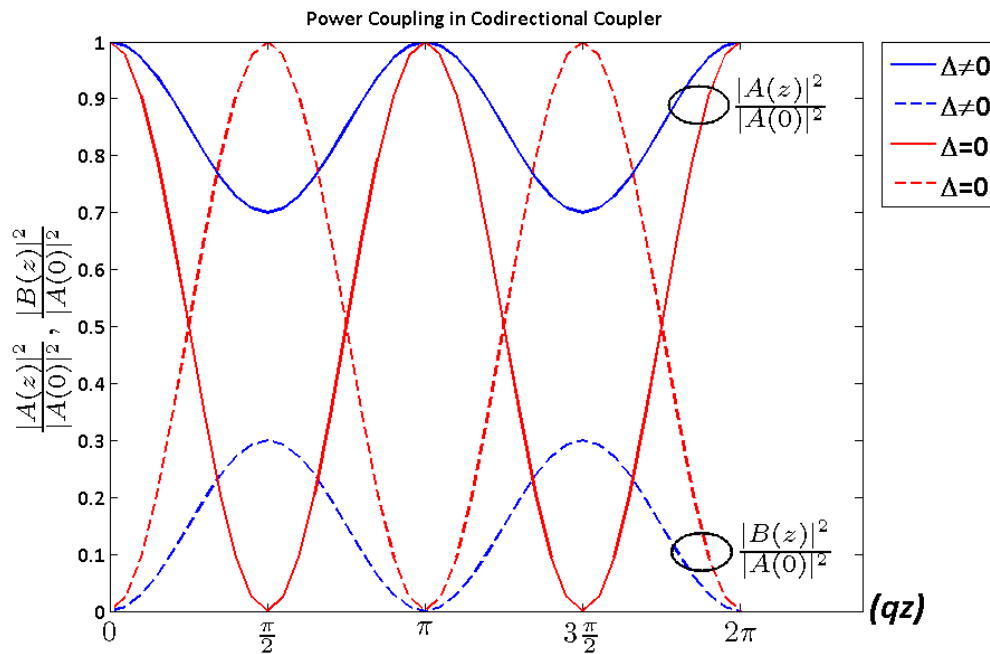
Figure 2.13. Amount of coupled power between two codirectional waveguides.

Since As$_2$S$_3$ and Ti:LiNbO$_3$ waveguides are not identical and the effective indices

are far apart from each other, the power coupling between the two are minimal.

Fimmwave uses the "Field mode matching" method of Sudbo [22] and can be utilized

to simulate three dimensional structures. As_2S_3 width and height are chosen 2x0.45μm and the structure on figure 2.12 is simulated for a propagation length of 500μm. A small portion 13.6% of the power is coupled up to chalcogenide waveguide at a distance of 210μm while most stays in titanium diffused region (Fig. 2.14). If the As_2S_3 length is made longer, the same portion of the power couples up and down along the length resembling the behavior in figure 2.13.
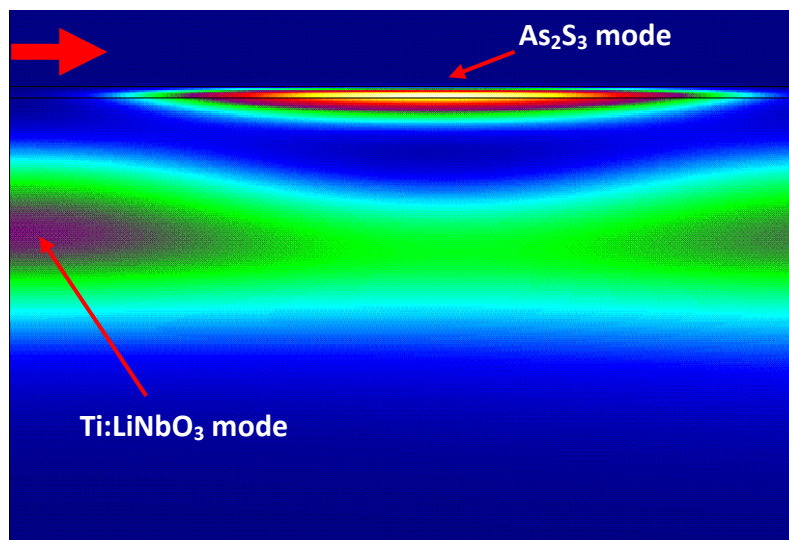
Figure 2.14. 13.6% of the input power is coupled into the chalcogenide waveguide.

Although there is no gap between the two unidentical waveguides, κ_{ab} is very small for a big sized As_2S_3 waveguide. It is possible to couple all of the power into the chalcogenide waveguide if the waveguide dimensions are kept very small. However the power confinement in these waveguides is not enough for bending structures such as s-bends and u-bends. A two-dimensional taper structure with increasing width is

proposed as the coupler between As_2S_3 and $Ti:LiNbO_3$ waveguides (Fig.2.15). The initial width is chosen to be small enough to minimally perturb $Ti:LiNbO_3$ mode while the final width should support a higher confinement. Mode in-depth analysis of the taper structure is given in Chapter IV.
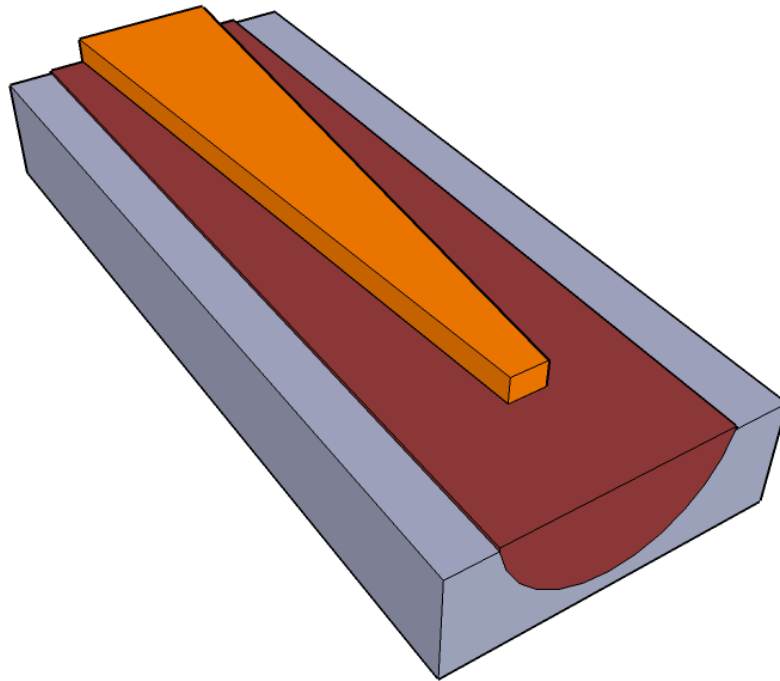
Figure 2.15. Proposed As_2S_3 taper structure.

2.3   Modes in Bent Waveguides

The main purpose of this research is to take advantage of mode bending ability of hi-index chalcogenide glass. Due to the small modal size and high confinement, it is possible to fabricate bent waveguides with a tight radius using As_2S_3 waveguides. The direction of the optical mode is changed after it is coupled up to the chalcogenide

overlay as the waveguides are curved. Figure 2.16 shows a schematic view of a fundamental mode propagating through a circular bend.
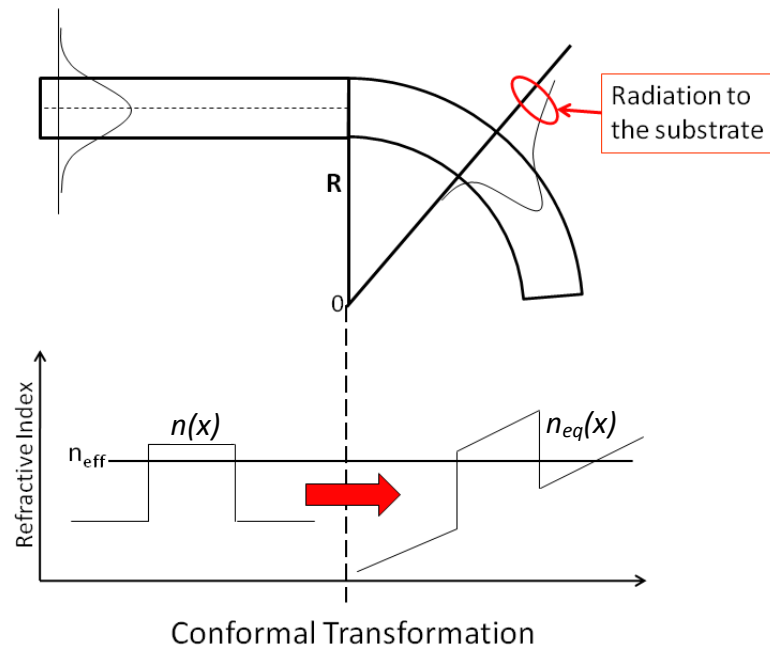
Figure 2.16. Refractive index transformation to a bent waveguide.

The mode slightly shifts towards and propagates along the outer boundary as in whispering-gallery modes (WGM). Physically the bending losses stem from power radiated towards the outside of a bend [2]. The losses increase exponentially with decreasing bend radius ($\alpha \propto e^{-R}$). The refractive index profile ($n(x)$) of a straight waveguide transforms to an equivalent refractive index ($n_{eq}(x)$) in a bend [3],

$$n_{eq}(x) = n(x)\sqrt{1 + \frac{x}{R}} \tag{2.38}$$

which can be used in a mode solution to estimate bend-loss. In addition to pure bending loss, there is also transition loss resulting from mode mismatch between the straight and the bent sections. To illustrate the transition loss, a bend radius of 100μm is introduced to TE_{11} mode of an As_2S_3 waveguide of 3μm width and 0.4μm thickness and the intensity profile is demonstrated (Fig. 2.17). The complex solver module of Fimmwave software is used and the complex refractive index is included to estimate propagation loss.
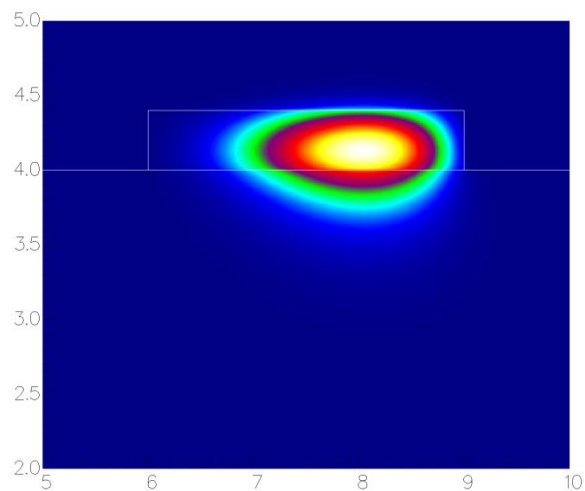
Figure 2.17. Mode shift towards the right boundary.

The optical mode is shifted to the right side by ~0.5μm if the center of the curve is set to the left of the waveguide. The difference between figures 2.6.a and 2.17 clearly explains the transition loss and it can be minimized by introducing an offset right after the straight waveguide. The transition loss increases with increasing radius.

The pure bending loss of a given waveguide can be simulated for a given constant radius. Since we are interested in the behavior of the optical mode inside the chalcogenide waveguide, the bend losses are calculated for TE_{11} and TM_{11} fundamental modes (Fig. 2.18). The losses are calculated for a given bend radius in dB/cm.
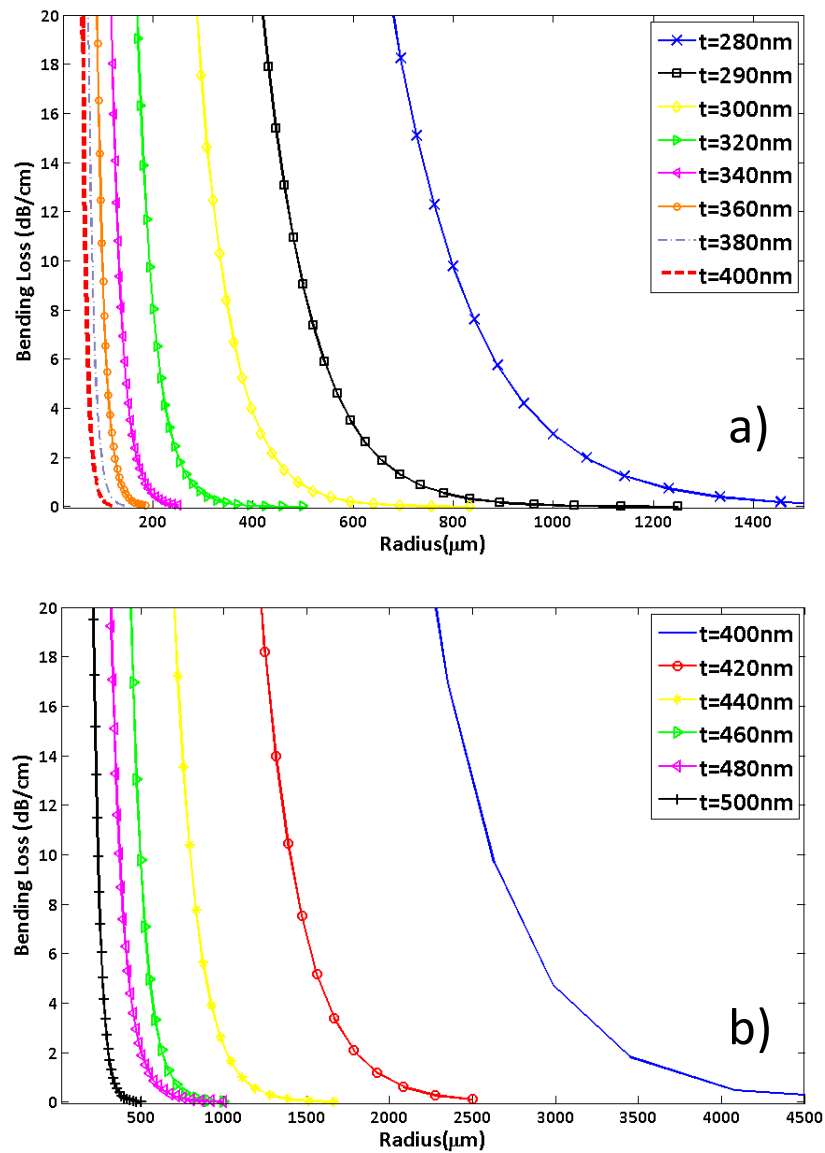
Figure 2.18. Bending losses for a) TE and b) TM polarized modes.

It is worth noting that TM polarized bending modes are significantly affected by the thickness of the overlay, whilst it is possible to use smaller bend radii for TE modes for the same thickness. The confinements which depend on the assumned Δn of both polarizations play a significant role in these results as TE polarized mode can achieve bends 50 times tighter than TM polarized mode at the thickness of 400nm.

2.4   Ring Resonator Theory

An optical ring resonator is a basic single stage filter with a feedback path. The feedback produces a pole that produce an infinite number of terms to the impulse response. The ring resonator on $LiNbO_3$ will be constructed with As_2S_3 and can be understood as an all-pass IIR (Infinite Impulse Response) filter [23]. It consists of a coupling region and a delay line (Fig. 2.19).
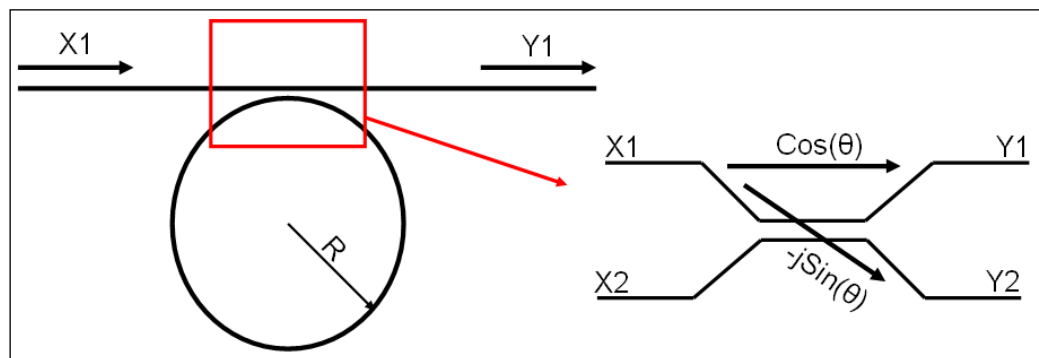
Figure 2.19. Schematic of coupling region of a typical ring resonator.

X1 and Y1 are the ingoing and outgoing electromagnetic fields respectively. A percentage of optical power ($|X1|^2$) couples up to the ring resonator and makes a

roundtrip through the feedback path. The same percentage of resonating power feeds back to Y1 while the remaining percentage stays in the ring. The amount of coupling is determined by the power coupling ratio, κ. The relationship between κ and θ is:

$$\cos(\theta) = \sqrt{1 - \kappa} \tag{2.39}$$

For the 2x2 coupler seen in figure 2.19, the through and cross port transmissions can be written as:

$$\begin{bmatrix} Y1 \\ Y2 \end{bmatrix} = \begin{bmatrix} \cos(\theta) & -j\sin(\theta) \\ -j\sin(\theta) & \cos(\theta) \end{bmatrix} \begin{bmatrix} X1 \\ X2 \end{bmatrix} \tag{2.40}$$

Physically the roundtrip length can be seen as a delay line, and the phase can be written as βL where L is the circumference of the ring.

$$\beta L = \frac{\omega}{c} n_g L = \omega T \tag{2.41}$$

$$T = \frac{n_g L}{c} \tag{2.42}$$

T is called the unit delay and is equal to 1/FSR, and FSR is the free spectral range which is the periodicity in the frequency domain. Overall, when we introduce the loss per roundtrip ($\gamma = 10^{(-loss/20)}$ (dB)) we can write the transfer function of the ring as:

$H(\omega) = \frac{Y1(\omega)}{X1(\omega)} = \cos(\theta) + -j\sin(\theta)\,\exp(-j\omega T) -j\sin(\theta)\,\gamma + -j\sin(\theta)$

$\exp(-j\omega T)\ \cos(\theta)\,\exp(-j\omega T)\ -j\sin(\theta)\,\gamma^2 + -j\sin(\theta)\,\exp(-j\omega T)$

$\cos(\theta)\,\exp(-j\omega T)\ \cos(\theta)\,\exp(-j\omega T)\ -j\sin(\theta)\,\gamma^3 + \ldots$

and once we simplify the equation above, we get:

$$H(\omega) = \frac{\cos(\theta) - \gamma e^{-j\omega T}}{1 - \cos(\theta)\gamma e^{-j\omega T}} \tag{2.43}$$

for the transfer function. We can plot the magnitude response of the ring resonator

($|H(\omega)|^2$) for given coupling ratio and loss values. Assuming 3dB coupling, we plot the

magnitude response for various roundtrip losses from 0.5dB to 6dB in Figure 2.20.
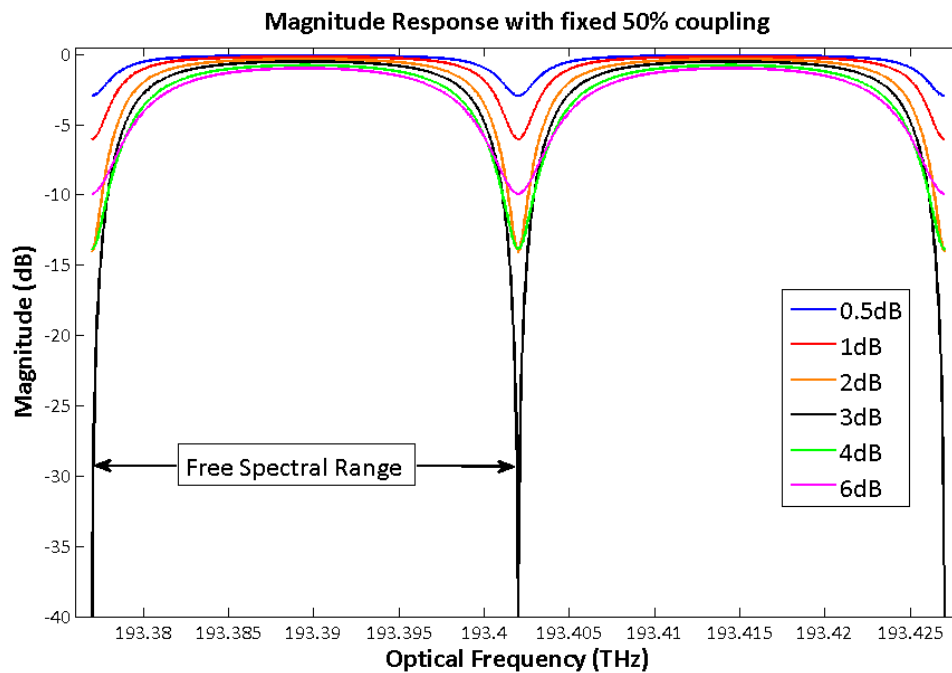
Figure 2.20. Magnitude response for various roundtrip loss values covering two FSRs.

We can also make a similar plot by keeping a fixed roundtrip loss and varying

the coupling ratio. Assuming 2dB round-trip loss, we plot the magnitude response for

various coupling ratios from 5% to 60% in Figure 2.21.
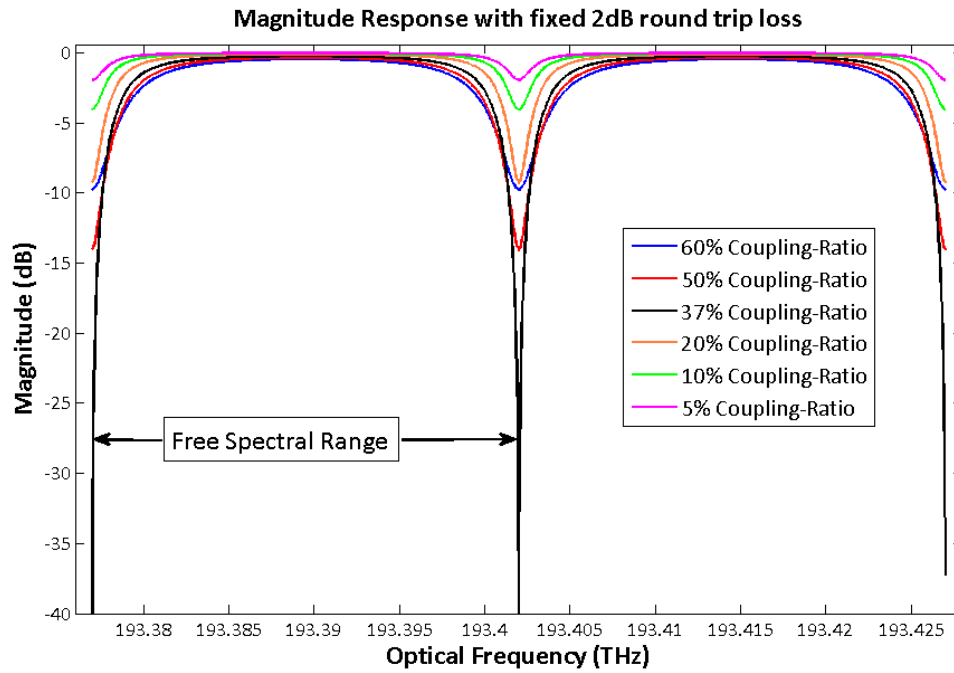
Figure 2.21. Magnitude response for various coupling ratios covering two FSRs.

As can be seen from the plots above, the shape of the transfer function highly depends on roundtrip loss and coupling ratio which depend on process parameters. However the distance between the dips (Δf), or the FSR, can be determined by the circumference of the As$_2$S$_3$ ring:

$$\Delta f = \frac{c}{n_g L} \cong \frac{300GHz}{n_g L} \qquad (2.44)$$

where n$_g$ is the group refractive index and L is the circumference in millimeters. The group refractive index of As$_2$S$_3$ is plotted in Figures 2.22 and 2.23. The refractive index values are obtained from bulk As$_2$S$_3$ [19]. As the ring gets smaller, we get a larger free spectral range. The FSR is 120GHz for L=1mm while the FSR is 1.2GHz for L=10cm.
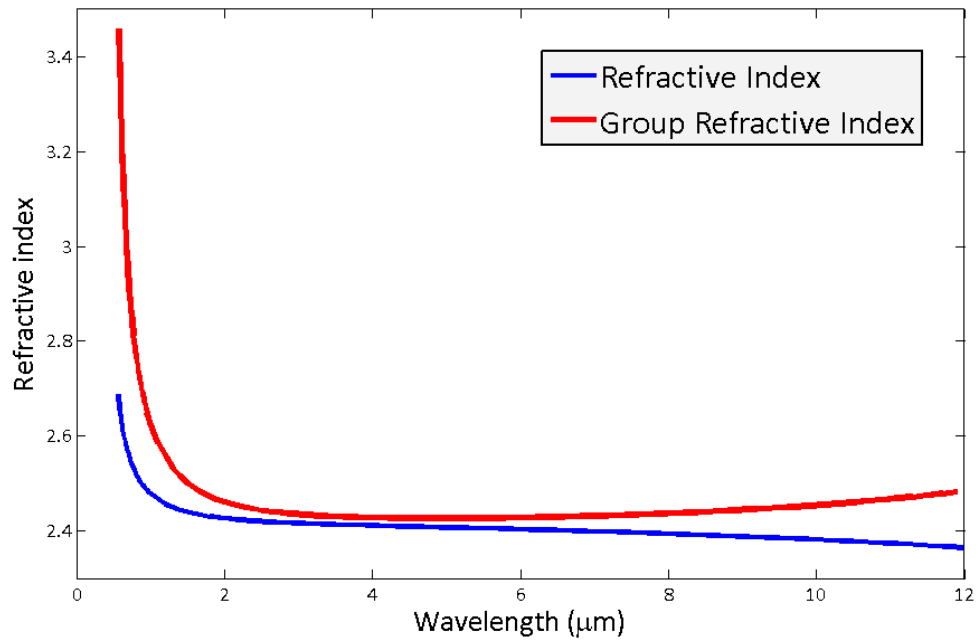
Figure 2.22. Group refractive index of As_2S_3 is higher than regular refractive index.
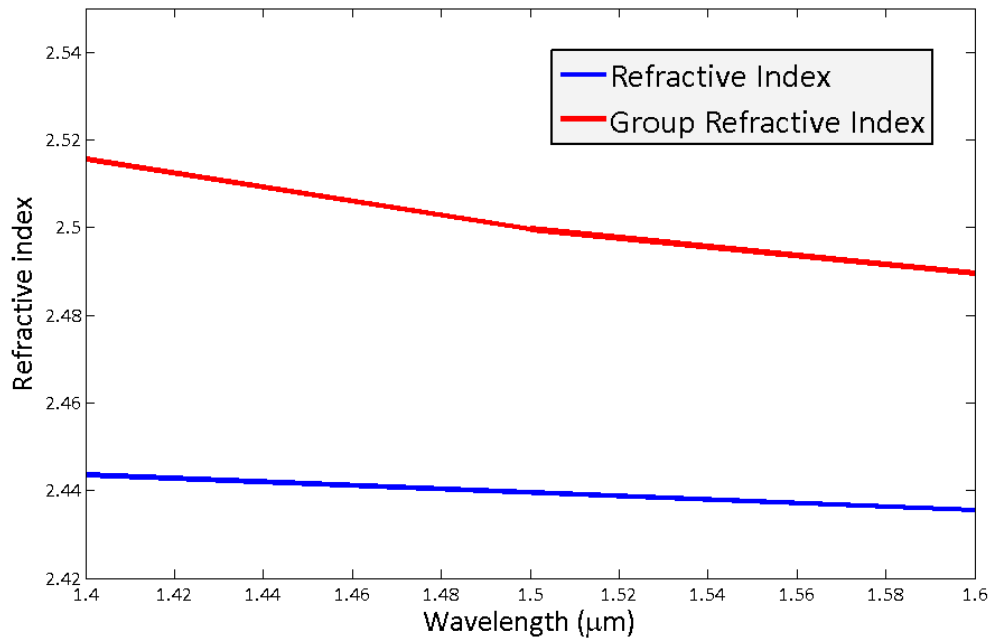
Figure 2.23. Group refractive index of As_2S_3 from 1.4µm to 1.6µm.

It is significant to evaluate the phase response of an optical filter besides its magnitude response. Since the optical ring resonator is a delay line the group delay (τ_g) information is a figure of merit for signal processing applications. The phase response is derived from the transfer function and is defined as follows:

$$\Theta(\omega) = \tan^{-1}\left[\frac{\text{im}[H(e^{-j\omega})\}}{\text{re}[H(e^{-j\omega})\}}\right] \tag{2.45}$$

and the group delay is defined by the derivative of the phase response of the transfer function multiplied by the unit delay T.

$$\tau_g(\omega) = -T\left(\frac{d\Theta}{d\omega}\right) \tag{2.46}$$

The group delay can be plotted for several coupling ratios at a fixed 3dB roundtrip loss (Fig. 2.24). Here the zero of the transfer function is chosen so that it is minimum phase, i.e. $z_1 = \frac{\gamma}{\cos(\theta)} < 1$. If the magnitude of the zero ($|z_1|$) is bigger than 1, the zero of the transfer function is called a maximum phase zero. Although $|z_1|$ and $\left|1/z_1\right|$ have the same distance from the unit circle ($|z| = 1$), and thus the same magnitude response, they have different group delay responses (Fig. 2.25).
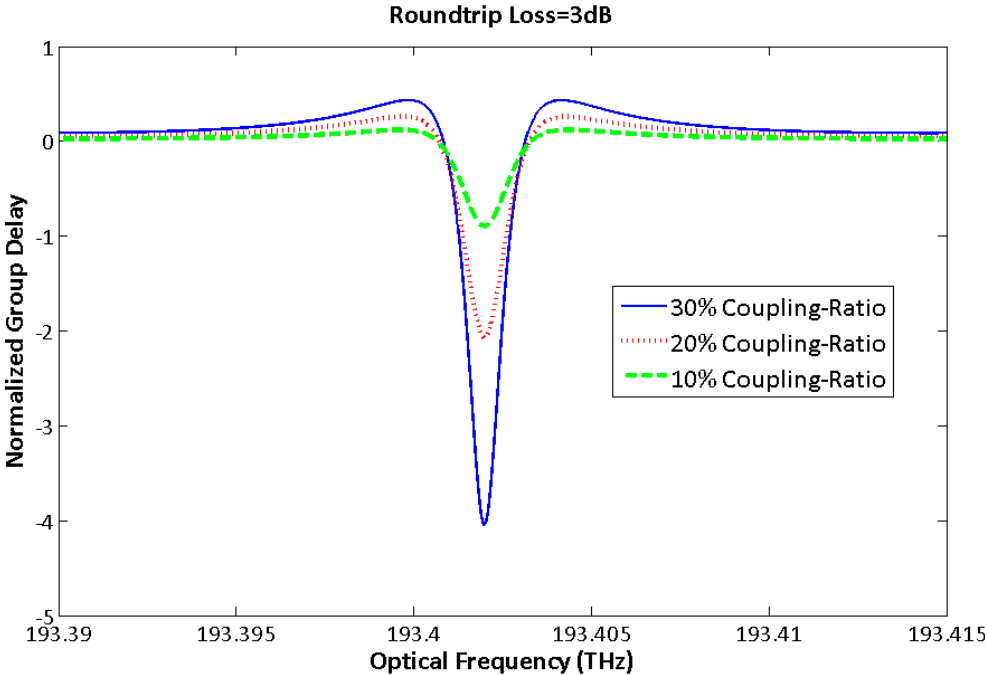
Figure 2.24. Group delay as a function of coupling ratio.
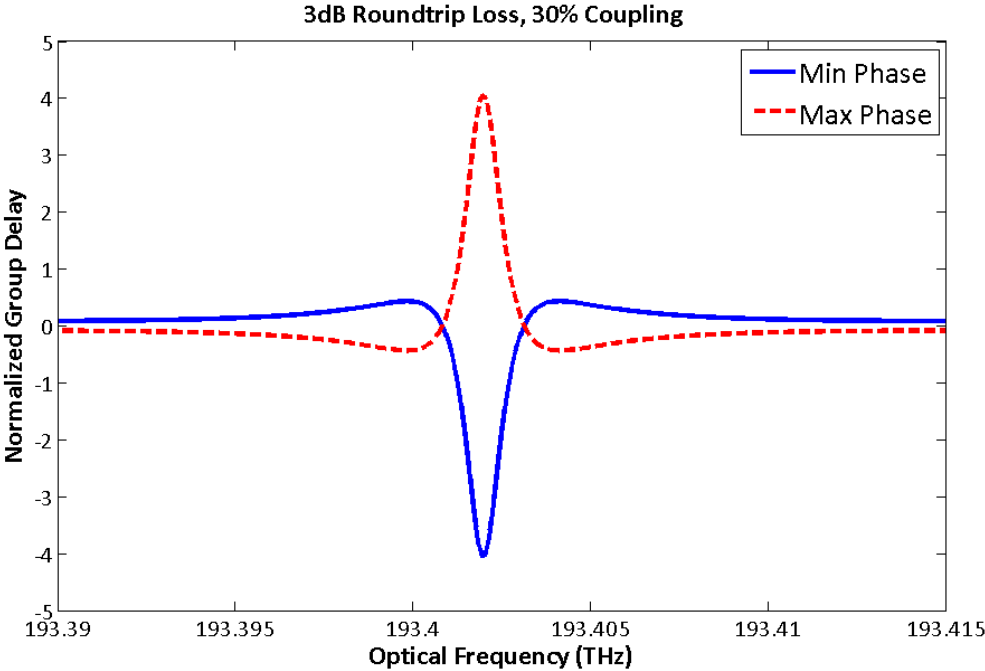
Figure 2.25. Group delay of maximum and minimum-phase zeros of equal magnitude.

The group delay is a measure of the waveguide quality of a ring resonator. A ring with low roundtrip loss will have a higher group delay than a lossy ring resonator for the same coupling ratio. A ring resonator with a 25GHz free-spectral range will act like a ~40ps of delay line and a higher group delay (multiple of $T\sim40$ps) means the optical signal survives many round trips.

2.5   Optical Waveguide Measurements

After the fabrication steps are completed, the optical waveguides are tested to assure low loss operation or superior response if they are designed as optical filters. Since the waveguides are designed for operating around 1.5µm wavelength the laser sources used to test them are robust telecommunication lasers. The basic schematic of a loss measurement setup includes a laser source, collimating optics or optical fiber, and a detector that is sensitive to telecommunication wavelengths. The use of collimating or bulk optics that were used in the past to collect laser light and couple it into the optical waveguide has been abandoned due to its time consuming alignment. Since semiconductor telecommunications lasers have high numerical apertures (NA), they already come with low NA optical fibers pigtailed to their end to save a great percentage of the optical power. The waveguides of interest are Ti:LiNbO$_3$ waveguides and they are comparable in size to regular single-mode fibers. It is convenient to use a measurement setup where optical fiber is butt-coupled to Ti:LiNbO$_3$ waveguide at both ends (Fig. 2.26).
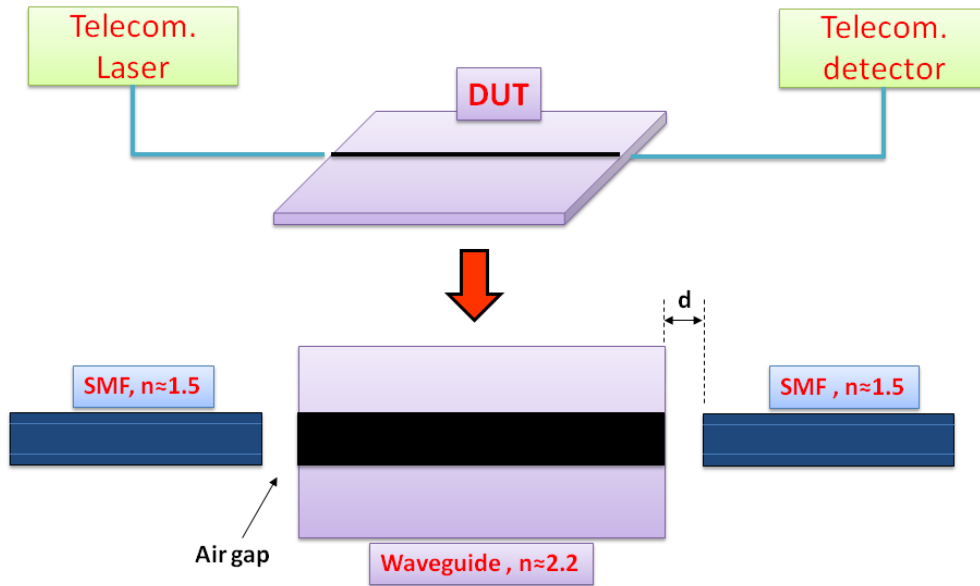
Figure 2.26. Waveguide measurement setup.

The insertion loss of a waveguide in dB is equal to $10\log(\frac{P_{out}}{P_{in}})$ and includes fiber-to-waveguide and waveguide-to-fiber coupling losses and waveguide propagation losses. The insertion loss is obtained after subtracting the loss in the system measured by coupling input and output fibers to take a reference measurement. The air gaps (*d*) before and after the waveguides introduce two Fabry-Perot interferometers that contribute to coupling losses. The transfer function of a fiber-air-lithium niobate system can be written as

$$H(e^{-j\omega}) = \frac{t_{12}t_{23}\sqrt{e^{-j\theta_2}e^{-j\omega}}}{1 + r_{12}r_{23}e^{-j\theta_2}e^{-j\omega}} \qquad (2.47)$$

where t_{12}, t_{23}, r_{12} and r_{23} are transmission and reflection coefficients at fiber-air and air-waveguide boundaries respectively. $\theta_2 = (\frac{2\pi n_{air}}{\lambda} \cdot d)$ is the phase term related to the air gap. The maximum and minimum transmission through an air gap can be calculated;

a 3µm air gap can cause between ~18% and ~40% power loss. Due to wide range of loss values, it is customary to use index-matching liquid of refractive index ~1.5 to cover the air gap between the fiber and the lithium-niobate. This will significantly reduce the amount of power loss due to Fresnel reflections.

The filter response of optical filters for telecommunications can be measured with tunable and coherent lasers. Tunable lasers that are able to tune the lasing wavelength over ~80nm range (from 1490 to 1570nm) are readily available, i.e. Agilent/HP 8168E and 81680A. Optical spectrum analyzers can be used as detectors in some filter applications that do not require high resolution, but may be replaced with tunable lasers and dedicated detectors. Some of the optical table-top lasers in our lab are already equipped with detectors.

Another important need for measuring optical waveguides in general is the state of polarization (SOP) of the incoming laser source. Although semiconductor lasers are built to emit a certain polarization, the state of polarization changes along the coupled fiber. Optical waveguide filters are designed to work with certain polarization states such as TE or TM. Birefringent materials such as lithium-niobate require launching 100% TE or TM polarized light in order to maintain the same state of polarization coming out of it.

The waveguide loss can be measured using the setup in Figure 2.27a. The swept laser source is fed to the polarization controller's input port before reaching the waveguide. The incoming SOP to the waveguide can be adjusted using the polarization

controller that has a motorized half-wave, quarter-wave and linear-polarizer plates. For

lithium-niobate linearly polarized SOPs (TE & TM) are launched into the waveguide and

insertion loss values are recorded from 1520 to 1570nm.
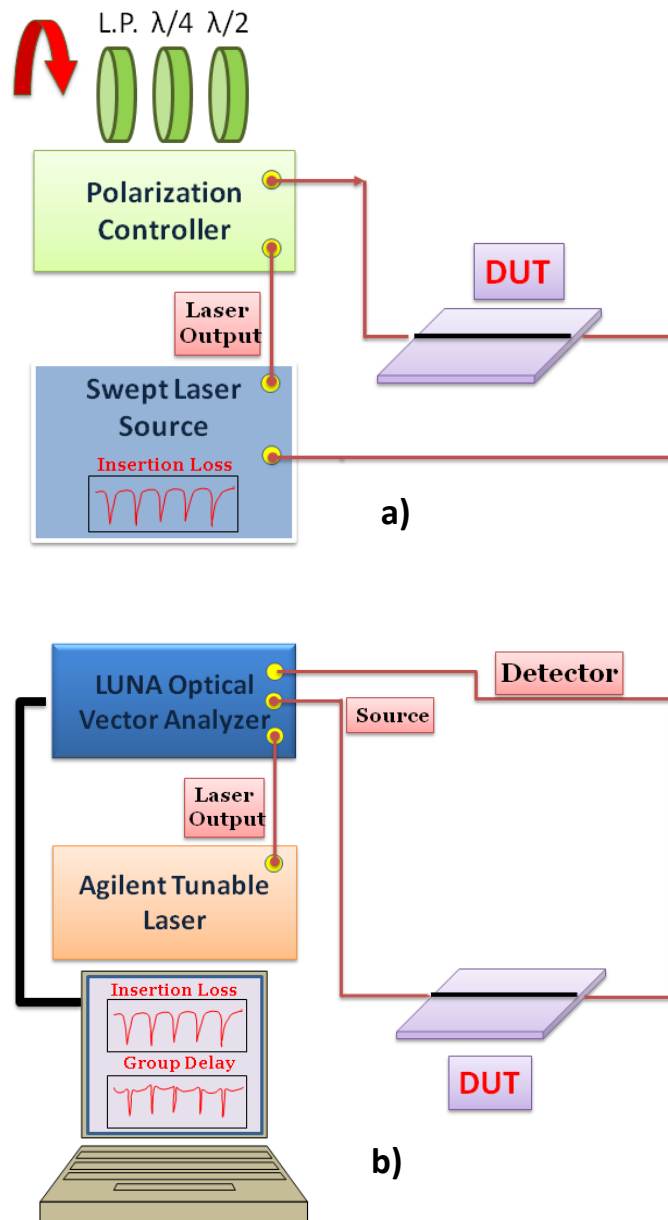
Figure 2.27. a) Measurement setup for waveguide losses; b) Setup for group delay and insertion loss measurements; Jones Matrix method.

Optical filters do not only require insertion loss information but also phase information. As shown before, ring resonators show highest extinction ratio when the roundtrip loss is equal to the critical coupling. Most researchers ignore the phase response of the ring resonators and do not measure the group delay of the ring. However, phase information leads to group delay which is of great significance when considering the quality of the filter. The setup in Figure 2.27b measures both loss and group delay information using LUNA Technologies Optical Vector Analyzer (OVA) and a tunable swept laser source. OVA provides the Jones Matrix information $\begin{bmatrix} a & b \\ c & d \end{bmatrix}$ of the device under test (DUT) that tells how it operates in a given system. Jones calculus was invented by R.C. Jones in 1941 and is a way of representing the polarized light (Jones Vector) and the effect of an optical device on a given polarization. The Jones method is similar to Stokes parameters except it includes instantaneous electric fields rather than average power. The data given by OVA is of the form

$$J_i = \begin{bmatrix} a_i & b_i \\ c_i & d_i \end{bmatrix} \tag{2.48}$$

and includes Jones matrix (J_i) information for every wavelength over the spectrum. Insertion loss and average group delay can be calculated using 2.48 for each wavelength as follows

$$IL_i = 10\log(\frac{|a_i|^2 + |b_i|^2 + |c_i|^2 + |d_i|^2}{2}) \tag{2.49}$$

$$GD_i = \left(\frac{a_i^* a_{i+1} + b_i^* b_{i+1} + c_i^* c_{i+1} + d_i^* d_{i+1}}{\Delta\omega} \right) \tag{2.50}$$

where $\Delta\omega$ is the change in frequency from index *i+1* to *i.*

The information represented has some inaccuracies built in it as it does not include the Jones matrices of the input and output optical fibers that couple to the waveguide ends. Although the optical fibers have very low-loss they have an effect on the state of polarization as they induce a rotation of the phase term of the Jones matrix elements. The complete Jones matrix information also includes the two more arbitrary matrices for source and detector fibers.

$$\bar{K} = \begin{bmatrix} \sin\theta_d e^{i\varphi_d} & -\cos\theta_d e^{-i\psi_d} \\ \cos\theta_d e^{i\psi_d} & \sin\theta_d e^{-i\varphi_d} \end{bmatrix} \begin{bmatrix} a & b \\ c & d \end{bmatrix} \begin{bmatrix} \sin\theta_s e^{i\varphi_s} & \cos\theta_s e^{i\psi_s} \\ -\cos\theta_s e^{-i\psi_s} & \sin\theta_s e^{-i\varphi_s} \end{bmatrix} \qquad (2.51)$$

To reach the actual DUT Jones Matrix information ($\bar{J}$), all unknowns ($\theta_d, \varphi_d, \psi_d, \theta_s, \varphi_s, \psi_s$) should be evaluated and the matrix $\bar{K}$ should be multiplied by arbitrary fiber source and detector rotation matrices on both sides to eliminate them. The derivation of rotation matrices is not in the scope of this dissertation although it is automated and used in our lab.

CHAPTER III

FABRICATION PROCESS DEVELOPMENT

This chapter discusses the fabrication methods of both Ti:LiNbO$_3$ diffused and As$_2$S$_3$ ridge waveguides as well as new developments made to improve the waveguide quality. Basic thin-film characterization tools are used to check the composition and quality of the deposited films.

3.1   Fabrication of Ti:LiNbO$_3$ Waveguides

Metal diffusion into lithium niobate (LiNbO$_3$) is a preferred way of building low-loss and functional waveguides that are size compatible with regular single mode communication fibers. The most established waveguide fabrication in LiNbO$_3$, besides proton exchange process, is titanium (Ti) in-diffusion at elevated temperatures. A Ti pattern of desired thickness and width is patterned on LiNbO$_3$, and then diffused into the substrate at around 1000°C.

The fabrication process starts with a rectangular piece or optical chip cut from an x-cut y-propagating LiNbO$_3$ wafer. The optical chip is then cleaned to remove any surface residue titanium deposition. A preselected thickness is deposited on the surface and photolithographic patterns are revealed after photoresist development. The titanium is protected by the hardened photoresist while the rest of it is etched away using reactive ion etching. After the photoresist on the surface is removed the sample is placed into the diffusion furnace at 1025°C for preferred time. The y-propagating

ends of the sample are polished to optical quality before optical testing. The Figure 3.1 gives a brief summary of the fabrication process.
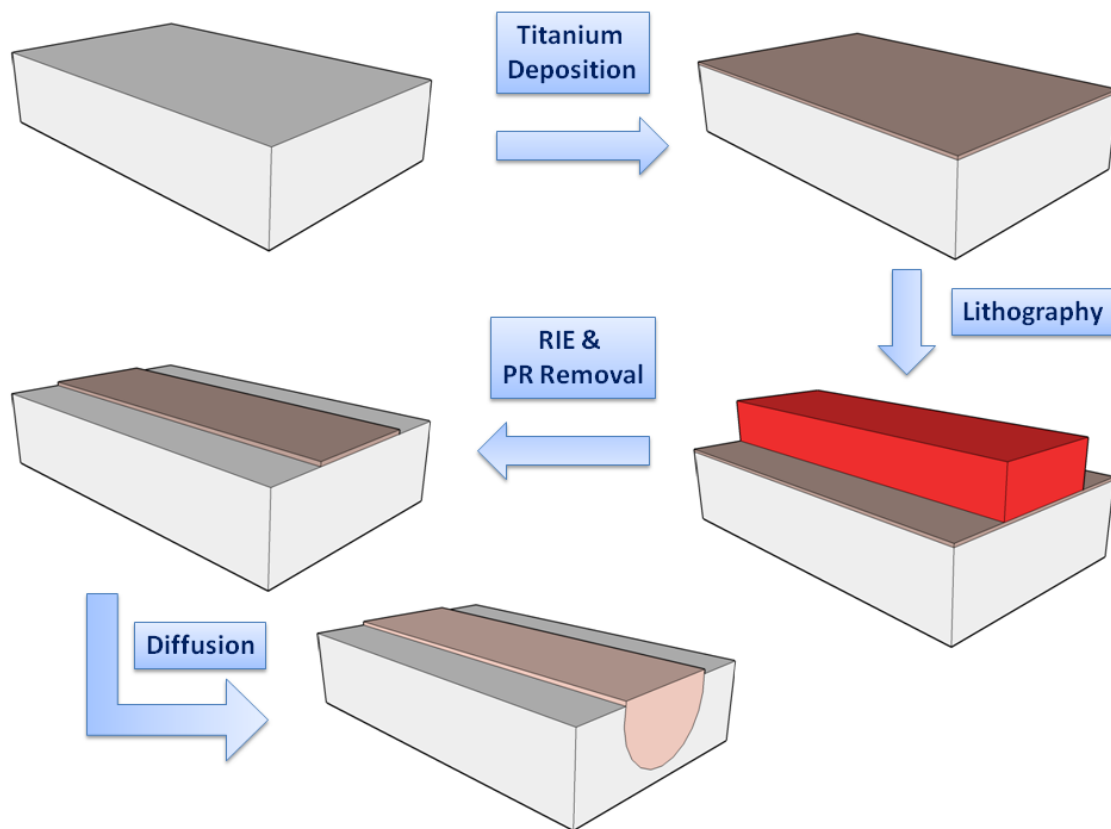
Figure 3.1. Ti:LiNbO$_3$ fabrication process flow.

The titanium metal can be deposited using 3 deposition techniques: DC Sputtering, E-beam Evaporation, and DC Magnetron Sputtering. The first and the third one involve a plasma environment while the metal is heated to its melting point in the second one in order to evaporate onto the substrate. Plasma during sputtering increases the energy of the Ti atoms that are pulled out from the target and causes

them to hit the substrate with higher energy. It is a preferred deposition method due to its better adhesion to the surface. To create waveguides that work around 1.5µm wavelength, the deposited thickness of the Ti strip can be varied from 800Å to 1300Å but the diffusion time has to be adjusted accordingly. More titanium means higher titanium atom concentration in $LiNbO_3$ and it may desirable in certain applications. The selected Ti strip width is 7µm and is patterned onto surface before etching.

A reactive ion etching (RIE) system from Oxford Instruments is used for titanium etching. A fluorine based gas (CHF_3) is used in tandem with argon (Ar) to result in titanium fluoride (TiF_x) reaction products although a chlorine based gas is preferred for faster etching rate [24]. The RIE system is equipped with inductively-coupled plasma (ICP) in addition to regular RF power and ICP results in much faster etch rates but low selectivity to photoresist. The inductive coil surrounds the etching chamber and increases the number of ionized gas molecules. It is preferred to stop etching right before reaching the $LiNbO_3$ surface to prevent the damage and continue with hydro-fluoric acid to etch away the remaining Ti on the surface. However it is possible to slow the etch rate and avoid the surface damage.

The samples with Ti strips are put on a flat alumina boat, and loaded into a 10cm diameter diffusion furnace. The furnace was heated up to 1025°C by increasing the temperature 13.5°C/min, and cooling done over a 6 hour period without any interference. Diffusion gas is selected as breathing air (BA) which is composed of 70% N_2 and 30% O_2 and it is bubbled through room temperature water at a flow rate of

150sccm (0.15L/min). Titanium atoms diffuse into the LiNbO$_3$ substrate in an anisotropic manner. A great deal of attention has been directed to finding the lateral and vertical diffusion profiles [25-27] and their relations with temperature and initial Ti thickness. It is found that lithium out-diffusion can create a lateral surface guiding layer [28] that is undesirable if diffused waveguides are close to each other for a specific device. In order to prevent lithium out-diffusion, a common practice is to use a wet diffusion environment, where gases flow through water to introduce water vapor [29]. Although there are reports of better surface quality in a dry environment [30], good results are also obtained in the cases of wet O$_2$ and wet Ar [31].

The titanium on the surface goes through several phase changes when exposed to heat and oxygen. The phase transformation of the diffusion of Ti strips is also well addressed [32-33] and it is concluded that rutile (TiO$_2$) phase is dominant at low temperatures. Titanium is completely oxidized in the first hour of diffusion, and after this stage Li$^+$ (lithium) and Nb^{5+} (niobium) atoms migrate from the bulk to the surface and create Ti:Li:Nb oxide layer [32, 34]. In two studies, granular or island-like structures resulting from incomplete diffusion of Ti into LiNbO$_3$ were observed [35-36], although some researchers suggest it, even longer diffusion times did not solve this problem [37]. There can be a great source of optical loss if the samples are left under-diffused. Moreover, a critical observation is the ratio of initial deposited Ti thickness to the post-diffusion thickness is 1:1.5-2 [25, 34, 38]. This can significantly affect the final mode profile, since the Ti concentration is highest at the surface. It is predicted that

TiO_2 formation is the reason for this height increase [25, 34]. In both cases, the flow rates are around 1L/min which is also used in another study [31] or even exceeded (2.4L/min) [36]. Unlike the results reported in other papers, our ratio of post-diffusion thickness to initial Ti thickness is less than one. To obtain a higher ratio, we have conducted experiments by increasing the flow rate to 1L/min from 0.15L/min or even higher to 1.5L/min. However our results did not change and we still obtained a much smaller ratio. In order to better understand the height increase, we prepared 7 identical samples with the same Ti thickness using e-beam evaporation. After lithography and RIE steps, we placed 6 of them into the diffusion furnace separately for 0, 1, 3, 5, 7, and 9 hours. We saved one of them to compare the surface of the Ti strip and we recorded the observed height. The sample with 0 hour diffusion was heated to the diffusion temperature but the diffusion did not proceed and the furnace was shut down. The surface modification of the titanium strips is observed looked (Fig. 3.2).

a) Patterned Ti strip before diffusion

b) 0 hour diffused sample

c) 1 hour diffused sample

d) 3 hour diffused sample

e) 5 hour diffused sample

f) 7 hour diffused sample
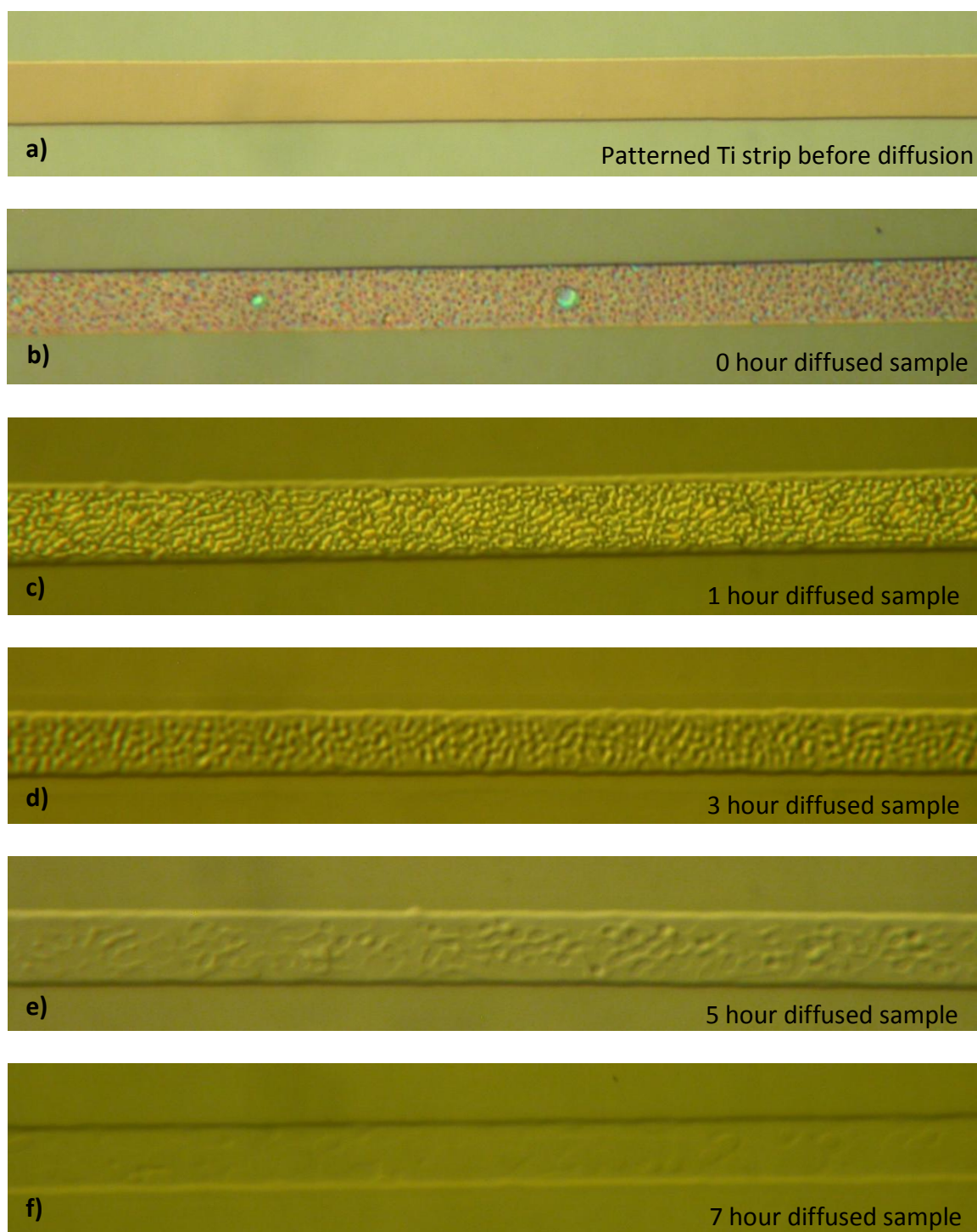
Figure 3.2. Ti diffusion progress into $LiNbO_3$ observed at each step by an optical microscope: a) Only Ti strip; b) 0h; c) 1h; d) 3h; e) 5h; f) 7h; g) 9h; h) 950Å diffused dry BA 9.5h at 1025°C; i) 1200Å diffused dry BA 12h at 1025°C.

g)

9 hour diffused sample

h)

i)
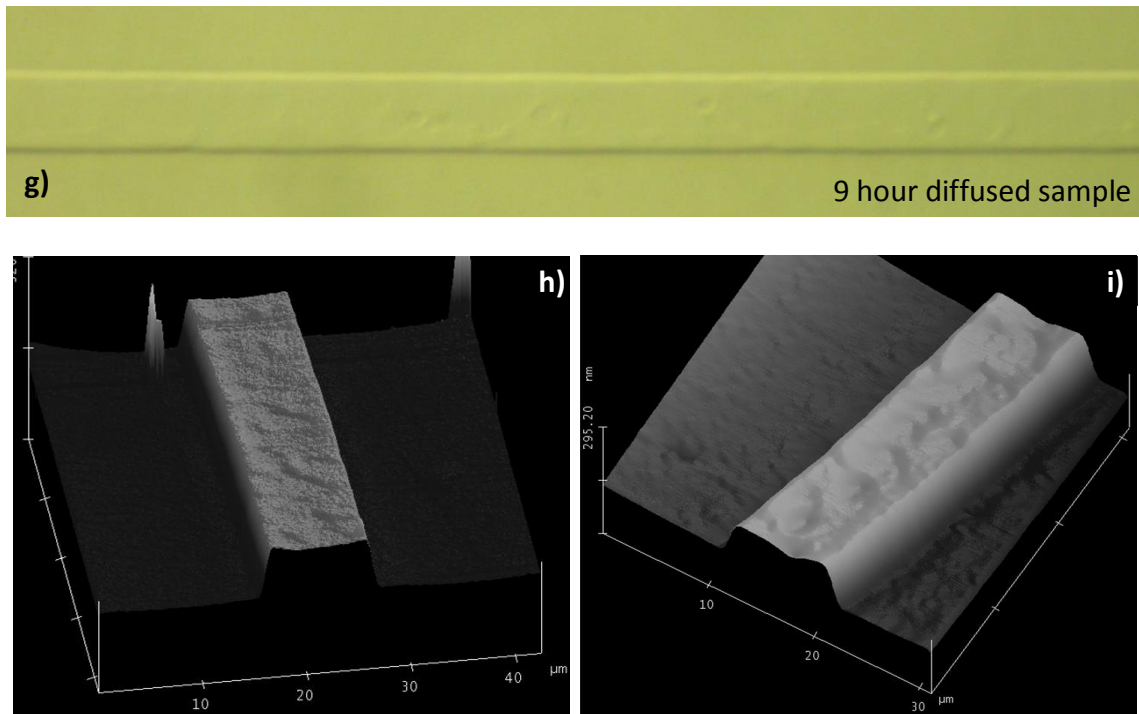
Figure 3.2. Continued.

We have also used atomic-force microscopy (AFM, from Veeco Instruments USA) in multi-tapping mode to capture the surface of post diffusion height of several samples (Fig. 3.2b-c). Although the two samples had different initial Ti strip thicknesses, their surfaces after diffusion look very comparable. The modification of the surface and the height increase clearly indicates the TiO_x formation (Fig. 3.3). Fukuma et al. also suggests that residual TiO_2 films or insufficient diffusion is the real source of surface roughness, and this eventually leads to light scattering [20]. Eventually the post diffusion height decreases down to ~800Å which is below the initial thickness of ~900Å.
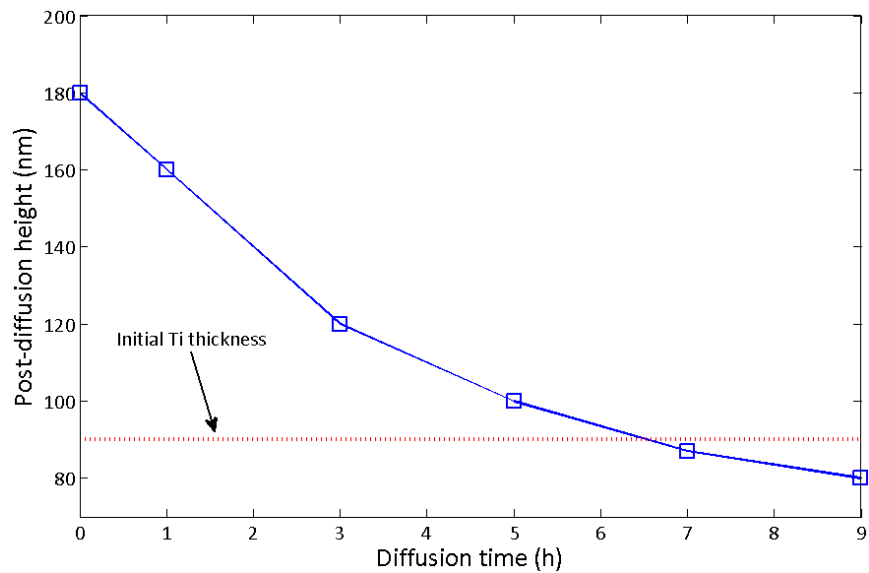
Figure 3.3. Post diffusion thickness vs. diffusion time for e-beam evaporated Ti strips.

The titanium surface looks better as the diffusion progresses and the island-like structures disappear. Although the surface quality of samples gets better with longer diffusion time, this is not reproducible for all the samples. Getting smooth surfaces is very critical for obtaining low-loss As_2S_3 waveguides besides $Ti:LiNbO_3$ waveguides. Any roughness underneath As_2S_3 will introduce more loss due to increased bottom-wall scattering. We have switched to using DC Magnetron Sputtering for deposition of titanium instead of using regular DC sputtering or E-beam Evaporation. We also introduced a heated bubbler to the diffusion system instead of using a room temperature bubbler where the breathing air passes through water preheated to 70°C. The water vapor amount is increased using this system. Finally we have obtained very smooth diffused surfaces that are reproducible from sample to sample (Fig. 3.4).
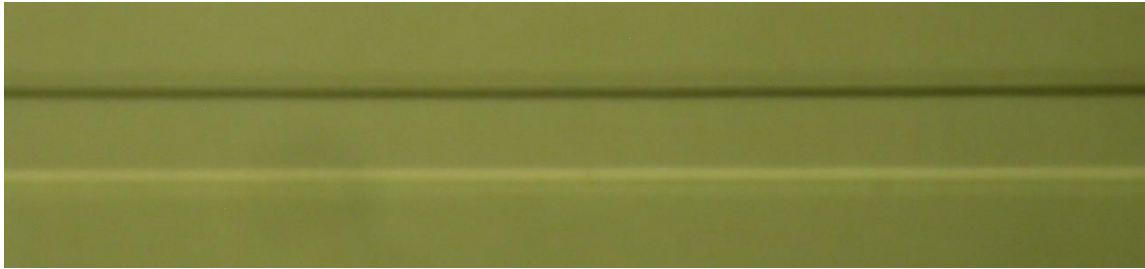
Figure 3.4. Diffused waveguide surface on LiNbO$_3$.Ti is sputtered by DC magnetron sputtering and diffused using a heated bubbler.

After diffusion the sample ends are polished to optical quality using different graded abrasive pads. We have switched from a slurry based polishing recipe to using only water due to its much improved speed and quality. The abrasive films have diamond particles of different grain sizes resin bonded on top of it. Since the hardness of diamond is larger than LiNbO$_3$, the choice of diamond is necessary instead of silicon carbide. The rectangular samples have very rough edges after dicing them from a whole wafer. The area of an edge is the thickness of LiNbO$_3$ (1mm) times the sample width (10mm to 20mm) and it takes less time to polish an edge with less area. Polishing is faster to start with a bigger grain sized film such as 15μm and continue to smaller ones, 3μm, and 0.5μm diamond sizes to obtain smoother edges. The evolution of the edge profile is depicted in Figure 3.5.
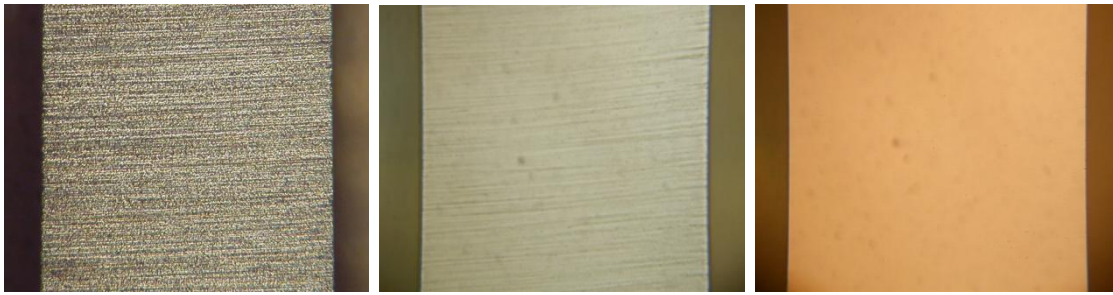
Figure 3.5. Polished edges after 15µm, 3µm, and 0.5µm.

3.2   Fabrication of Chalcogenide Waveguides

Chalcogenide glasses are amorphous materials with at least one of the chalcogen elements; Se, Te, and S. Arsenic-trisulfide (As_2S_3) is a binary glass and a member of the chalcogenide glass family. Chalcogenide glasses have been explored for both near and mid-infrared optical waveguides and fabrication methods involve regular top-down approach, lift-off, and photorefractive effects [39-43]. The regular top-down approach contains deposition of As_2S_3 thin film, lithography and etching to create the core region. Waveguides using the lift-off are much simpler and there is no need to do any sort of etching as waveguide patterns are revealed after removing the photoresist. Since illumination of above band-gap light on chalcogenide glasses increase its refractive index, the photorefractive effect can also be used to create optical waveguides. Out of the three waveguide fabrication methods, the standard top-down approach provides the most control over waveguide dimensions and it is being used with other material systems (silica, silicon, and III-V) as well. Although we started using lift-off process fabricating As_2S_3 waveguides, we switched to regular top-down approach to obtain smooth edges and controllable linewidths.

The As_2S_3 waveguide fabrication process starts with already diffused Ti:$LiNbO_3$ optical sample. A preselected As_2S_3 thickness is deposited on the surface using RF-magnetron sputtering system. A protective layer of SiO_2 and Ti are evaporated onto As_2S_3 as a protective cover layer before lithography. Photolithographic patterns on 3-layer stack are revealed after photoresist development. The areas that are not protected are etched down to $LiNbO_3$ surface. After the photoresist on the surface is removed the sample is placed in hydro-fluoric (HF) solution to remove SiO_2 and Ti before testing. The Figure 3.6 gives a brief summary of the fabrication process.
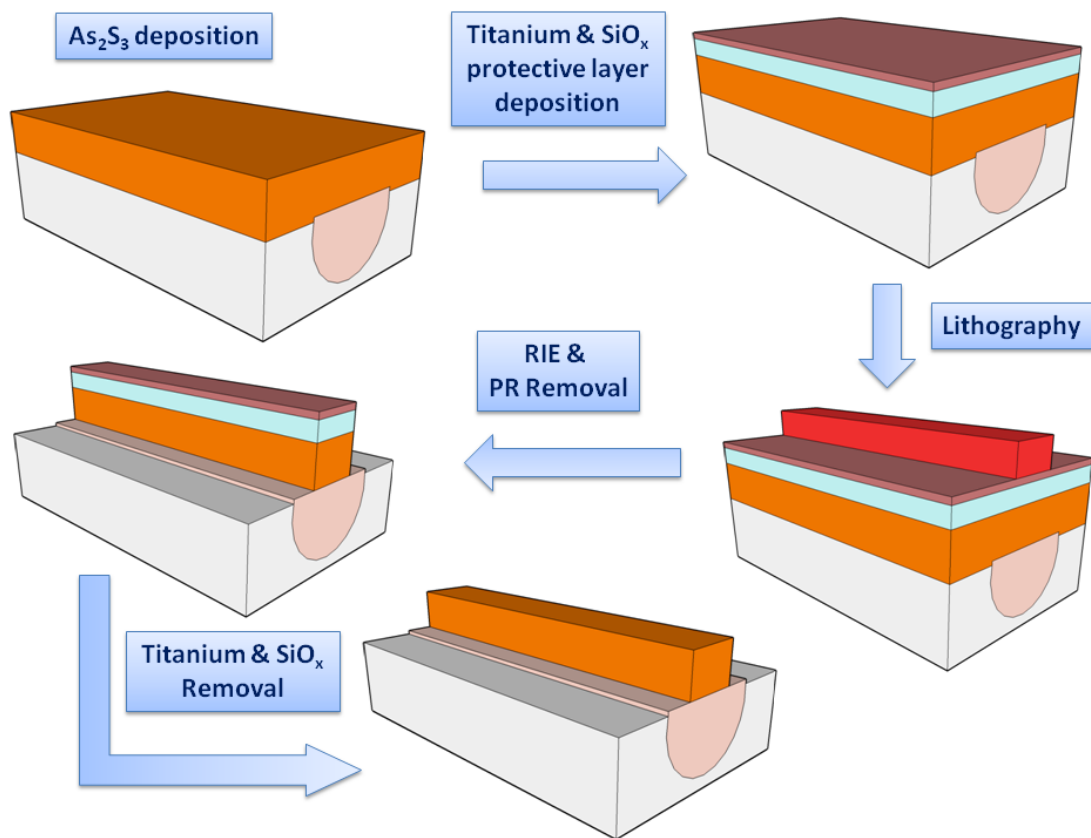
Figure 3.6. As_2S_3-on-Ti:$LiNbO_3$ fabrication process flow.

3.2.1 Chalcogenide Thin-film Deposition

Thermal evaporation [42, 44], ultrafast pulsed-laser deposition [45], and RF sputtering [39] are physical deposition methods so far used to successfully deposit waveguide quality thin-film chalcogenide glass. Due to its lower melting point (~700°C) compared to oxide glasses and its ease of practice, thermal evaporation is a preferred deposition method. The exact stoichiometry of As_2S_3 is hard to achieve with evaporation since the vapor pressures of arsenic and sulfur are different from each other for the same vacuum pressure and temperature. The exact mass percentages (60.9% for As, 39.1% for S) are hard to achieve using evaporation unless a system with two thermal boats is used for each material. Pulsed laser deposition, on the other hand, is not prone to stoichiometric errors as it physically takes away atoms from the target using laser ablation. Radio-frequency (RF) sputtering is preferred while depositing dielectric and semiconductor materials such as SiO_2, Si_3N_4, and TiO_2. Due to its semi-conductive nature [46], As_2S_3 can also be deposited using RF sputtering. Sputtering is a physical vapor deposition and a plasma environment is created to physically take away atoms from the target [47]. Argon is preferred inert gas used in plasma systems for its non-reactive nature.

For the first time, we have utilized a form of sputtering to deposit As_2S_3 on $LiNbO_3$ substrate, planar magnetron sputtering. The word planar comes from the relative position of target with respect to the substrate. The target and the substrate are parallel to each other in a horizontal way unlike vertical sputtering systems. The

magnet in the gun creates a magnetic field to sustain a path for atoms. Regular sputtering systems do not need a magnet because the target is vertically separated and the atoms easily find their way down to the substrate. Owing to its soft and brittle nature, applying high RF power causes very high deposition rates and target deformation. Magnetron systems use lower power levels and prevent deformation because of it.

The target is stoichiometric bulk glass obtained from Amorphous Materials Co. (Garland, TX). It is hand polished with a ruby-red color and 2 inch diameter. The distance between the target and the substrate is 3.5" and both are stationary during deposition. The applied RF power is around 15W and the forward and reflected power levels are tuned using an amplitude and phase matching network. 50sccm of argon gas is flowed into the chamber and 2mTorr pressure is obtained. Since the pressure level we are using is around 2mTorr it is hard to ignite the plasma with such a low power level. Keeping the flow rate and the power level the same, increasing the chamber pressure higher until the plasma ignites and lowering it back down 2mTorr keeps the plasma ignited. A thickness monitor is used to observe the deposition rate, which is around 1Å/s.

3.2.2 Chalcogenide Thin-film Characterization

Chalcogenide thin-film characterization is essentially needed because the material will be used as an optical waveguide. The most important characterization is the refractive index measurement, both real and imaginary parts (n vs. k). The real part relates to the effective index encountered by the fundamental mode which has a great impact on waveguide coupling and bending loss. The imaginary part (k) is related to the absorption coefficient of the material and to the intrinsic loss. A high absorption value leads to undesirable lossy waveguides.

Besides its refractive index information, the elemental composition and purity of the film have to be checked to confirm its quality, and this can be done by X-ray Photoelectron spectroscopy (XPS). In the XPS process, the photons emitted by a monochromatic X-ray source impinge on a surface or a thin film and causes adsorption by the core electron of an atom. If the photon energy is high enough the electron (or the photoelectron) will emit out of the surface with the energy

$$E_{kinetic} = h\nu - E_{binding} - \Phi \qquad (3.1)$$

where $h\nu$ is the photon energy, $E_{binding}$ is the binding energy of the electron, and Φ is the work function of the analyzer. $E_{kinetic}$ is directly measured by the analyzer that has a known Φ. Since As_2S_3 is a semi-insulating material, there exists positive charge after the photoelectrons are emitted out of the surface although most XPS systems are equipped with charge compensators. The shift affects the whole XPS spectrum and can

easily be identified by the carbon (C 1s) binding energy shift. Carbon is a contaminant subsisting on every surface to be analyzed and has a binding energy of 284.6eV.

XPS is also used to quantify the chemical composition, besides identifying the elements, because the number of photoelectrons of an element (As or S) is dependent upon the atomic concentration (%) of that specific element in the sample. As_2S_3 is an amorphous glass and is composed of Arsenic (As) and Sulfur (S) atoms. Two out of 5 atoms are arsenic while the remaining 3 atoms are sulfur, and this corresponds to 40/60 atomic concentration ratio. Since the atomic masses of *As* and *S* are 74.922 and 32.065 respectively, the mass concentration of *As* is 60.9% and the remaining 39.1% is sulfur's.

Generally the most intense peaks of elements are results of photoelectron emission from the most outer shell of the atom. It is the *3d* level for arsenic while it is *2p* for sulfur. The electron shell configurations of *As* and *S* elements (Table 3.1) are:

Table 3.1. Electron shell configurations of arsenic and sulfur.

Arsenic			Sulfur	
$1s^2$			$1s^2$	
$2s^2$	$2p^6$		$2s^2$	$\mathbf{2p^6}$
$3s^2$	$3p^6$	$\mathbf{3d^{10}}$	$3s^2$	$3p^4$
$4s^2$	$4p^3$			

Elemental arsenic and sulfur have specific XPS spectrums, which have been studied [48-51]. Arsenic and sulfur compounds (such as As_2S_3, As_2O_3, SO_2, ZnS) exhibit a shifted spectrum compared to elemental compositions. A correct way of interpreting

XPS spectrum of magnetron sputtered As_2S_3 is to compare it to the results discussed in the literature [48, 51] and to the XPS spectrum of the sputter target. We have examined 3 deposited samples and a piece from the sputter target and compared their *As* peaks to each other (Fig. 3.7). The locations of the peaks are adjusted to adventitious carbon on the surface.
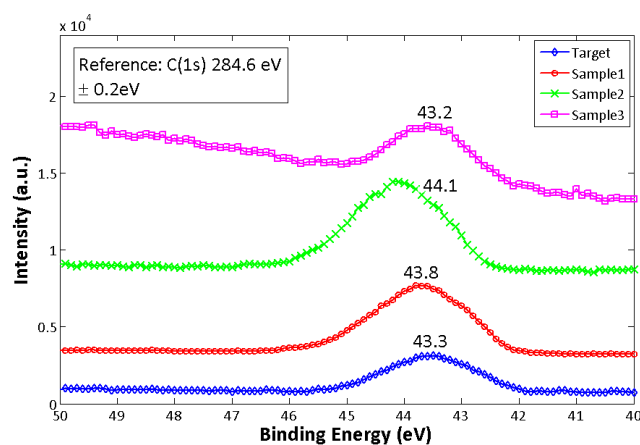
Figure 3.7. Binding energy of As (3d) in As_2S_3.

The peaks of sample1 and sample2 are shifted positively while sample3 has almost the same peak location as the target. Bahl *et al.* reports As peak in As_2S_3 to be 43.4eV [48] which overlaps with our results. The shifts in samples 1 and 2 are attributed to arsenolite (As_2O_3) formation confirmed by XPS data fitting (Fig. 3.8) and atomic concentration ratios (Table 3.2).
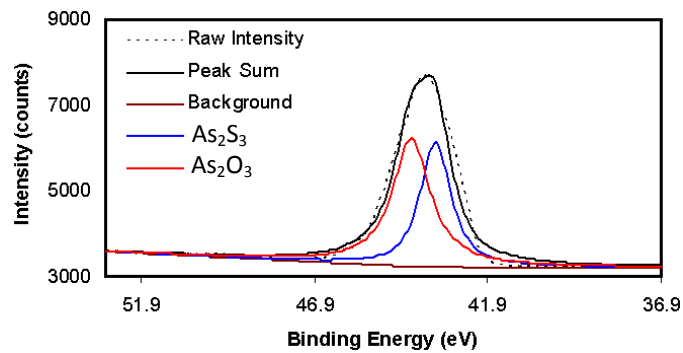
Figure 3.8. Oxygen content on the deposited As_2S_3 confirmed by XPS.

Table 3.2. Atomic concentrations of samples.

S (32.065), As (74.922)	Peak	Atomic Concentration (%) (±2%)
Sample1	S (2p)	53.15
	As (3d)	46.85
Sample2	S (2p)	54.81
	As (3d)	45.19
Sample3	S (2p)	61.68
	As (3d)	38.32
Target	S (2p)	59.39
	As (3d)	40.61

Arsenolites are formed as the result of oxidation during and after deposition and cause surface crystallites. The surface crystals are observed using scanning-electron and optical microscopy systems (Fig. 3.9) and can be a great source of optical loss if they interact with waveguides.
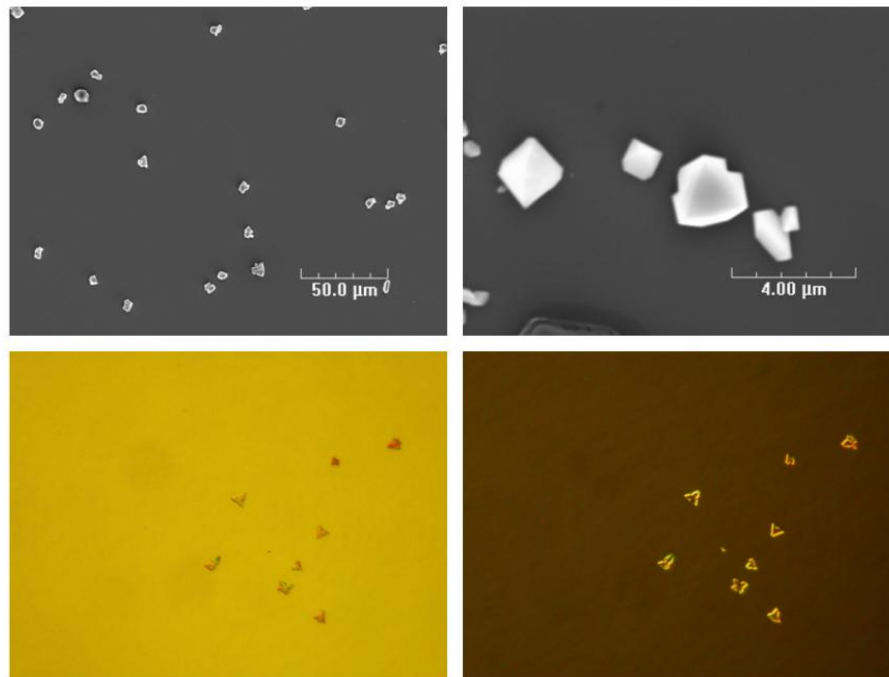
Figure 3.9. Surface crystals observed using both SEM and optical imaging.

We have changed our deposition recipe by increasing the flow rate, and the deposition system by preventing small leaks. The small leaks cause ambient air to enter the vacuum chamber during deposition and mix with the plasma ambient argon. Sample3 is deposited after all these modifications and has overlapping atomic concentration with the target. Later on, we have obtained XPS spectrum of several samples and have not observed any extraordinary shifts in their binding energy.

Another material characterization technique, especially for amorphous films, is an X-ray diffraction study that reveals if the deposited film has any crystalline phase. Although we check for microcrystals on the surface using an optical microscope, and composition using XPS, the amorphous quality of all of the monolayers of the thin film

can best be verified with XRD (Fig. 3.10). Since we do not observe any narrow and sudden peaks along the 2θ scan, we can easily say that our film is in amorphous phase.
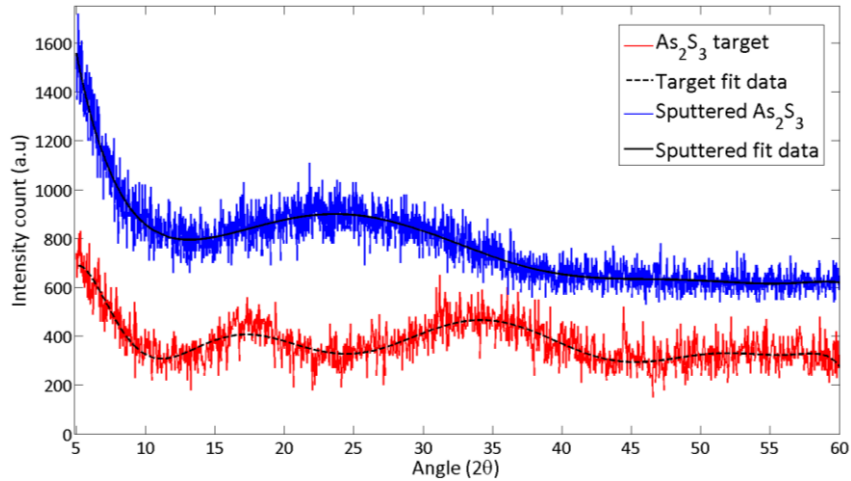
Figure 3.10. XRD data from target and sputtered thin films.

After checking the composition, amorphous quality and purity of the deposited thin film, refractive index measurements are performed. We have used two distinct methods to check the refractive index of As_2S_3, reflection spectroscopy and spectroscopic ellipsometer. Both methods also provide the film thicknesses very accurately. Refractive index ($\bar{n}$) can be written as

$$\bar{n} = n + ik \qquad (3.2)$$

where k is related to the absorption coefficient (α)

$$\alpha = \frac{4\pi k}{\lambda} \qquad (3.3)$$

If a material is a good absorber at a given frequency, the waves are strongly reflected at the surface. Dielectric materials are most reflective to light waves above their bandgap energy. Absorption in dielectrics is not desired and decays down as the wavelength increases.

A reflection spectrometer employs a broadband light source (350-800nm) and measures reflectance over the wavelength range. Thicker films exhibit more oscillations on reflectance spectrum than thin films which makes them more suitable for determining n and k. From reflectance, one can obtain optical constants by fitting the obtained data to the calculated data. The refractive index data from the F-20 system (Filmetrics, Inc.) is shown in Figure 3.11a.

In addition to reflectance spectroscopy measurement, ellipsometry is another reflectance technique to measure thickness and optical constants of thin films using a polarized light source. The incoming light on the surface is polarized to a known state and the reflected light goes through an analyzer before the detector which detects the change in polarization. Ellipsometer measurements give us Δ and ψ pairs as data where ψ is the amplitude change and Δ is the phase change. After the data is collected an optical model is constructed to compare generated and experimental data like the case of reflectance spectroscopy. Mean-squared error (MSE) which is a good indicator of the fit between modeled data and measured data is obtained. The Δ-ψ pair and the refractive index data from an ellipsometer in spectroscopic mode (Nanofilm EP3-SE, from Nanofilm Technologies GmbH) is shown below in Figure 3.11b-c.
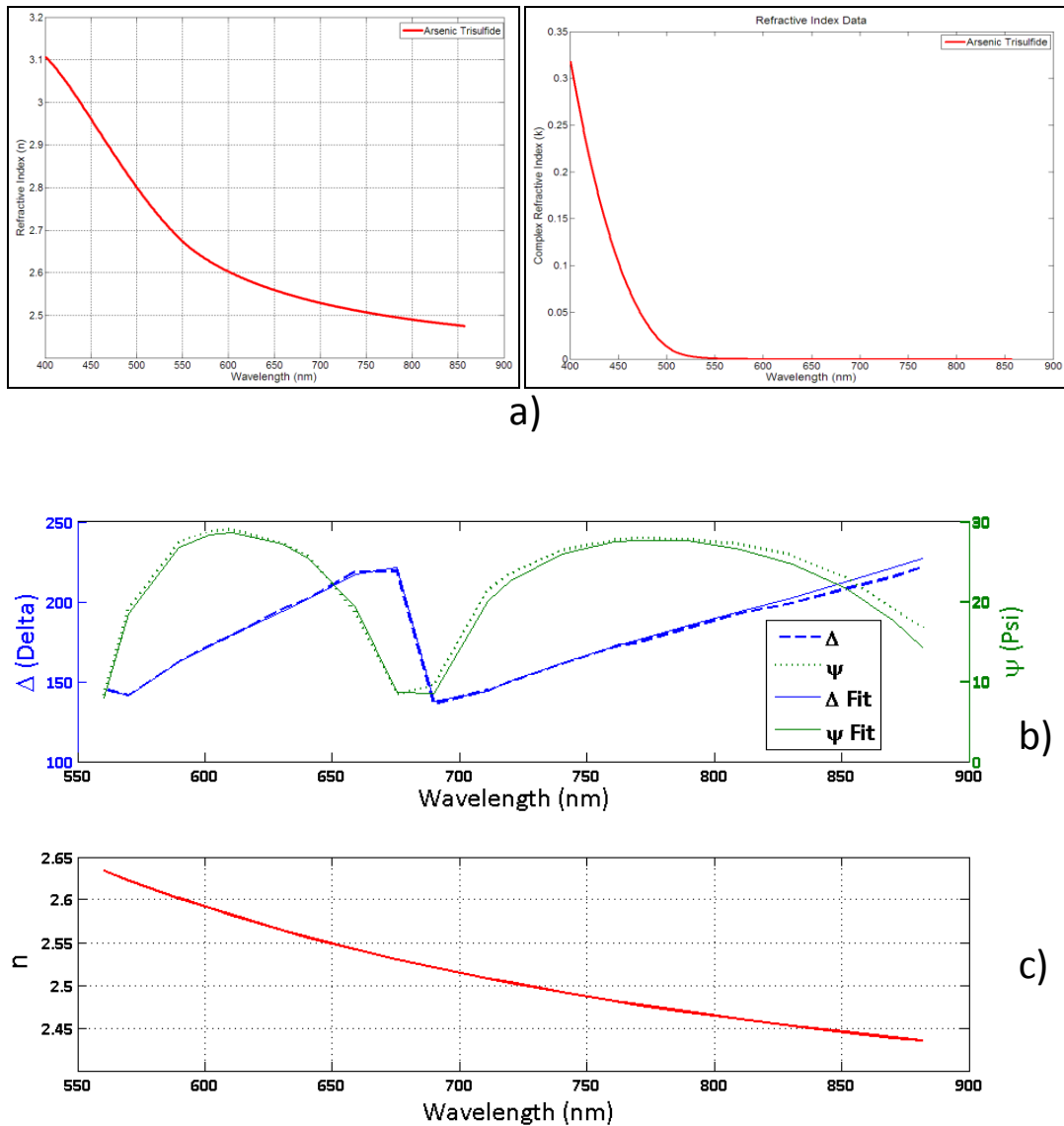
Figure 3.11. a) Refractive index of a 480nm thick As$_2$S$_3$ film extracted from reflectance spectrum measurement; b) Reflectance spectrum with fitted Δ and ψ pair; c) Refractive index of a 495nm thick As$_2$S$_3$ film extracted from ellipsometric spectrum measurement.

Both reflectance spectroscopy and ellipsometry depend on post-processing of the data in order to obtain thickness and optical constants. There are many models to represent n and k; Cauchy, Drude, and Amorphous Semiconductor are some of them.

The following Cauchy dispersion formula gives refractive index in terms of wavelength

and three coefficients, A, B, and C [52].

$$n(\lambda) = A + \frac{B}{\lambda^2} + \frac{C}{\lambda^4} \tag{3.4}$$

Cauchy coefficients are investigated for As_2S_3 [53], A=5.41, B=0.20, and C=0.14.

It is important to note that Cauchy relationship is a good model for frequencies below

the bandgap of the material where absorption coefficient is much lower.

3.2.3   Waveguide Formation Through Reactive-ion Etching

The last step before testing As_2S_3-on-Ti:$LiNbO_3$ waveguides is the formation of

rectangular shaped chalcogenide waveguides. The thin film acts as a planar waveguide

with no horizontal boundaries to support a bent waveguide mode and is not suitable

for practical applications. Rib shaped chalcogenide waveguides are already created

using wet etching where an alkaline solvent is involved [40, 44]. It is customary to use

dry etching to define waveguide shape due to controllability of the dimensions and

anisotropy. Reactive-ion etching (RIE) is a dry etching method where the reactive gases

are introduced to a plasma sustaining chamber under low pressure (10-100mT). The

reactive gases are chosen according to the etched material; the compounds formed

must have high volatility. Fluorinated gases (CF_4, CHF_3) are preferred for As_2S_3 since

AsF_x and SF_x are highly volatile as they have very low boiling points [24]. Inert species

(polymer) formed on the sidewalls of the etched material causes anisotropic etching

needed to created smooth and vertical sidewalls [47]. The inert species deposited on

the surface during etching are removed physically by using an inert gas (argon) because too much deposition on the surface may actually stop etching. RIE recipes developed in our lab are results of many tries as we inspected sidewall roughness, sidewall angle and etched surface roughness using hi-resolution scanning electron microscopy on silicon dummy samples. The same depositions steps are applied to 1x1cm silicon pieces and cleaved ends are inspected.

RIE experiments on As_2S_3 are already done using CF_4&O_2 mixture and CHF_3 [41, 54-55]. Since our protective coating (SiO_2+Ti) is different from what is used in the literature, the recipes developed will have to be adjusted accordingly. CHF_3 is a preferred gas to etch SiO_2 and can etch Ti as well [56]. Owing to more polymer deposition than CF_4, it is suitable for obtaining smoother sidewalls. Removed amount of *As* and *S* from the surface may not be the same due to *As-As* and *S-S* bonds in the amorphous glass and this may lead to surface roughness after etching [57]. Given that we remove all As_2S_3, improving the surface roughness is not so critical to our waveguide quality.

Besides obtaining smooth sidewalls, the final sidewall angle of the As_2S_3 waveguide has significant effect on the quality of the waveguide as the final mode profile and effective index of the fundamental mode change. There is also the unwanted polarization conversion when a waveguide with a slight angle is introduced a bent structure. The polarization conversion phenomenon is well documented in the literature and the tolerances for the sidewall angle are set [58-60]. The photoresist

after developing has an angle which replicates to the underlying SiO_2 and Ti protective layer (Fig. 3.12a). However, the sidewall angle of As_2S_3 waveguide is close to 90° when dry ething is proceeded further down (Fig. 3.12b). Recipes developed are presented in Table 3.3.
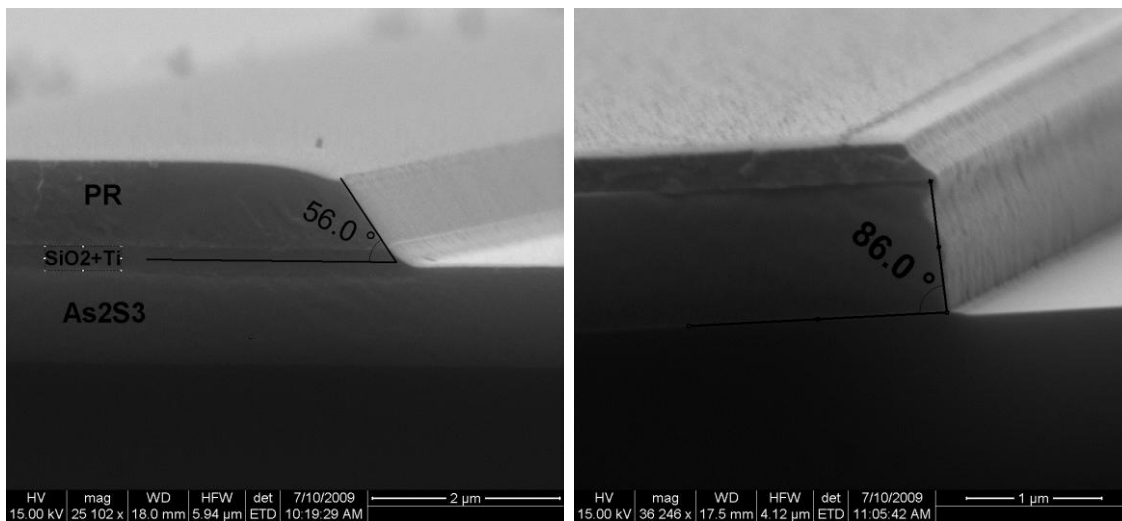
Figure 3.12. Photoresist and As_2S_3 sidewall angle after RIE. The PR is removed in the second picture using O_2 plasma.

Precise control of the etch depth of the As_2S_3 layer along the way is critical in order to prevent etching into $LiNbO_3$ surface. When etching is stopped before it reaches the surface and then continues all the way, we experience the "masking effect" revealed in figure 3.13a-b. The etched layer up to that point masks the underlying unetched As_2S_3 layer and creates an etching line. We believe this effect is a result of using photoresist as an etch mask and we designed a series of experiments in which we used a thin layer titanium as the protective layer and eliminated to usage of SiO_2.
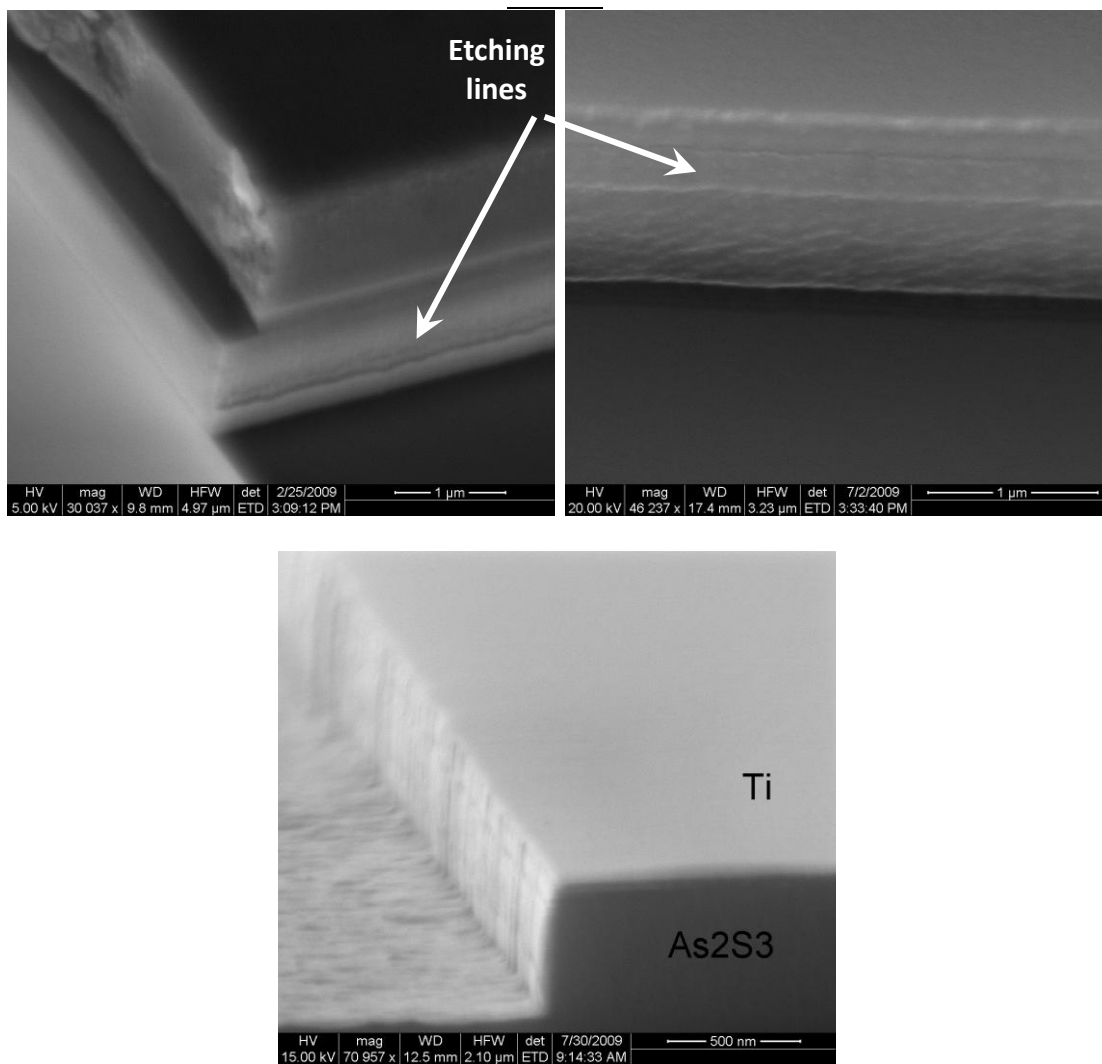
Figure 3.13. Masking effect created using photoresist and metal as mask layers.

We deposited 40-50nm of Ti on As_2S_3 using e-beam evaporation and we patterned our waveguide design on top of the metal using standard lithography. We etched Ti all the way and removed PR on it using acetone and quick O_2 plasma (i.e. ashing). Since the selectivity of Ti to As_2S_3 is very high, As_2S_3 is etched all the way before

Ti mask layer is consumed. Although we stopped two times during RIE, we do not experience a huge masking effect as we did with using PR as the mask (Fig. 3.13c).

Table 3.3. Recipes developed for As_2S_3 dry etching.

Sample size: 2x2cm	RF Power (Watts)	ICP Power (Watts)	Pressure (mTorr)	Gas Flow (sccm)	Etch Mask	Etch rate (nm/min)
Figures 3.11-3.12	100	200	10	CHF_3:30 Ar:5	PR and Ti	450-500
Figure 3.13a	100	200	20	CHF_3:10 Ar:30	Ti	100
Figure 3.13b	20	200	10	CHF_3:30 Ar:0	Ti	100
Figure 3.13c-e	100	200	10	CHF_3:30 Ar:5	Ti	500-550
Figure 3.14a-b-d	100	200	10	CHF_3:25 Ar:5	PR and Ti	400-450
Figure 3.14c	100	200	10	CHF_3:30 Ar:5	PR and Ti	500-550

We slowed down the As_2S_3 etch rate by changing the flow rate of flowed gases. By increasing Ar content to 30sccm and decreasing CHF_3 content to 10sccm, we slowed down the etch rate to 100nm/min but also obtained a huge undercut (Fig. 3.14a). As stated before, CHF_3 content is essential to prevent undercut due to polymer deposition. The other option to slow down the etch rate is to decrease the RF power to much lower levels. Adjusting RF power changes the DC bias voltage on the plate (i.e. automatic adjustment by the Oxford RIE system) the sample is placed on. A high DC bias induces a straighter path for ions and is critical for anisotropic etch profiles. The recipe change induced a very positive etch slope for As_2S_3 as depicted in figure 3.14b.
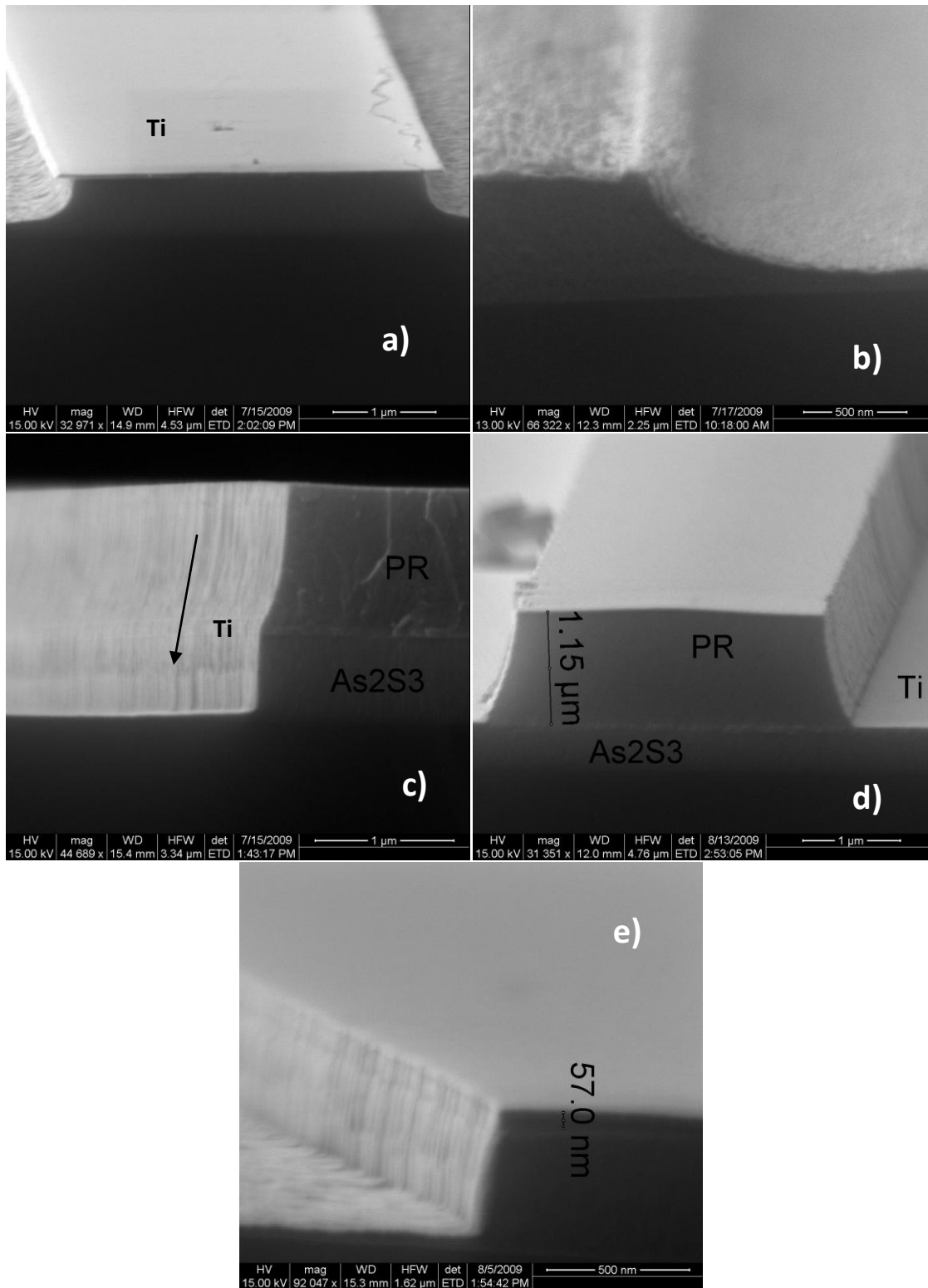
Figure 3.14. a) Recipe change created undesirable undercut; b) Recipe change created very positive etch profile; c-e) Sidewall roughness due to photoresist and Ti.

During SEM inspection, we realized that the source of sidewall roughness stems from the roughness on the sidewalls of the photoresist. In figures 3.14c-d, the sample was etched using PR as the etch mask and the lines on the sidewall of As_2S_3 layer follows the lines on photoresist. Although the period of sidewall roughness is much smaller than the wavelength of the light it can still create additional waveguide loss [4, 61-62]. Even when we remove the PR and use Ti as the etch mask, these lines do not disappear since they continue onto Ti layer as well (Fig. 3.14e). The roughness on the PR is also caused by the etching process and can be improved by adding ashing step (O_2 plasma to remove a small portion of PR) and having longer PR hard-bake time [63]. Our usual process does not involve either one of these and hard-bake time was only for 10-15min. Photoresist reflows and changes shape if hard-baked longer or at a higher temperature on a hot plate and it is much harder to remove it after the RIE step. The photoresist shape changed significantly when hard-baked 30min at 135°C in a hot oven or 2min at 145°C on a hot plate (Fig. 3.15). Adding 15sec of O_2 plasma (pressure: 40mTorr, flow: 40sccm (pure O_2), RF power: 100W) right before RIE significantly decreased the sidewall roughness (Fig. 3.15a-b-c).
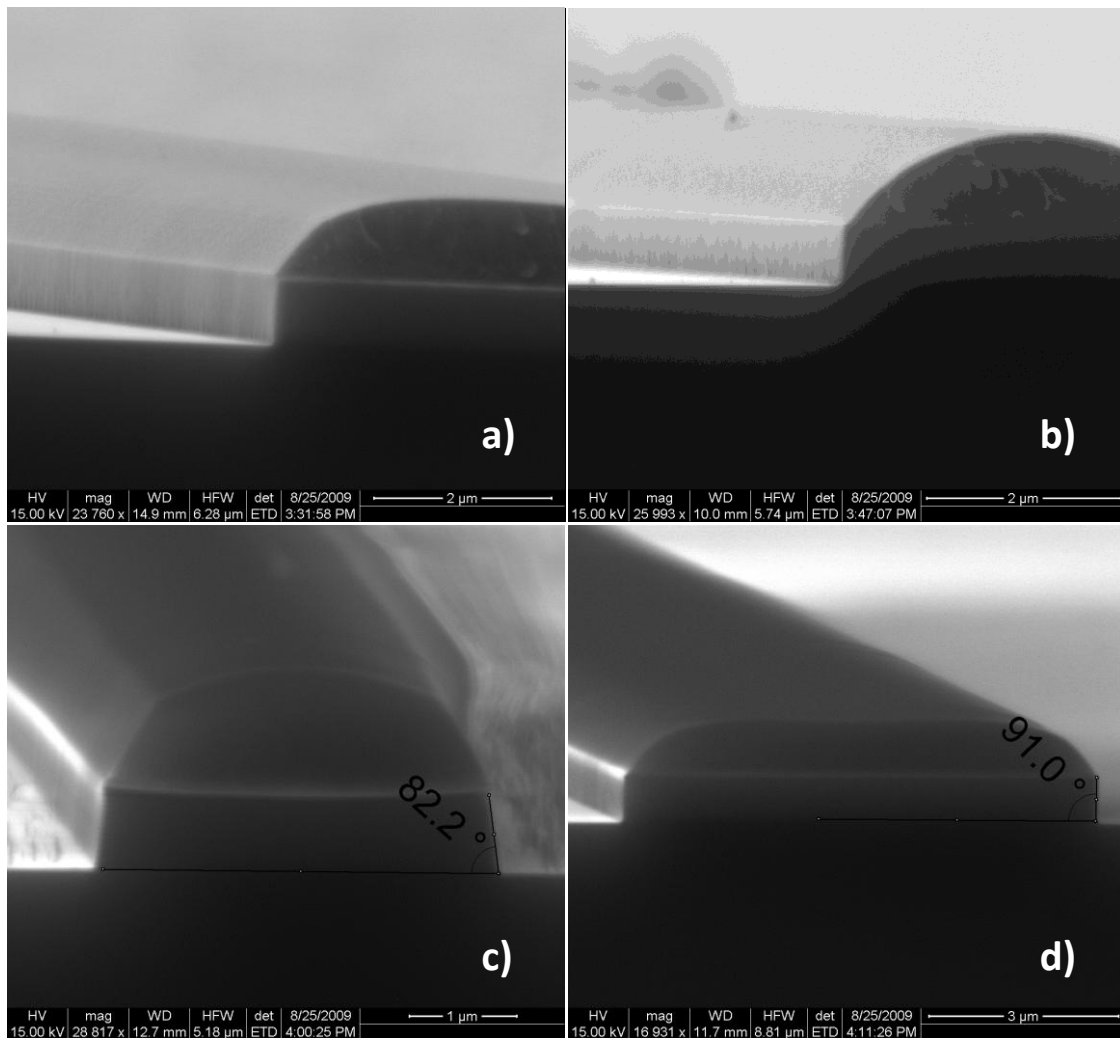
Figure 3.15. a) Sample sidewall with photoresist baked at 135°C for 30min in hot oven, 15sec O_2 plasma and RIE; b) Sample sidewall with photoresist baked at 145°C for 2min on hot plate, 15sec O_2 plasma and RIE; c) Etch recipe with CHF_3 flow rate of 30sccm; d) Etch recipe with CHF_3 flow rate of 25sccm.

As mentioned earlier, CHF_3 flow rate determines the sidewall angle of As_2S_3 waveguide and induces 6-8° of deviation from vertical sidewalls (Fig. 3.14e, 3.15c). By decreasing CHF_3 flow rate from 30sccm to 25sccm and keeping Ar flow rate the same (1/5 Ar/CHF_3 ratio), we are able to get almost vertical sidewalls (Fig. 3.15d).

The scattering loss due to rough sidewalls is analyzed in 2D [64], and 3D waveguides [65-66]. For low aspect ratio waveguides (or low height to width ratio), scattering losses are more prominent for TE polarized light than TM polarized light.

CHAPTER IV

RESULTS AND DISCUSSION[*]

4.1   S-shaped Bend Structures

Integrated optics requires bending structures that are essential parts of directional couplers, ring resonators, u-bends and other waveguide components. The bend radii reduction is critical to high density integration and enables more functionality to be brought on-chip. In general, waveguides with higher core confinement with respect to the surroundings can achieve smaller bend radii with low loss. The smallest bending structures [61, 68] reported to date have a substantially larger refractive index difference between the core and the cladding than can be achieved in standard, diffused lithium niobate waveguides.

In the case of Ti:LiNbO$_3$ optical waveguides, the small index difference in the diffused region does not allow tight bending structures with low losses. Typical bend radii are maintained at over 1cm in lithium niobate waveguides to minimize bend losses. We have proposed utilizing vertically integrated As$_2$S$_3$ on LiNbO$_3$ as a way to create smaller bend radii s-bends [69]. We demonstrate low-loss, transverse-magnetic (TM) polarization s-bend results for highly confined arsenic-trisulfide waveguides on top of Ti:LiNbO$_3$ waveguides. The optical mode inside Ti:LiNbO$_3$ waveguide transfers into As$_2$S$_3$ waveguide by the help of a tapering structure and goes through an s-bend before going back to a Ti:LiNbO$_3$ waveguide using a second taper identical to the first one. The TM polarization couples much more efficiently than the transverse-electric (TE) polarization for relaxed fabrication processes. Low-loss coupling of standard single-mode fiber into the Ti:LiNbO$_3$ waveguide is maintained without having to couple directly from the fiber into a highly confining As$_2$S$_3$ waveguide.

A thin titanium film is deposited on a bare x-cut y-propagating LiNbO$_3$ chip using DC sputtering. The thickness was measured to be 1100Å using a surface profilometer. Photolithography and reactive-ion etching of the titanium are used to define 7µm-wide strips for waveguiding at a wavelength of 1.5µm. Diffusion of titanium into LiNbO$_3$ is carried out in oxygen ambient at 1025°C for 10.5 hours. The end facets of the optical chip are polished to prepare it for optical waveguide testing.

As$_2$S$_3$ is deposited on the LiNbO$_3$ waveguide chip using RF sputtering. The thickness of the As$_2$S$_3$ layer is 400nm, and the refractive index is measured to be 2.56 at

a wavelength of 0.63µm. The film does not need annealing after deposition due to its good adhesion to the substrate and since its refractive index is close to that of the target. Since As_2S_3 dissolves in developer solution, it is necessary to protect it with a lower refractive index SiO_2 and a thin titanium metal layer, which is used to cover the porous SiO_2. SiO_2 and Ti depositions are done using e-beam evaporation. Photolithography is done on the titanium to define the As_2S_3 waveguides and is followed by reactive-ion etching that etches the Ti-SiO_2-As_2S_3 layers down to the $LiNbO_3$ surface. The remaining SiO_2 and Ti are removed using a diluted HF (Hydrofluoric acid) solution. The resulting structure is illustrated in Figure 4.1.
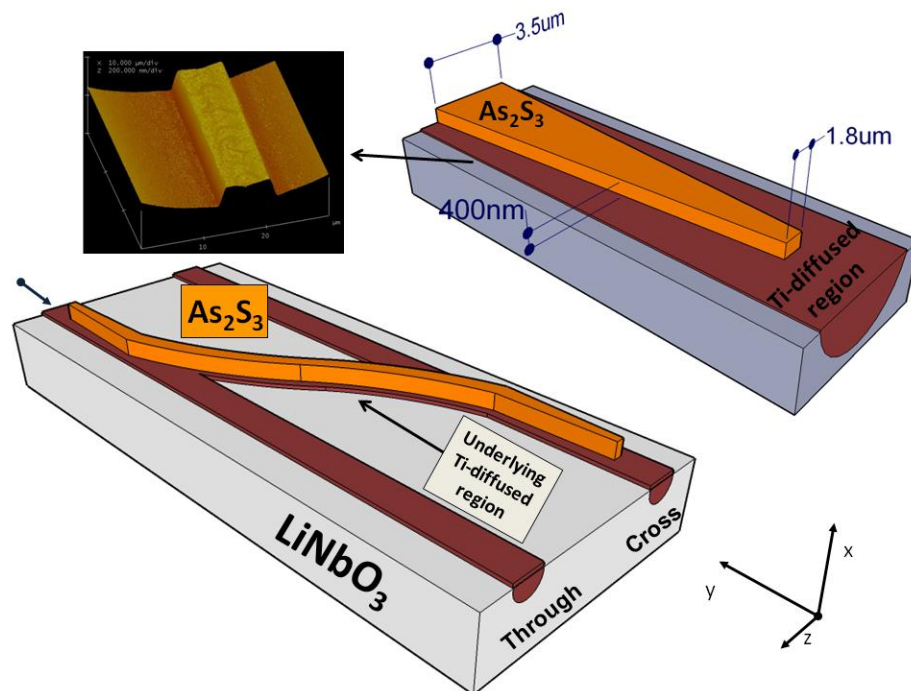
Figure 4.1. a) Vertically integrated As_2S_3 S-bend on $LiNbO_3$ waveguide chip with a zoom-in picture of the taper structure and an AFM picture showing the Ti bump after diffusion; b) Optical micrograph of a fabricated S-bend.
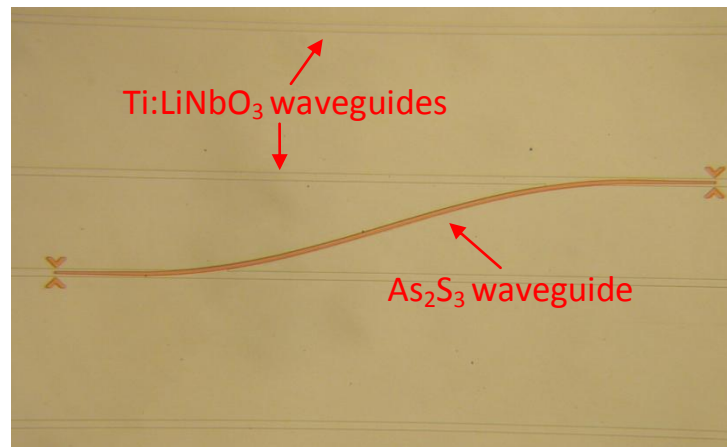
Figure 4.1. Continued.

The coupling region consists of a taper that is placed in the middle of the Ti:LiNbO$_3$ waveguide. The initial width of the taper is 1.8µm and increases to 3.5µm at the end of the taper. The first taper helps the optical mode inside the Ti:LiNbO$_3$ waveguide transfer to the As$_2$S$_3$ waveguide while the second taper at the end of the s-bend works the opposite way. Its length is fixed at 2mm in order to achieve efficient mode transfer. The taper structure is introduced to satisfy the phase-match condition, by tapering the starting point to minimally perturb the low-index contrast Ti:LiNbO$_3$ waveguide mode. Additionally the optical mode, once it couples up to the chalcogenide waveguide, does not couple back to LiNbO$_3$ until the end of the taper due to the gradual increase in the width. The 3D power transfer of the taper structure is simulated using finite-difference method algorithm (FDM) of FimmProp software (Fig. 4.2a-b). 99.8% of the input power is adiabatically transformed into a smaller mode by the end of the taper. Only 10% of the power is confined in As$_2$S$_3$ at the end of the taper while

most of the power is still inside the diffused waveguide. Figure 4.2c shows the intensity

profile of the Ti:LiNbO$_3$ fundamental mode while 4.2d has the mode at the end of the

As$_2$S$_3$ overlay taper. The mode evolution from can be easily shown using vertical electric

field profiles along the taper at various points (Fig. 4.2e). The mode shape getting

smaller and the peak amplitude increasing are signs of how the taper effects the mode

confinement.
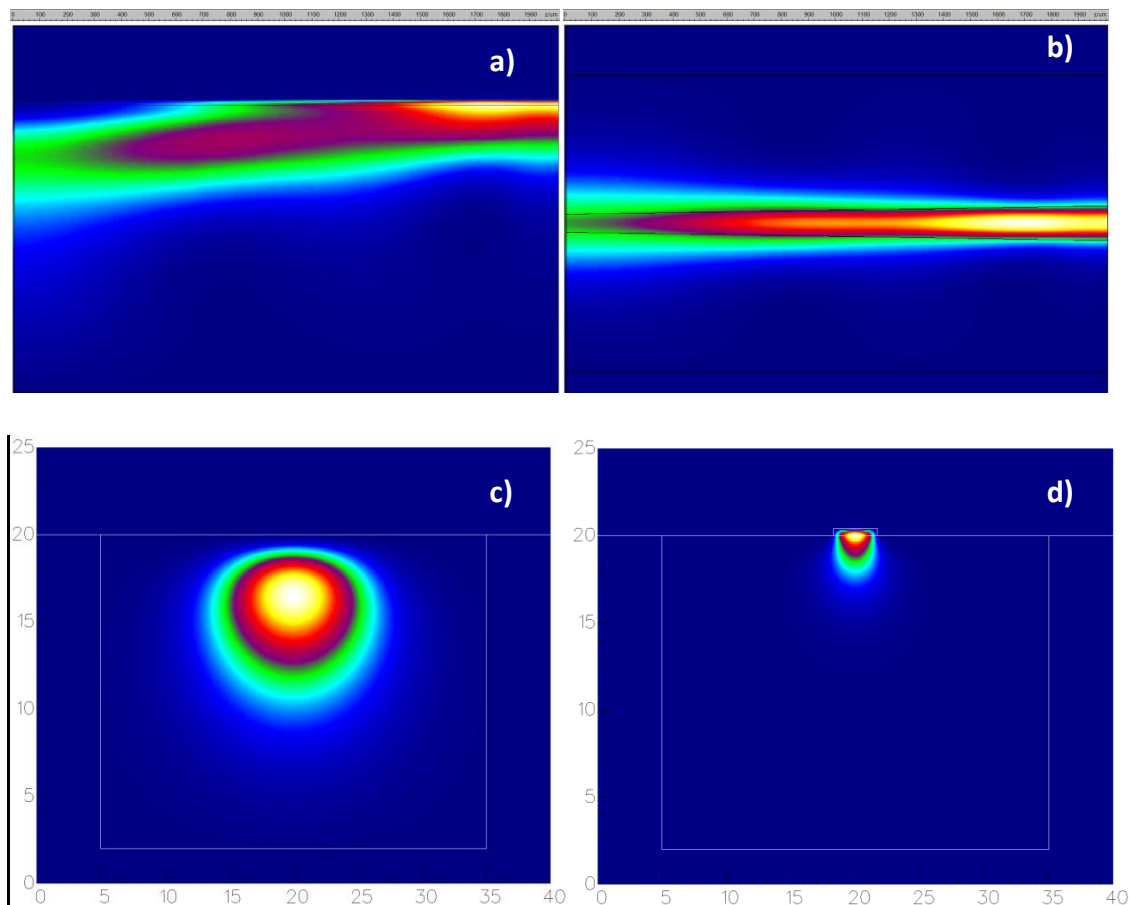
Figure 4.2. 2D-3D simulations of power propagation and transfer through a taper, a) Top view; b)Side view; c) Fundamental mode of Ti:LiNbO$_3$ waveguide; d) Fundamental mode of As$_2$S$_3$-on-Ti:LiNbO3 waveguide; e) Vertical electric field amplitudes at various distances along the taper.
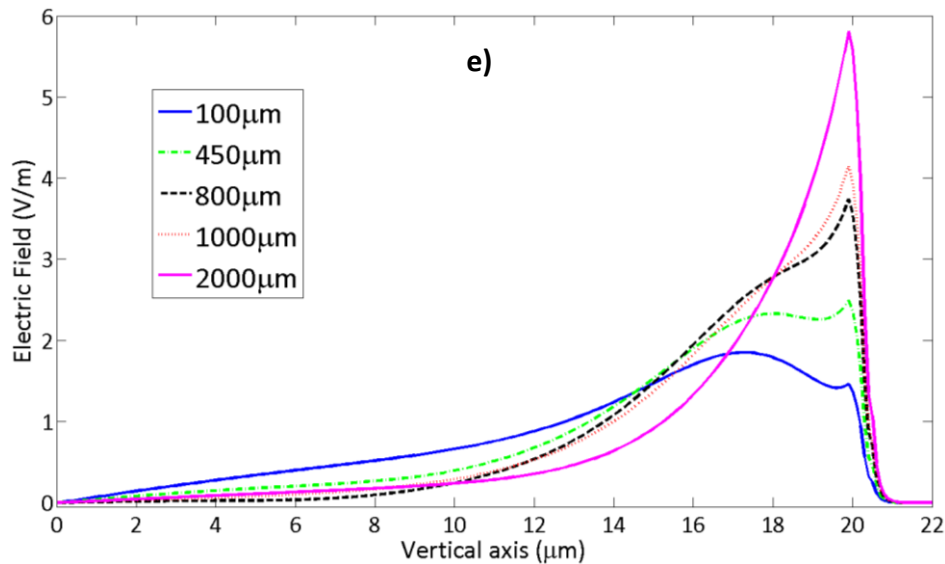
Figure 4.2. Continued.

Although all the titanium diffuses into LiNbO$_3$, during diffusion there arises a bump on the LiNbO$_3$ surface which has almost the same height as the initial Ti thickness as shown in the AFM inset of Figure 4.1. This creates a step discontinuity on the surface for As$_2$S$_3$ waveguide, which could result in excess waveguide loss. To overcome this problem, we introduced an underlying Ti diffused region that sits underneath the As$_2$S$_3$ waveguide and connects between the parallel Ti:LiNbO$_3$ waveguides. The underlying diffused region is only 4µm wide and does not strongly guide a mode at 1.55µm wavelength. Nevertheless, this region creates a perturbation for the straight Ti:LiNbO$_3$ waveguide, which results in additional insertion loss.

The s-bend is chosen to follow a cosine function [70] to minimize the curvature and thus the bend loss. The bend radius is minimal (though not zero) right after the taper and increases until the midpoint of the s-bend, where it is infinity. Consequently,

the bend loss is highest at the taper ends and constantly decreases until the midpoint, where it is negligible.

The Ti-diffused waveguides are tested by butt coupling light into the waveguide ends using a single-mode fiber. The laser source launched into the waveguides is a highly coherent laser that sweeps the wavelength from 1520 to 1570nm. There is no predefined axis of polarization of the light that is coming out of the laser source. Orthogonal polarization states relative to the waveguide substrate are generated by a polarization controller which is previously aligned with a bulk polarizer. The half and quarter wave plates inside the polarization controller have unique angles for both TE and TM polarizations. The insertion loss value of a waveguide is recorded using a DAQ card and Labview from National Instruments. The fiber-to-fiber insertion loss of a straight Ti:LiNbO$_3$ waveguide is measured for both TE and TM polarizations and is around 3dB. The discontinuity that is caused by the diffused region under the s-bend increases the insertion loss values of the straight waveguide, particularly for the TE mode.

In order to test the As$_2$S$_3$ s-bend on Ti:LiNbO$_3$, the LiNbO$_3$ waveguide chip is coupled to standard single-mode fibers at both input and output ends. The other two methods, direct fiber and prism coupling to As$_2$S$_3$ waveguide would generate a huge mode mismatch loss and would not be suitable for practical applications. The loss in the system is measured by aligning both input and output fibers and the fiber-to-fiber reference loss values, without an intervening straight waveguide, are subtracted from

the actual measurements. The loss values are recorded on both through and cross ports for both polarizations. Coupling of TE polarized light to the cross port was minimal. Figure 4.3 shows the insertion loss values at 1550nm for TM polarization at the cross port with and without the As_2S_3. Even without As_2S_3 overlay, there is negligible power propagating through underlying diffused region.
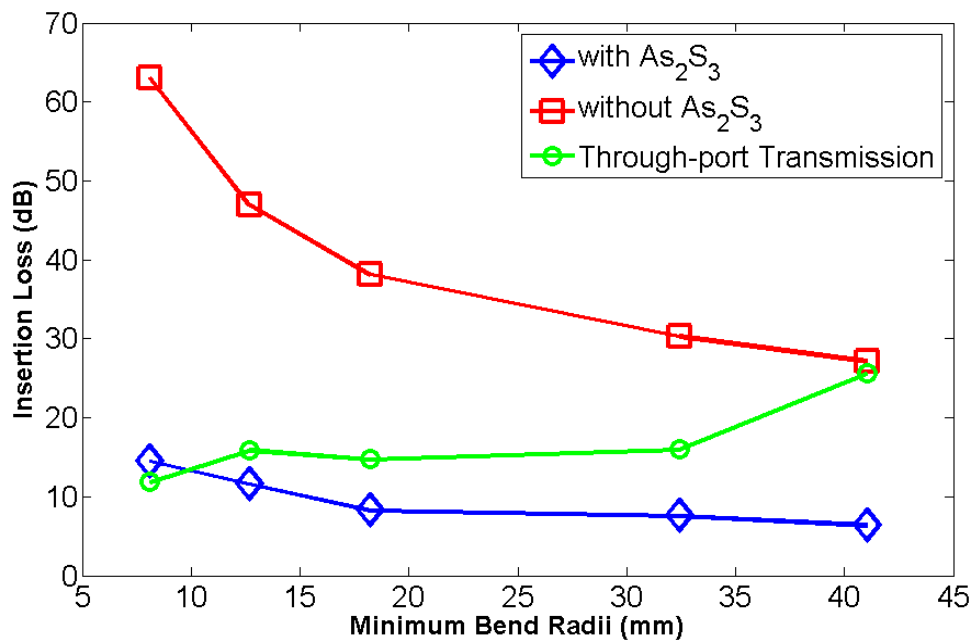
Figure 4.3. Insertion loss values of As_2S_3 S-bends on $LiNbO_3$ with and without As_2S_3. The bend radius plotted on the x-axis is the minimum along each s-bend. Input and output fiber-to-waveguide coupling losses are included as well.

It should be noted that the values in Figure 4.3 include the 3dB insertion loss associated with the fiber-to-waveguide coupling to straight $Ti:LiNbO_3$ waveguides. The angle of the tested s-bends goes from 1.27° to 2.86° while the typical angle used for $Ti:LiNbO_3$ y-branches or s-bends are below 1°. For the largest minimum bend radii, the

loss is only 2.5 dB once the average fiber-to-waveguide coupling loss contribution is removed. The s-bend loss values include taper loss, bend loss along the s-bend, loss due to the sudden transitions in radius of curvature (1/R) between the taper and s-bend, intrinsic material loss, and scattering losses due to sidewall roughness after RIE and any surface roughness on the Ti-diffused region. According to the results above, the bend loss contributes most to the overall loss as the s-bends get tighter.

The bend loss for the As_2S_3-on-Ti:$LiNbO_3$ waveguide was simulated for the TM polarization using conformal mapping method. The simulation results shown in Fig. 4.4 are for constant bend radii that correspond to the maximum curvature of the s-bend. Both experimental and simulations results confirm that with 400nm thickness the bend radii larger than 3cm is necessary to avoid huge losses through the s-bend. The intensity is not completely contained in the As_2S_3 overlay, as the confinement is just over 10%. A thicker film can be deposited to increase the confinement and lower the bend loss. By increasing the thickness to 0.5 µm, bend radii less than 500 µm should be achievable with low loss.

Although depositing a thicker film has a positive effect on bend loss, it may decrease the amount of power coupled into the overlay waveguide. In order to fully quantify the amount of power coupled to the As_2S_3 s-bend through the taper, we performed 2D and 3D simulations on the taper structure with two different methods. For the 3D full taper simulation, the tip width is changed from 0.5µm to 2.5µm and the power transferred to the end of the taper is calculated. A straight As_2S_3 waveguide with

variable width is used in the second simulation, and the 2D power overlap between the incoming Ti:LiNbO$_3$ mode and the mode profile of As$_2$S$_3$-on-LiNbO$_3$ section is calculated.
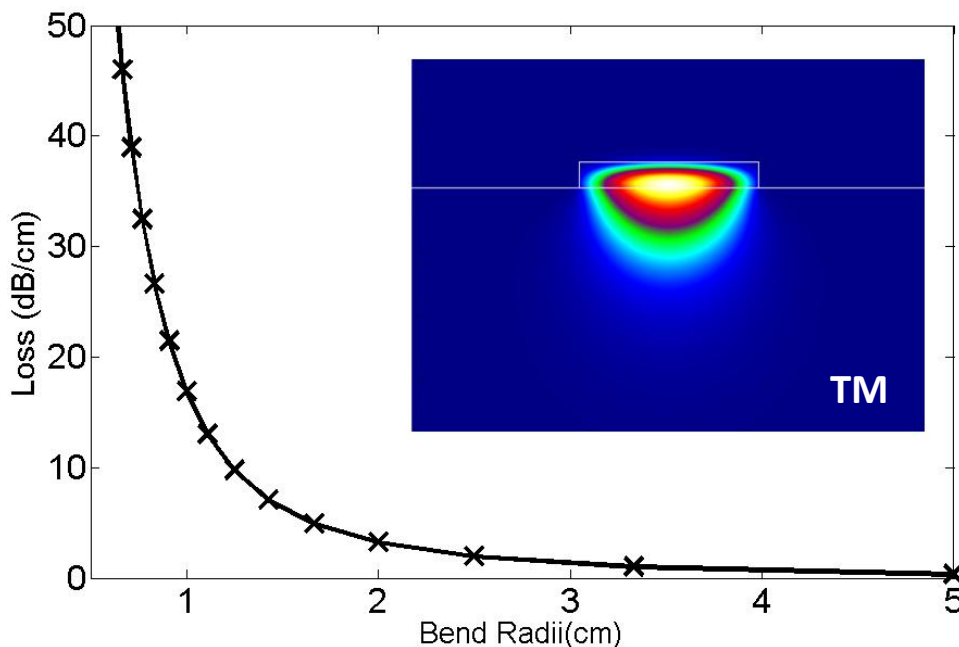
Figure 4.4. Bend loss simulation and 2D mode intensity picture of As$_2$S$_3$ on Ti:LiNbO$_3$ with 0.4x3.5µm dimensions for TM polarization.

The mode in the Ti:LiNbO$_3$ waveguide section is not fully transferred to the overlay waveguide for larger taper tips as indicated in Fig. 4.5. The TE polarized light did not couple efficiently to the As$_2$S$_3$ waveguide because the initial tip width of the taper was too large in our experiments. The TE polarization needs smaller tip widths (around 0.6µm) for a 0.4µm thickness for mode phase matching condition while 1.5µm is sufficient to couple 95% of the power for the TM polarized light according to the simulation results.
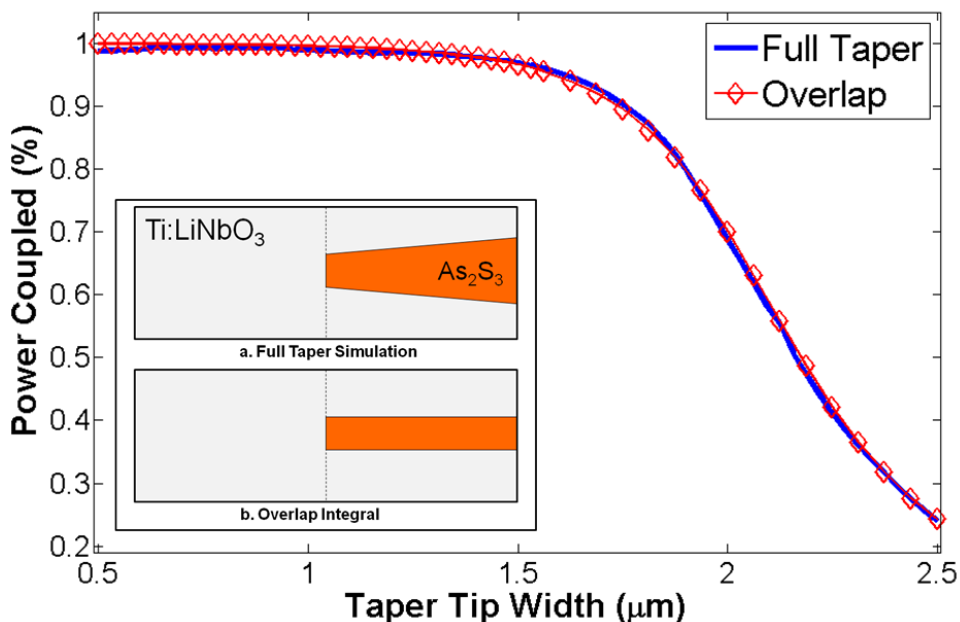
Figure 4.5. Two simulations comparing the power coupled into the As_2S_3 s-bend through the As_2S_3 taper. Maximum point corresponds to 100%.

The coupling loss for each taper is estimated from these simulations to be 0.6dB due to the 1.8µm average taper tip width that was achieved in our experiments. The experimental taper tip widths are quite uniform for all the s-bends. The excess loss of the remaining taper and s-bend structures, once the taper tip mode-coupling loss is removed, is estimated to be only 1.3 dB.

The performance of the tapers can be enhanced by fabricating smaller tips, which also allows for efficient coupling into a thicker As_2S_3 layer. Therefore s-bends with bend radii smaller than 3cm can be easily fabricated. The abrupt change in curvature at the beginning of the s-bend does not contribute much to the overall loss

for these bend radii but will be the dominating loss for bends smaller than about 500µm.

The TE transmission through the s-bend (cross port) is minimal; whereas, it is dominantly transmitted to the through port. The behavior resembles a polarization beam splitter as shown in Fig. 4.6. For practical application as a polarization beam splitter, the extinction ratio would need to be improved further. The extinction ratio decreases with increasing wavelength.
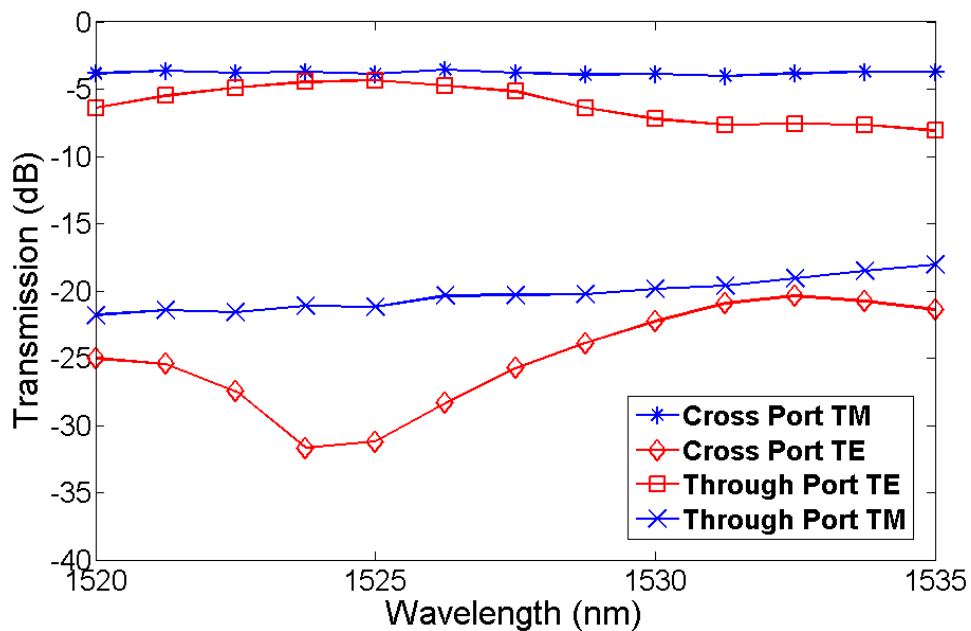
Figure 4.6. Insertion loss of an s-bend for the through and cross ports for both TE and TM polarizations.

We have demonstrated a novel approach to improve the bending performance of titanium diffused $LiNbO_3$ waveguides using vertically integrated As_2S_3 waveguides. A

taper structure is introduced to perturb the optical mode inside the Ti:LiNbO$_3$ and gradually transfer it in and out of the As$_2$S$_3$ waveguide. An excess loss of 1.3dB is estimated for the overlay waveguide, once the loss contribution of the finite taper tip widths is removed. Much smaller bend radii are achievable compared to what can be realized with typical Ti:LiNbO$_3$ waveguides, thus enabling higher integration densities to be attained on this important electro-optic waveguide platform.

4.2   Ring Resonator Waveguides

This portion of the fourth chapter presents and discusses the As$_2$S$_3$ ring resonators vertically stacked on LiNbO$_3$. Some parts of the following text is adapted from [71].

The lithium niobate (LiNbO$_3$) waveguide technology has evolved since the 1970s when titanium diffusion was first introduced [72]. Its electro-optic effect is being utilized widely in current modern telecommunication systems, as it is still the backbone of many optical networks for high-speed amplitude and phase modulators. While it has enabled the integration of advanced modulators, lithium niobate waveguide technology cannot produce optical filters with compact feedback paths. This is not possible using titanium-diffused or ion-exchanged waveguides since the waveguide modes in LiNbO$_3$ have much lower confinement due to their size and the material refractive index difference ($\Delta n \sim 10^{-3}$). Although feed-forward filters such as gratings and Mach-Zehnder interferometers have been fabricated using Ti-diffusion, ring resonators on LiNbO$_3$ with small radius have not been realized until recently [13-14]. Both papers

focus on increasing the optical confinement in $LiNbO_3$ through ridge waveguide designs since the smallest ring resonator using regular titanium diffusion approach has 30mm radius [73]. However, ring resonators on silica, silicon and III-V systems have been extensively studied for optical filter designs [74-76], ring lasers [77-78], and liquid sensing applications [79-80].

4.2.1   Rings with Taper to the Side

We reported the first feedback optical filter fabricated with arsenic-trisulfide (As_2S_3), a chalcogenide glass, integrated onto a $LiNbO_3$ substrate [71]. To overcome the low mode confinement of $LiNbO_3$ waveguides, we vertically integrate waveguides with a core material of As_2S_3, a chalcogenide glass with a refractive index of 2.4 compared to 2.2 for $LiNbO_3$. These vertically-integrated waveguides are capable of low-loss bend radii on the order of 100 microns. The mode confinement may be adjusted between the As_2S_3 and $LiNbO_3$ materials by varying the As_2S_3 waveguide thickness and width. Thus, a substantial portion of the mode may be designed to remain in the $LiNbO_3$ so that efficient electro-optic tuning can be achieved.

As_2S_3-on-$LiNbO_3$ waveguide fabrication begins with creating Ti-diffused waveguides. A titanium thickness of 950Å is sputtered on a diced x-cut y-propagating $LiNbO_3$ chip and is diffused for 9.5 hours in wet breathing air ambient. The end facets of the waveguide chip are then polished to optical quality and Ti-diffused waveguides are tested by end-coupling single-mode fibers. The fiber-to-fiber insertion loss of a typical waveguide is 2.5±0.5dB. A thin film of As_2S_3 is deposited on the $LiNbO_3$ using RF

magnetron sputtering with a 1Å/s deposition rate to result in 4700Å total thickness. A protective layer of SiO_2 and Ti is covered on the chalcogenide thin film to prevent dissolution of As_2S_3 in photoresist developer. Contact photolithography is used to pattern on the titanium and a subsequent reactive-ion etching step forms the As_2S_3 ring structure. The race track ring structure is revealed after the protective layer is removed using hydro-fluoric acid (Fig. 4.7a). The optical micrograph of the race track structure is shown in Fig. 4.7b, which is an allpass architecture ring with no coupling to the upper parallel Ti:LiNbO$_3$ waveguide as it is far away from As_2S_3 ring.
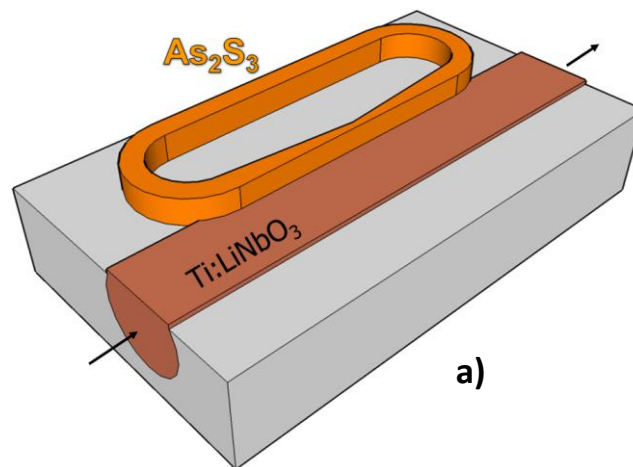
Figure 4.7. Vertically integrated As_2S_3 race-track ring resonator on LiNbO$_3$ waveguide chip. (a) Schematic; (b) Optical micrograph; (c) SEM image showing As_2S_3 ring approaching Ti:LiNbO$_3$ waveguide.
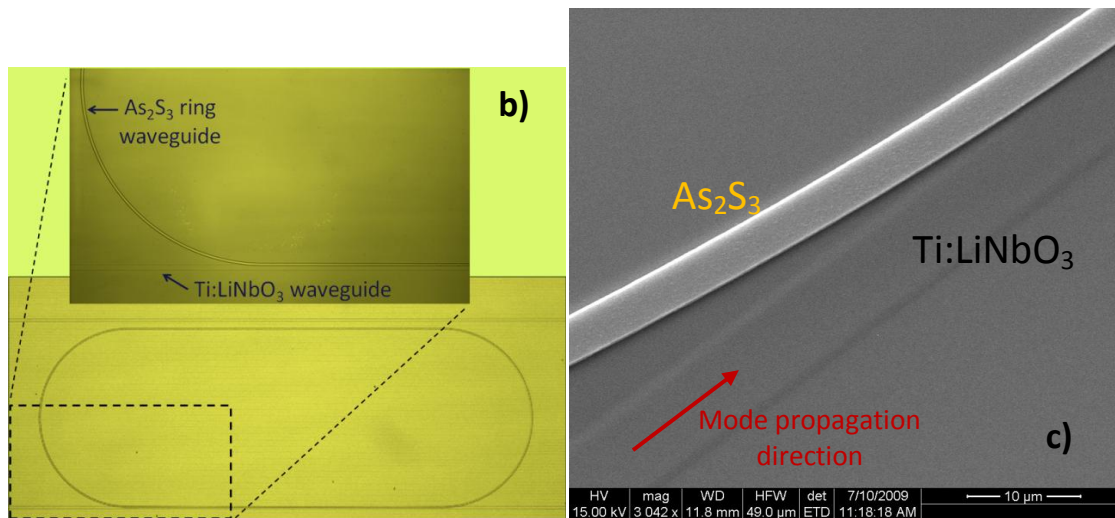
Figure 4.7. Continued.

This configuration uses a single coupling region between the input/output Ti:LiNbO$_3$ waveguide and the As$_2$S$_3$ ring resonator. If the feedback path is lossless, then this structure yields an ideal optical allpass filter. Optical allpass filters are building blocks for creating higher-order optical bandpass filters that have optimal filter design characteristics, such as those associated with the Chebyshev and elliptic filters that are well-known in digital signal processing. In practice, the loss encountered for each roundtrip of propagation breaks the pole/zero symmetry of the ideal allpass filter and creates both a wavelength-dependent amplitude and phase response.

The vertical coupling occurs with the help of back-to-back taper structures. The taper width starts from 1µm and increases to 3µm, which is the width of the ring waveguide. The taper design helps to reduce the effective index mismatch between the Ti-diffused waveguide and As$_2$S$_3$ waveguide, and thereby increase the coupling into the

ring. The 3D power transfer of a 750µm taper structure is simulated using finite-difference method algorithm (FDM) of FimmProp software and the views from the side and the top are shown for TM polarized mode (Fig. 4.8a-b). The 2D waveguide at the end of the taper supports 2 modes (Fig. 4.8c-d) and the mode profile at the taper end is the superposition of these modes. 32.4% of the power is coupled to first mode that is mostly confined in As_2S_3 overlay while 65.5% of the power stayed in Ti-diffused waveguide. Due to dual modes, mode beating phenomenon is observed along the taper. The power confinement is 37.2% inside As_2S_3 waveguide at the end of the taper while most of the power is still inside the diffused waveguide. Figures 4.8e-h shows the 2D intensity profiles of the propagating optical mode and its interaction with the side taper at 100, 250, 400, and 750µm distances. The percentage of power coupled up to As_2S_3 increases with taper length due to increasing adiabacity.
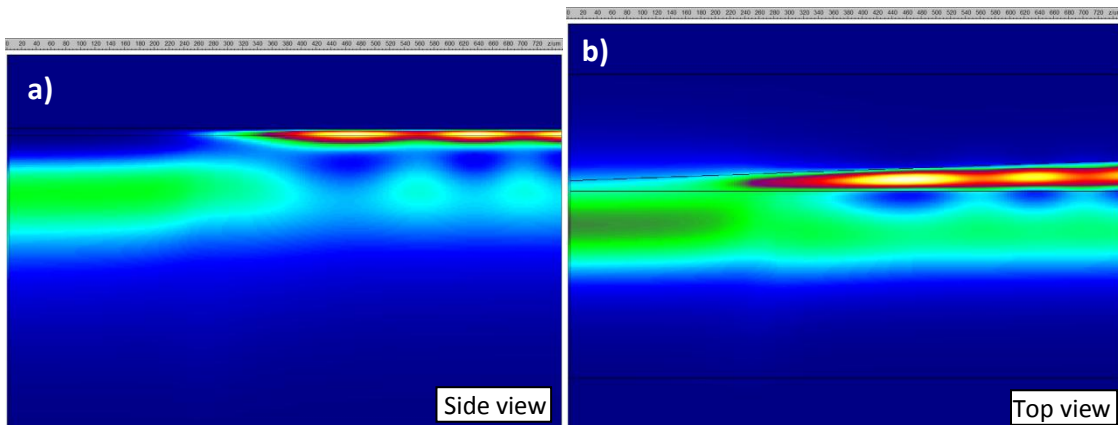
Figure 4.8. 2D-3D simulations of power propagation and transfer through a taper, a) Top view; b)Side view; c)50µm; d) 150µm; e) 250µm; f) 500µm; g) 750µm; h) Coupled power as a function of taper length.
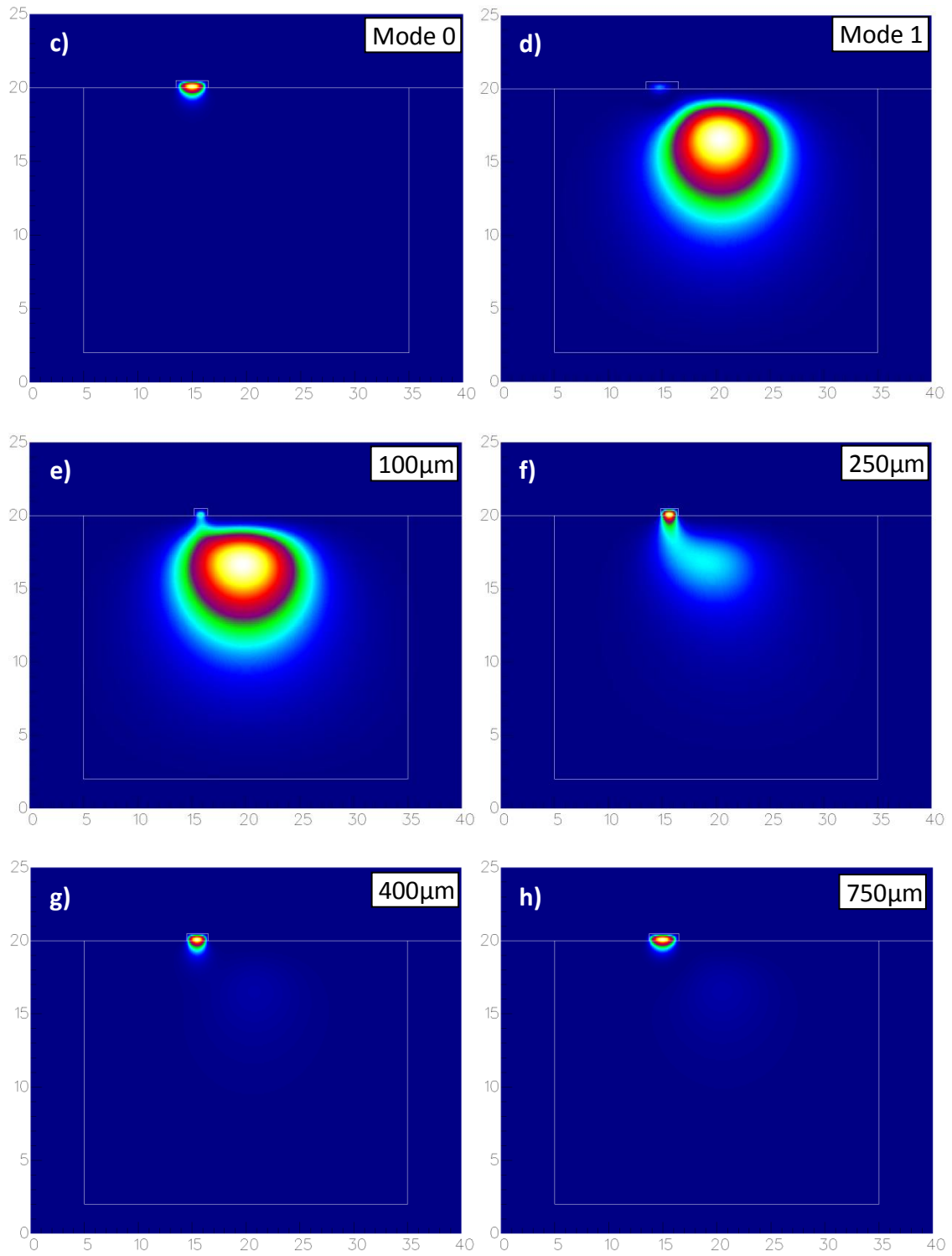
Figure 4.8. Continued.

Looking at modal effective indices along the taper will help us understand the coupling mechanism. We have solved As_2S_3-on-Ti:$LiNbO_3$ structure in 2D using finite-difference method and obtained the effective index values from 1µm to 3µm (Fig. 4.9), in order to enhance our trust to the results presented in the previous figure by 3D propagating mode solver. The fact that the n_{eff} of As_2S_3-on-Ti:$LiNbO_3$ waveguide asymptotically approaches Ti:$LiNbO_3$ waveguide, justifies the coupling phenomenon.
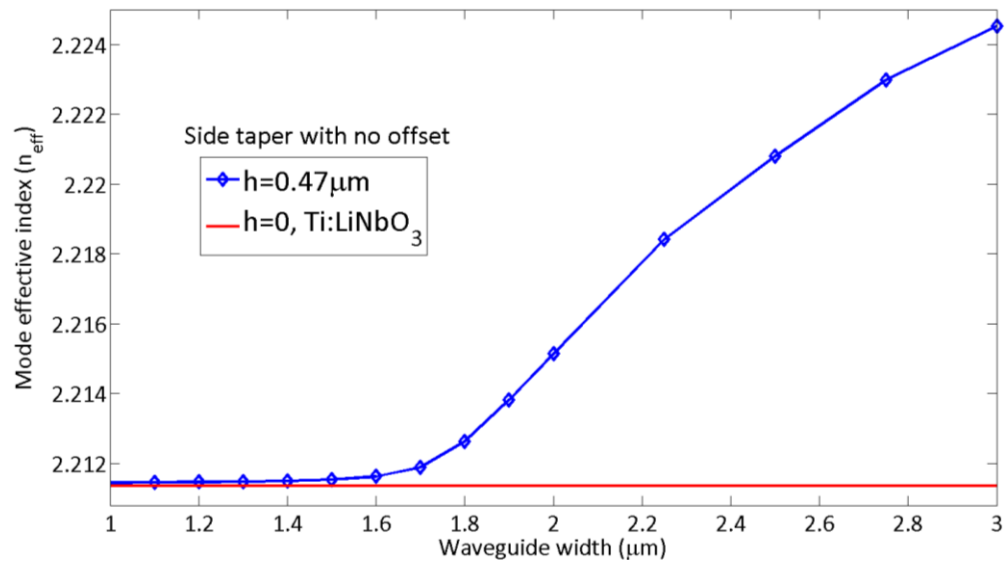
Figure 4.9. Effective index values of TM polarization extracted from solving As_2S_3-on-Ti:$LiNbO_3$ waveguides in 2D.

The taper length (750µm) and the ring diameter (581.6µm) together correspond to a circumference of 4.827mm and free-spectral range (FSR) of approximately 25.4GHz. After fabricating several ring structures with different offsets and taper dimensions, our measurement results show that the power transfer is best if the

chalcogenide waveguide slightly overlaps or sits next to the diffused waveguide (Fig. 4.10a). As can be seen, the diffused region creates a small bump after diffusion and this creates a discontinuity for the As_2S_3 ring waveguide. An atomic force microscopy (AFM) image clearly shows the bump resulting from titanium diffusion and the overlap of the chalcogenide waveguide (Fig. 4.10b). The mode overlap increases when the ring waveguide overlaps the Ti-diffused waveguide.
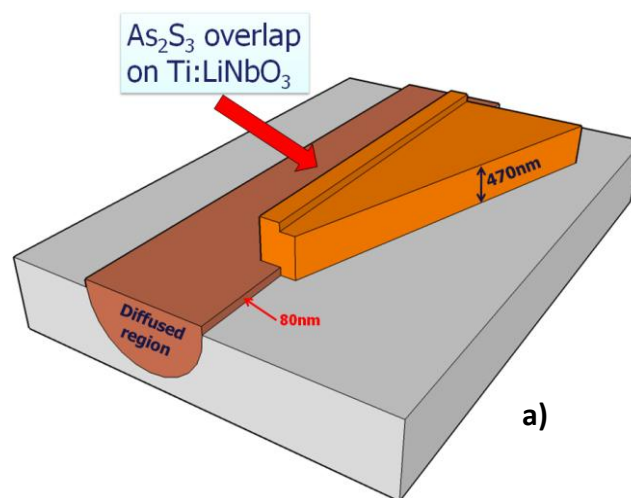
Figure 4.10. (a) Schematic As_2S_3 taper structure and its overlap on Ti:LiNbO$_3$ waveguide; (b) AFM picture of the ring starting to overlap on Ti:LiNbO$_3$ waveguide.
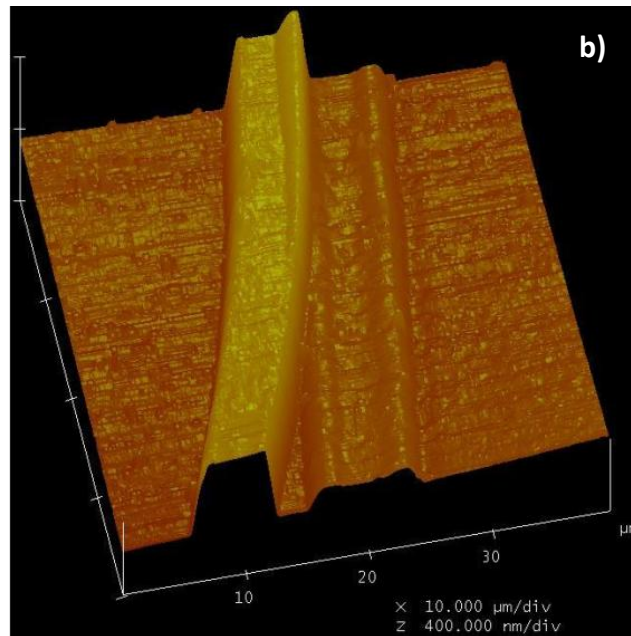
Figure 4.10. Continued.

As stated in Chapter I, in order to determine the power coupling ratio (c) and the roundtrip loss (γ), the magnitude response is not enough by itself because it does not provide a unique solution, i.e. whether the zero is a maximum-phase or a minimum-phase [23]. We measured the magnitude response and group delay of the As$_2$S$_3$ ring using a LUNA Technologies Optical Vector Analyzer (OVA) with a tunable laser source, and fitted the responses to extract the coupling coefficient and round-trip loss values (Fig. 4.11). Fitting is done over four free-spectral ranges at the center wavelength of 1522nm. The OVA measures the full Jones matrix of a device under test. We use a polarizer as a reference to establish the incoming TE and TM polarizations to the waveguide under test. Since the tunable laser source is highly coherent, the Fabry-

Perot ripples originating from the polished LiNbO$_3$ chip are evident although an index matching liquid is used to reduce these ripples.
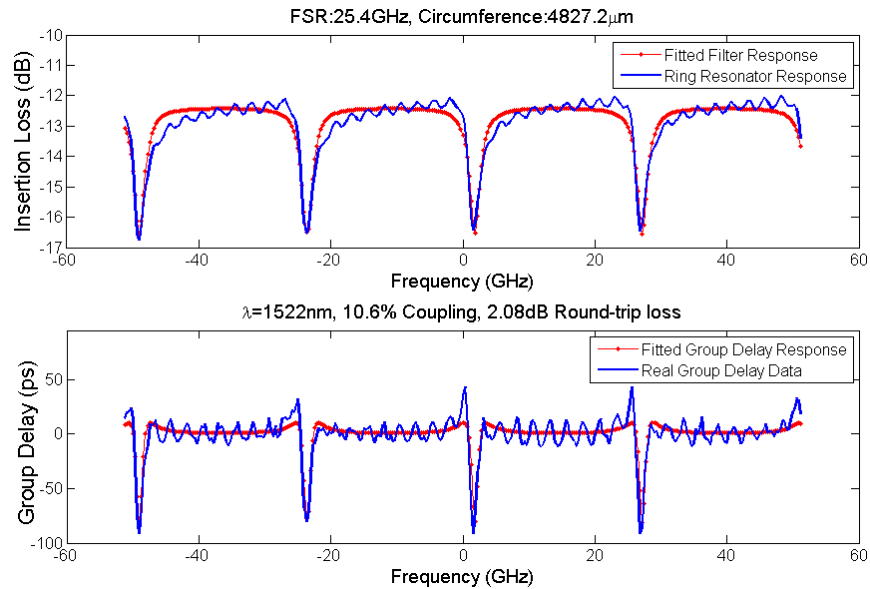
Figure 4.11. Transmission and group delay responses through As$_2$S$_3$-on-Ti:LiNbO$_3$ ring structure.

The zero is a minimum-phase zero (i.e. $\gamma/c < 1$) since the group delay near resonance is negative. The calculated power coupling ratio and roundtrip loss are 10.6% and 2.08dB respectively for TM polarization. The coupling ratio (κ) and As$_2$S$_3$ film thicknesses are inversely related, and thickness has a great impact on bend loss performance of the ring as it improves the roundtrip loss. The excess roundtrip loss is attributed to the discontinuity created by the diffused waveguide and sidewall roughness of the ring waveguide due to reactive-ion etching. We have simulated optical loss created by the diffused waveguide post diffusion height in 3D dimensional analysis for TE and TM polarizations (Fig. 4.12).

TM optical loss through a Ti-Bump for several As_2S_3 thicknesses

TE optical loss through a Ti-Bump for several As_2S_3 thicknesses
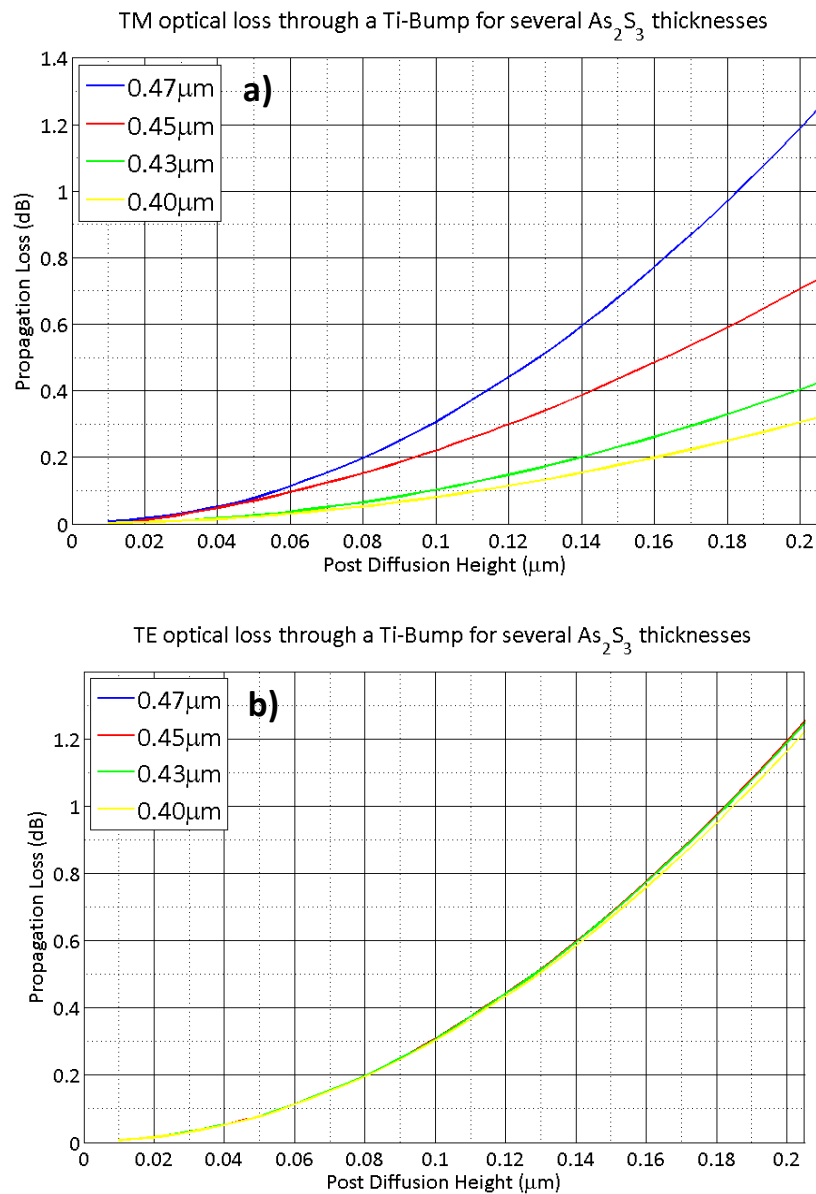
Figure 4.12. Simulated power loss created by the discontinuity of As_2S_3-on-Ti:LiNbO$_3$ ring structure at 1.55µm wavelength: a) TM; b) TE.

TM polarized light is more affected more from the discontinuity as the waveguide height increases. TE polarized light, on the other hand, experiences the same loss for the several thickness values. Typical loss value additionally induced to the ring roundtrip loss for both polarizations is 0.6dB/roundtrip (0.3x2). Simulations also

show that a smaller initial taper width (w_i < 0.8μm) increases the coupling ratio for TM polarization [67], and allows TE polarized light to couple into As_2S_3. The same simulation in figure 4.8 with the same taper dimensions is done for TE polarized light and the amount of coupling was less than 1%. As demonstrated in Chapter II, the TE mode can go through tighter bends with lower losses, which in turn makes it possible to fabricate even smaller As_2S_3 rings. We suspect bringing the initial taper width down will also allow us to align the As_2S_3 waveguide with less overlap on the diffused layer in order to reduce the roundtrip loss. The roundtrip loss can further be reduced with an optimized etching process. With improvements in the roundtrip loss, this integrated structure will find many applications in current telecommunication systems and analog photonic processing.

We have designed a photomask so that the rings would have different overlaps on the diffused waveguide. The overlap would vary from -2μm to 3μm gap, where -2 means a 2μm gap between the As_2S_3 ring and the post diffusion height. The results are given in table 4.1 and reveal a pattern; more overlap results in more power coupling into the ring resonator but also induces more roundtrip loss. The ring resonators did not have resonances even when there was a slight gap.

Table 4.1. Power coupling and roundtrip loss as a function of As_2S_3 overlap on $Ti:LiNbO_3$.

Radius (μm)	λ (nm)	FSR (GHz)	Overlap (μm)	κ (%)	Roundtrip Loss (dB)
290.8	1522	25.4	1	10.6	2.08
284.8	1554.4	32.5	2	22.3	3.9
284.8	-	-	3	-	Loss too much to measure
290.8	1568	25.4	2.2	27	5.68
284.8	1499.5	32.5	2.2	30.6	4
290.8	1502.2	25.4	1	13.3	2.93
290.8	1493	25.4	2.6	44	6.7

We later fabricated rings with longer side tapers. We increased the taper length from 750μm to 5000μm and set the radius to 445μm. As expected, the amount of coupling increased to 66% for the same taper width and thickness values. The new ring has 22.796mm of circumference that corresponds to 5.45GHz of FSR. Due to more waveguide length, it also experiences more loss 5.9dB (Fig. 4.13).
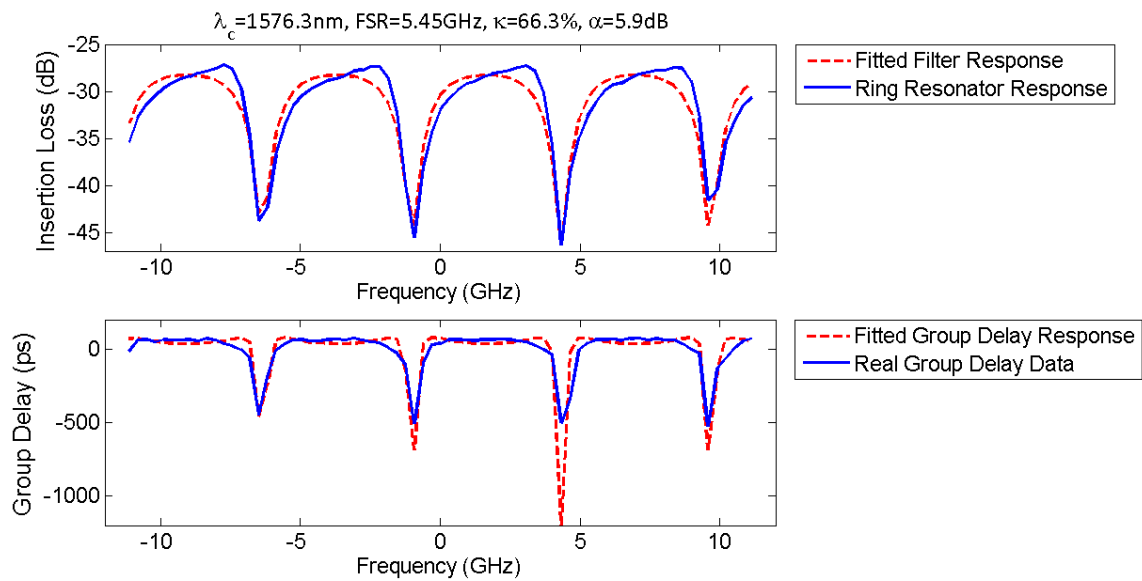
Figure 4.13. Insertion loss and group delay information of 22.796mm As_2S_3 ring on Ti:LiNbO$_3$.

4.2.2 Rings with Taper in the Middle

In the second ring resonator design, the As_2S_3 taper sits on top of the Ti:LiNbO$_3$ waveguide and the taper starts in the middle rather than to the side of the diffused waveguide (Fig. 4.14a). The complete ring structure also has underlying Ti diffused layer to avoid the post diffusion height (Fig. 4.14b).
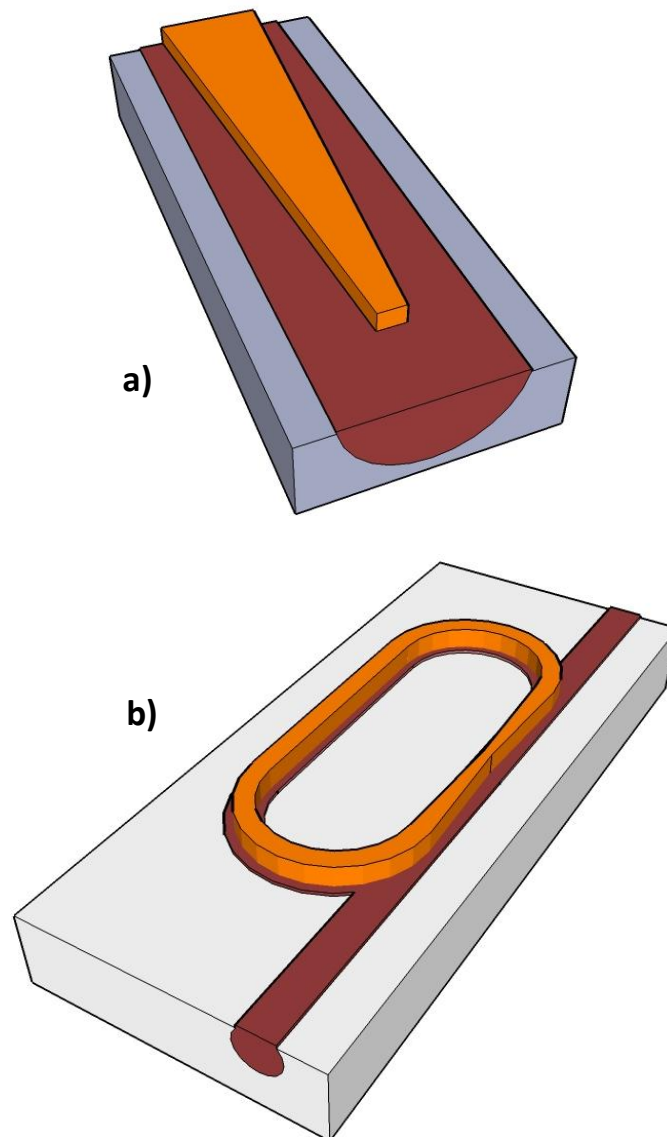
Figure 4.14. a) Taper starting from the middle; b) Race track As_2S_3-on-Ti:LiNbO$_3$ ring structure.

The main disadvantage of As_2S_3 waveguide rings sitting on top of the diffused waveguides is the loss induced by the rough surface underneath. We have captured the surface images using a light microscope with a polarizer in dark field mode in Chapter III. Atomic-force microscopy is used in multi-tapping mode to capture the surface of

post diffusion height of a sample that looks to have a very smooth surface under light

microscope (Fig. 4.15).
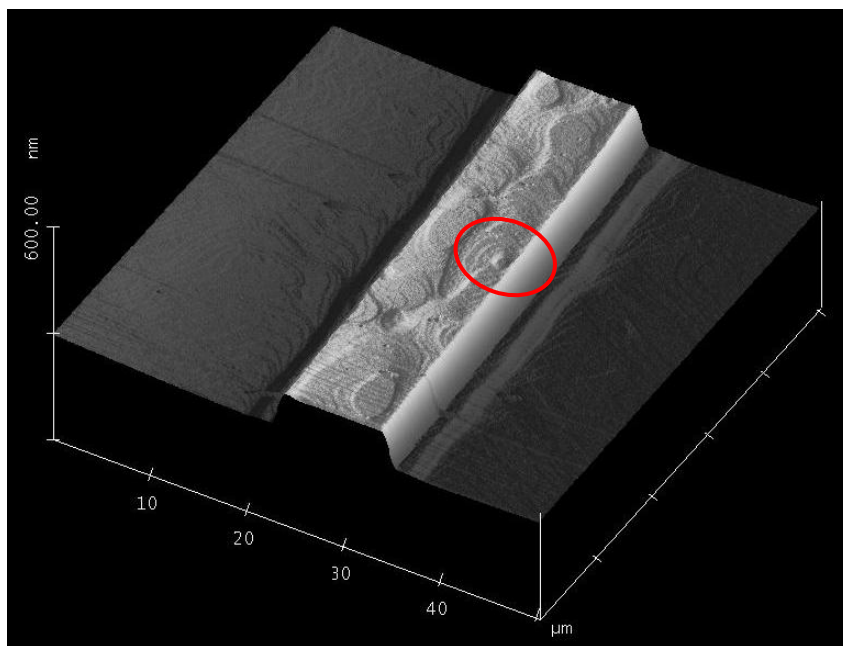
Figure 4.15. AFM picture of Ti diffused area with initial thickness of 950Å diffused wet breathing
air 9.5h at 1025°C.

Even though the surface is much smoother than before and the roughness

problem is fixed via modifying the diffusion conditions, there are still some pits that are

as much as 5nm in depth. This is captured on a line scan of the defect as circled in

Figure 4.15. Roughness underneath As_2S_3 waveguide is a big concern since waveguides

with low aspect ratio is more affected by the discontinuities at the top and the bottom

surfaces [65]. Especially TM polarizations are prone to these fluctuations on the

Ti:LiNbO$_3$ surface. There may also be random variations occurring on diffused surfaces

that could be due to imperfections on deposited titanium metal. These can be eliminated by thorough cleaning of the deposited surface.

We have used 2D finite-difference method (FDM) vectorial solver to solve TM modal effective indices (n_{eff}) of As_2S_3-on-Ti:LiNbO$_3$ waveguides as a function of width and height of the As_2S_3 overlay (Fig. 4.16a). Vectorial solvers are more accurate to solve high index contrast structures. The wavelength chosen from C-band is 1550nm and is suitable for WDM applications. The effective index of diffused waveguide mode is also plotted to give an idea about the coupling between the two waveguides and it is very close to the substrate index of 2.2112 derived from Sellmeier dispersion formula [81]. As the height increases, the effective index increases and the starting point for the curves shift to lower waveguide widths. Power confinement also increases to a stunning 51% value for 0.53µm width (Fig. 4.16b). This implies a key observation about the coupling efficiency: for thicker films, it is necessary to fabricate smaller taper start width in order to couple optical power into the As_2S_3 overlay and achieve smaller bend radii.
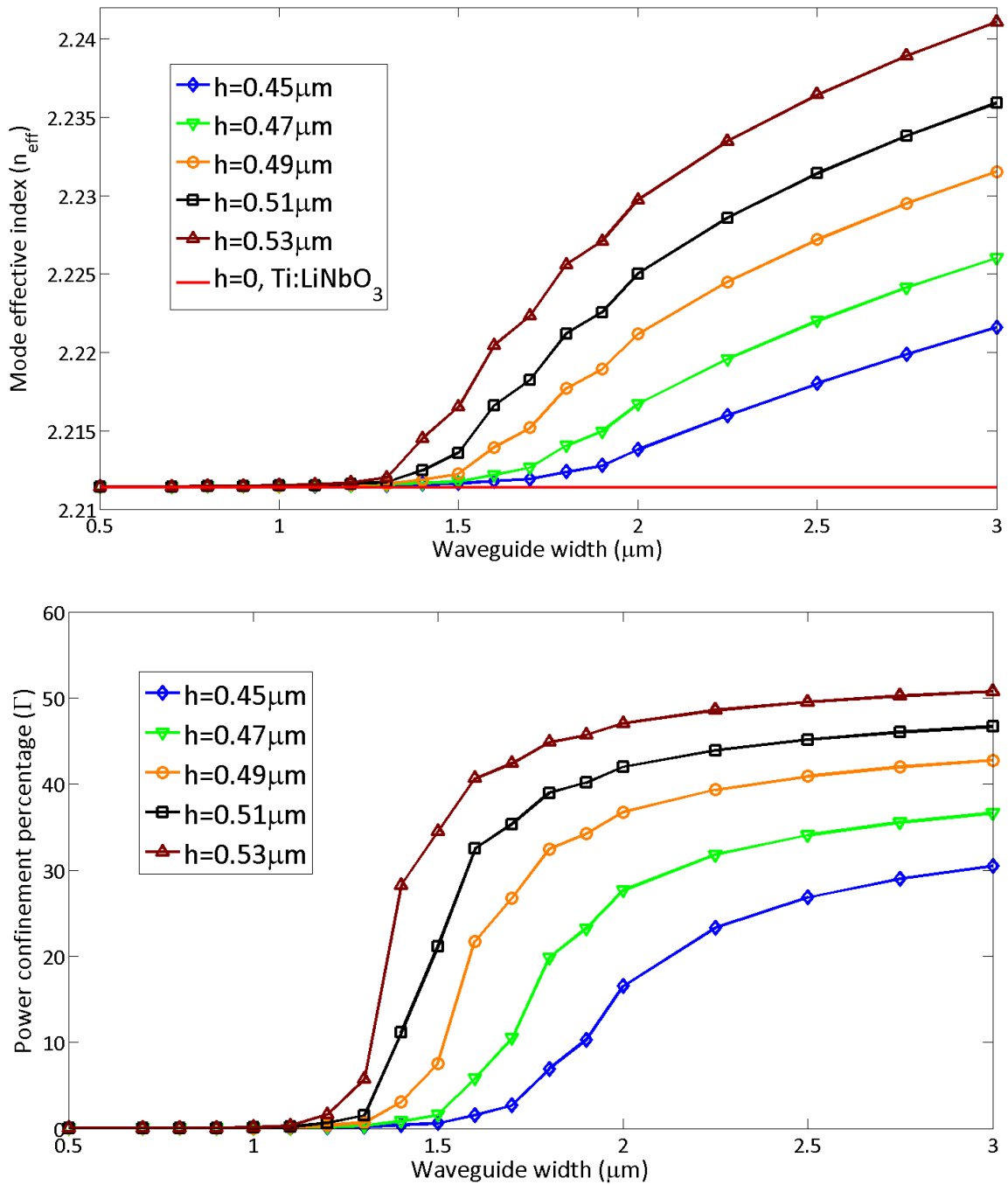
Figure 4.16. a) 2D simulations of modal effective indices from 0.5µm to 3µm; b) Power confinement in As_2S_3 for several thicknesses.

We then have simulated propagation through a taper length of 1mm (Fig. 4.17a), as the simulation software manual suggests using adiabatic tapers [82] for more accuracy and 1mm gives 0.057° of tapering angle. For this taper length, 65.4% percent of the input power is coupled up to As_2S_3 overlay and 34% stayed in the diffused region. The rest of the power coupled to radiation modes and did not survive the taper. The optical power seems to make a jump to the overlay around 400-425μm into the taper and this corresponds to an As_2S_3 width of 1.8-1.9μm. The exact width can be found by simulating Ti:LiNbO$_3$ waveguide by itself (or zero As_2S_3 width), and As_2S_3 waveguide without any diffused region underneath. As_2S_3 waveguide without diffused region is smaller than As_2S_3-on-Ti:LiNbO$_3$ and the effective indices will intersect (Fig. 4.17b). The instantaneous coupling can be justified by plotting mode effective index in the region where the taper starts (Fig. 4.17c). The n_{eff} follows a cubic curve rather than a linear one.
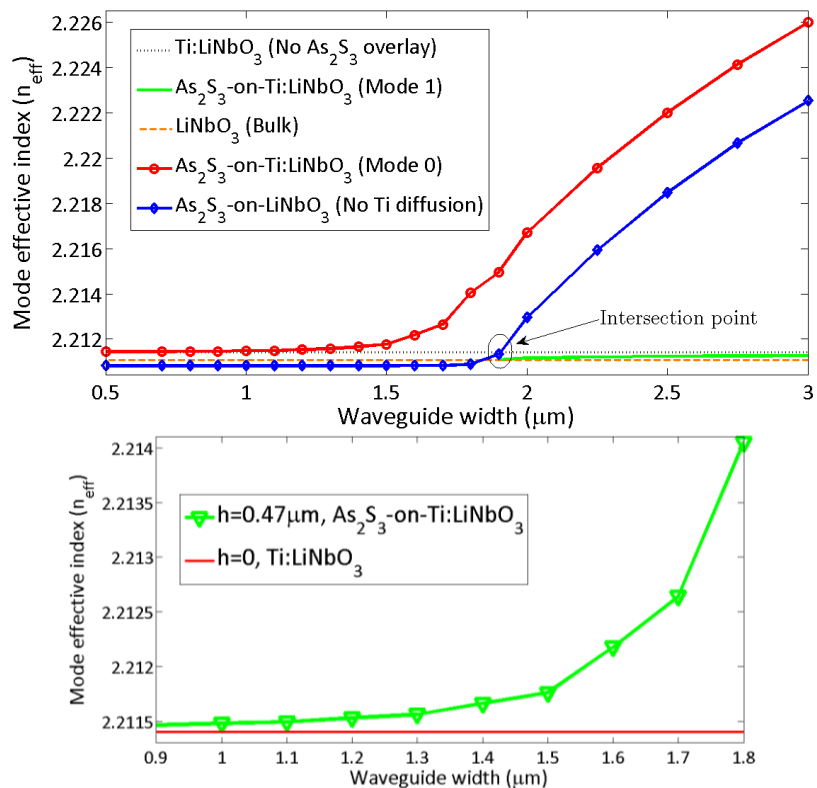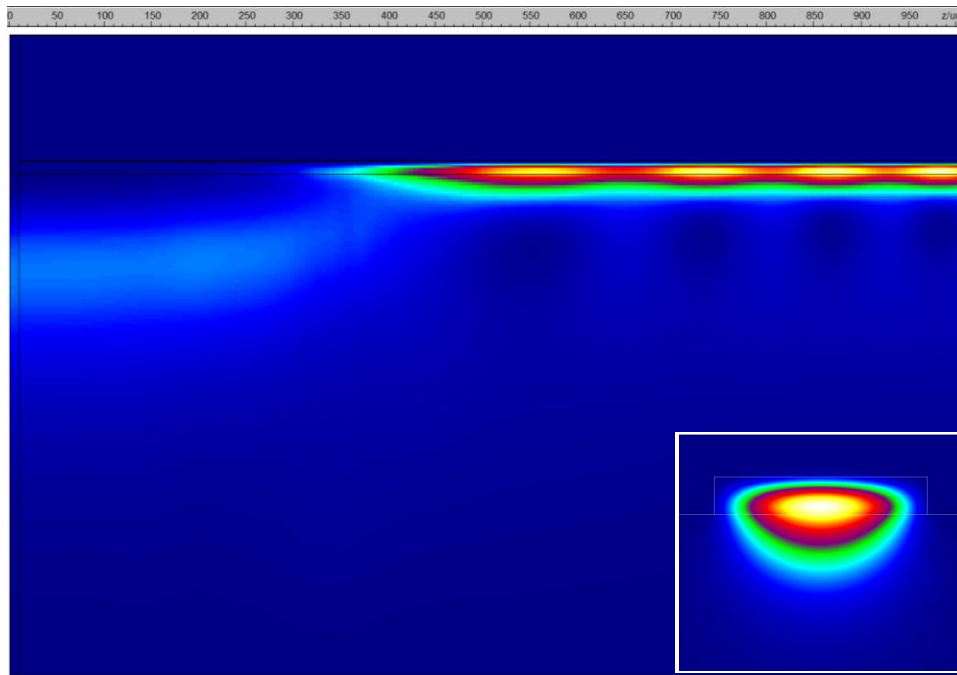
Figure 4.17. a) Side view of propagation of optical power through a of As_2S_3-on-Ti:$LiNbO_3$ taper and 2D intensity profile of As_2S_3 at the end of the taper; b) Effective indices of individual waveguides, As_2S_3 without Ti:$LiNbO_3$ and Ti:$LiNbO_3$ without As_2S_3; c) Close-up to effective index of As_2S_3-on-Ti:$LiNbO_3$ with 0.47μm.

As soon as the taper starts at 1µm, the As_2S_3-on-Ti:LiNbO$_3$ waveguide supports only 1 mode: 0th order mode confined in As_2S_3 and in Ti:LiNbO$_3$ at the same time. After around 450µm, where the overlay waveguide width is ~1.9µm, the whole structure starts supporting 2 orthogonal modes: 0th order mode confined in As_2S_3 and 1st order mode confined mostly in Ti:LiNbO$_3$ and partly in As_2S_3. The 2D intensity and vertical electric field profiles of a 2µm wide waveguides are plotted for even and odd modes (Fig. 4.18a-b). These 2 modes are also known as supermodes of the As_2S_3-on-Ti:LiNbO$_3$ waveguide structure and are orthogonal to each other [21]. The 1st order mode is actually very close to cut-off condition due to its effective index being very close to bulk refractive index. This mode is indeed a leaky but a propagating mode, and could be a source of loss if we were tapering down. Since we are slowly tapering up to a wider width structure, this mode will not generate any radiation loss and couple to diffused waveguide mode after the taper. To take the analysis further we looked at modes of 2µm wide As_2S_3 waveguide for several thicknesses (Fig. 4.18c). Although the leaky behavior is highest for 0.45µm thickness, it stays on for 0.47, 0.49, 0.51, 0.53µm thicknesses with higher effective index values. Taper with 0.45µm thickness does not experience any mode beating along its length.

We can analyze the whole taper structure in 2 steps by dividing the taper structure into 2 regions. Region 1 (1-1.9µm) only supports 1 mode and is the adiabatic mode size transforming region. Region 2 (1.9-3µm) supports 2 modes and can simply be analyzed using supermode approach.
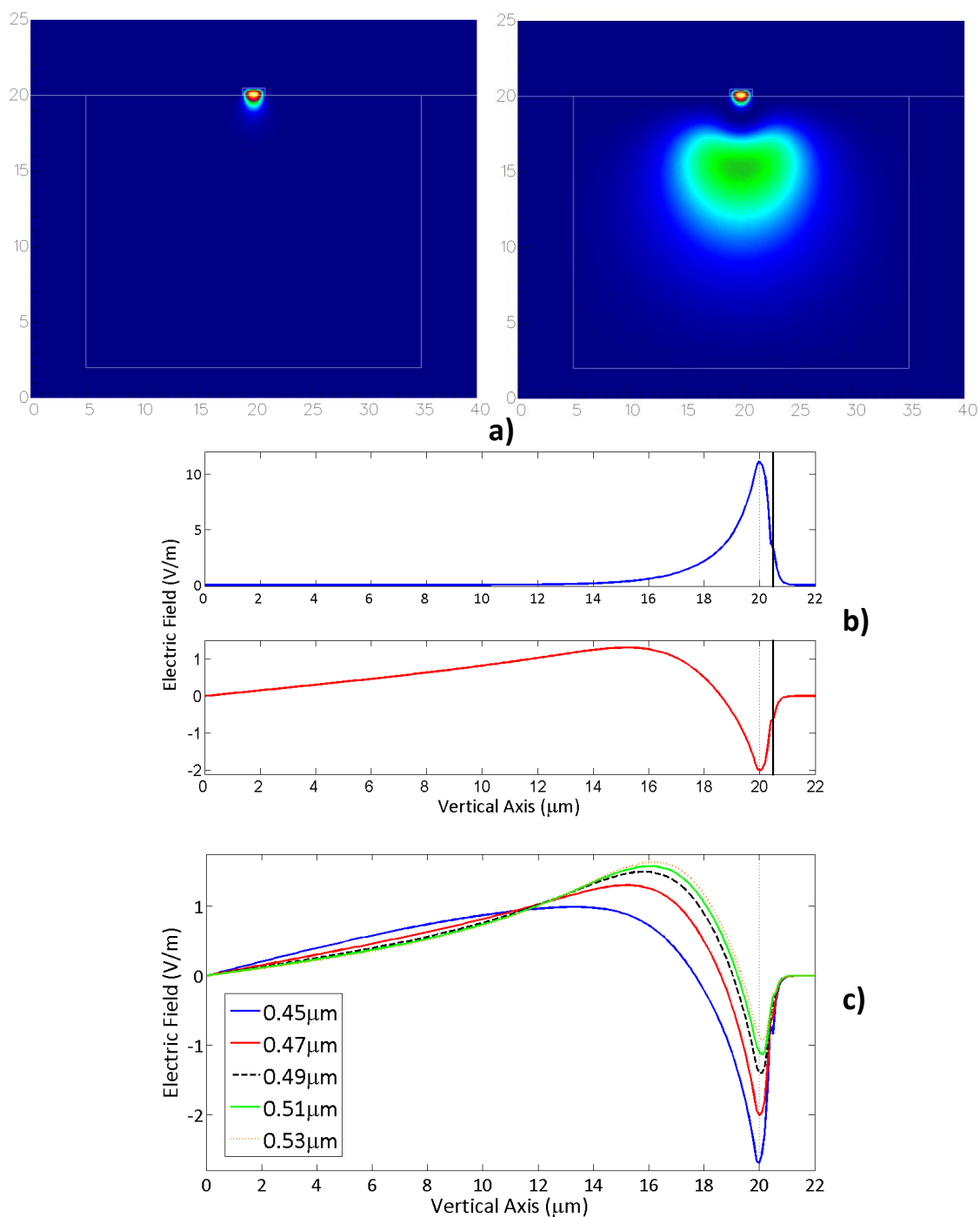
Figure 4.18. Electric field profiles of As$_2$S$_3$-on-Ti:LiNbO$_3$ waveguide; a) 2D intensity profiles with 2x0.47μm dimensions; b) Vertical electric field profile with 2x0.47μm dimensions; c) Vertical electric field profile with for several thicknesses and 2μm width.

The concept of supermodes gives a good explanation to the mode-beating phenomenon in Figure 4.18a-b [83]. It occurs owing to the effective index difference (Δn_{eff}) between the two supported mode, which is ~0.015±0.0025 or ~0.5±0.1%, and their co-propagating nature. Perturbation caused by the taper increases the effective index gap and the mode beating diminishes by the end. A vertical coupling structure using tapers is also investigated elsewhere and the same mode beating between the lower and the upper waveguides is observed [84]. In order to further minimize the supermode behavior of As_2S_3-on-Ti:$LiNbO_3$ waveguides, it is necessary to bend the waveguide away from straight diffused waveguide. Since Ti:$LiNbO_3$ waveguides cannot support bent modes of low radius of curvature, mode beating should not be expected around the bend.

The adiabatic mode transformer region slowly perturbs the diffused mode and increases the propagation constant. The mode effective area (A_{eff}) reduces 20 times (Ti:$LiNbO_3$ with respect to As_2S_3) and the peak intensity increases through this region. We can plot the mode evolution from 1μm to 1.8μm along the vertical axis (Fig. 4.19).
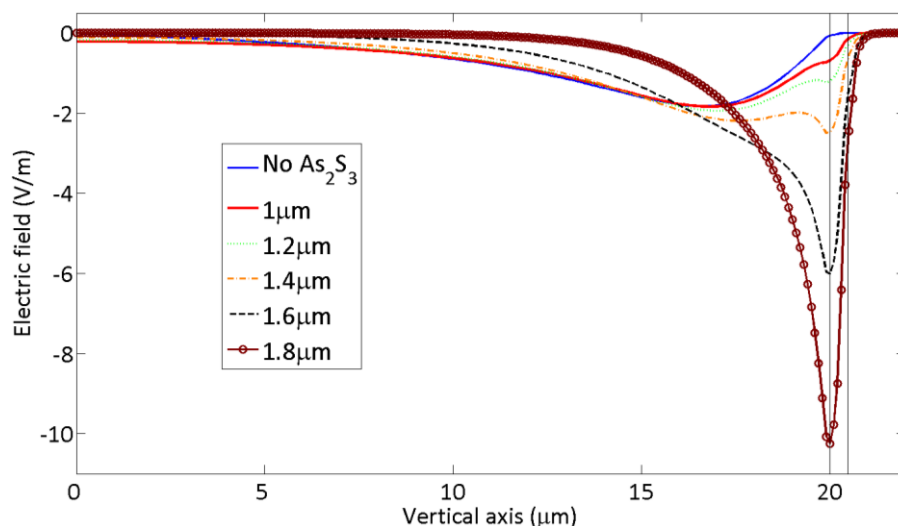
Figure 4.19. Electric field profiles of As_2S_3-on-Ti:$LiNbO_3$ waveguide tapering up from 1 to 1.9µm with 0.47µm height.

We have fabricated As_2S_3 ring resonator as shown in figure 4.13 by optimizing the surface of the diffused region. The final ring has 750µm long tapers and 475µm radius. Titanium diffused waveguides fabrication started with the initial 850Å strip thickness and 9 hours of diffusion in a wet breathing air atmosphere (Breathing air goes through heated water at 70°C) at 1025°C. After surface inspection, the ends are polished to optical quality. 475±5nm of As_2S_3 is deposited on the optical chip with a subsequent thin layer (50±5nm) of titanium evaporation. Instead of SiO_2+Ti and PR, we used Ti as the etch mask and the protective layer as described in Chapter III. Moreover, extended photoresist bake time (30min at 135°C) is used so that PR reflows and the sidewalls smoothen out. Titanium metal is etched with RIE and PR is removed with a prolonged O_2 plasma process. As_2S_3 waveguides are formed using Ti etch mask before

all of the metal is consumed. Additional HF dip removed the remaining Ti from the top of As_2S_3 waveguide.

The same testing procedure that was used for rings in section 4.2.1 is employed. The coupling percentage and the roundtrip loss are derived for a ring with ~7dB extinction ratio. 36% coupling with a 4.8dB roundtrip loss is obtained (Fig. 4.20).
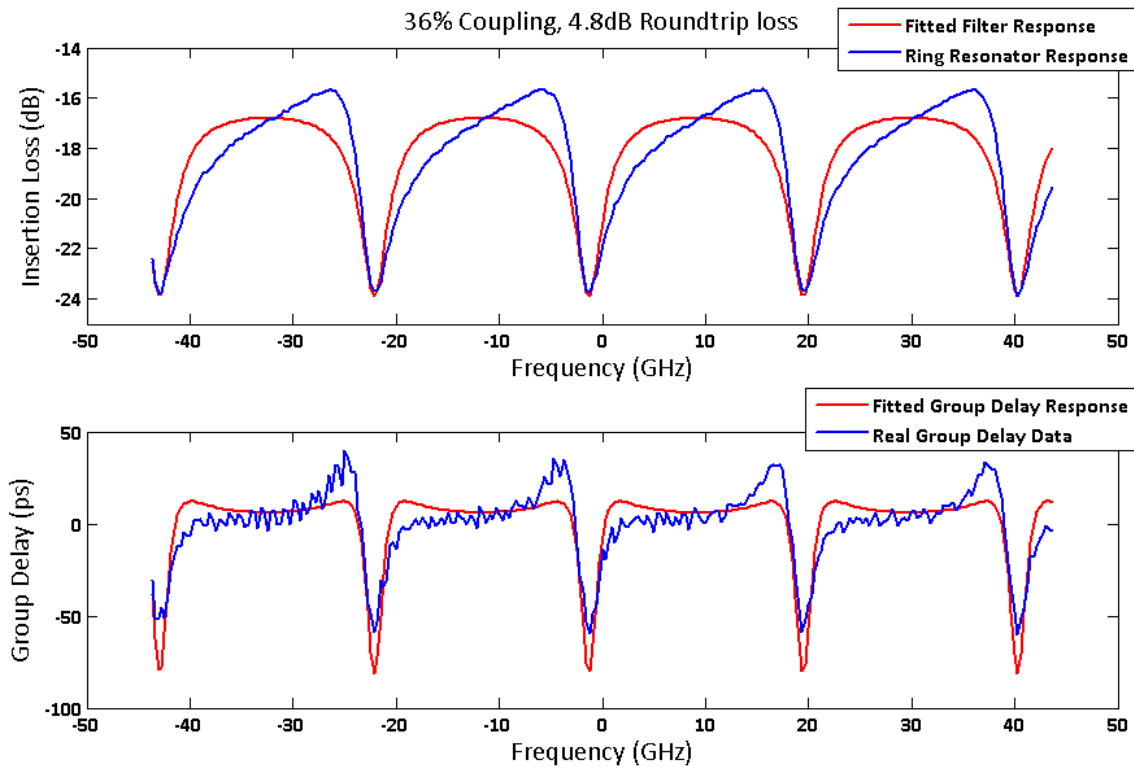
Figure 4.20. Ring resonance and its fitting at 1542nm center wavelength spanning 4 FSRs.

The ring with the taper in the middle has an increased coupling (κ) due to taper being close to the center of $Ti:LiNbO_3$ waveguide. The perturbation of the high index overlay is highest at the center of the diffused Ti strip since the modal intensity of the

diffused waveguide is also the highest in the middle. This can clearly be seen Figure 4.2c. We can argue that the coupling increase from 10.6% to 36% is a direct result of using a taper close to the center of the diffused region since all the taper dimensions are kept same.

In order to minimize the loss related to surface roughness, we designed an experiment where a buffer layer is introduced between Ti:LiNbO$_3$ and As$_2$S$_3$ waveguides. The buffer layer is selected as SiO$_2$ due to its availability and lower refractive index. In this taper design, a very thin layer of oxide (SiO$_2$, n=1.44) is used as a buffer layer in between the two similar refractive index cores. Since there is an intermediate layer, the overlay waveguide is not in direct contact with the diffused waveguide mode and the index contrast of As$_2$S$_3$ core with respect to surrounding (SiO$_2$) increases to 40%. First we have used a very thin layer of SiO$_2$ (10nm) in between the two higher index regions and simulated the supported modes. With 0.47μm height, the effective index of the fundamental mode becomes 2.213 and the power confinement decreases to 8%, which is not enough for a small bent structure. The same confinement factor (35%) is obtained when the waveguide height is increased to 0.51μm. We plotted the effective indices for heights of 0.51, 0.53, 0.55, and 0.57μm (Fig. 4.21a) and confinement percentages (Fig. 4.21b). It can be seen that, any thickness from 0.51 to 0.53 is suitable for taper structure due to the starting point of the n$_{eff}$ curves. Moreover, the confinement factor increases to ~56% for the thickness of 0.55μm.

Even though 10nm makes a huge improvement in terms of confinement, there is the possibility of mode leakage as a result of such a thin layer. Silicon-on-insulator waveguides need to have 2-3μm of oxide underneath in order to prevent substrate mode leakage. It is also hard to control such a thickness using a deposition system in real world. Hence we aimed for a middle layer thickness that is more achievable in reality, 100nm.
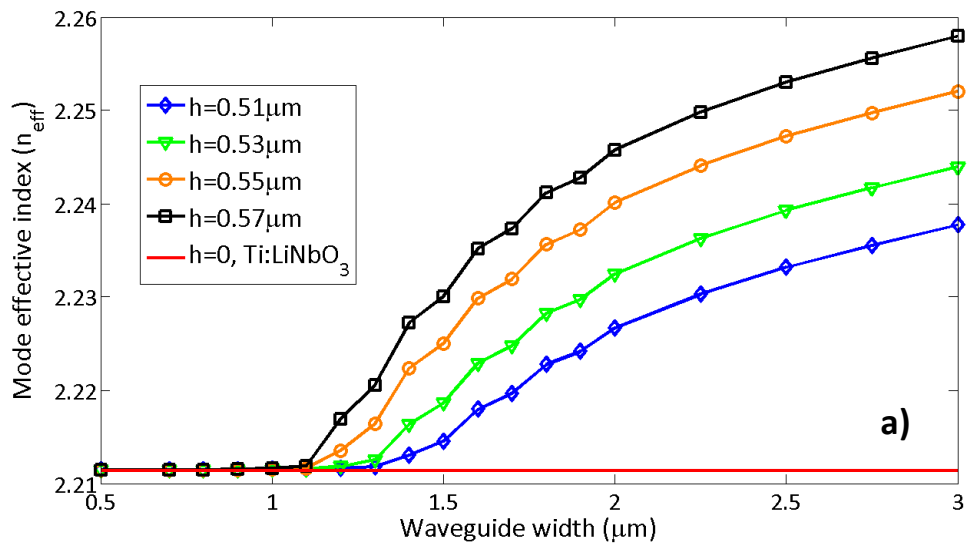
Figure 4.21. Modal effective indices and confinement factors as a function of waveguide dimensions are intermediate layer thickness; a-b) For 10nm SiO$_2$; c-d) For 100nm SiO$_2$.
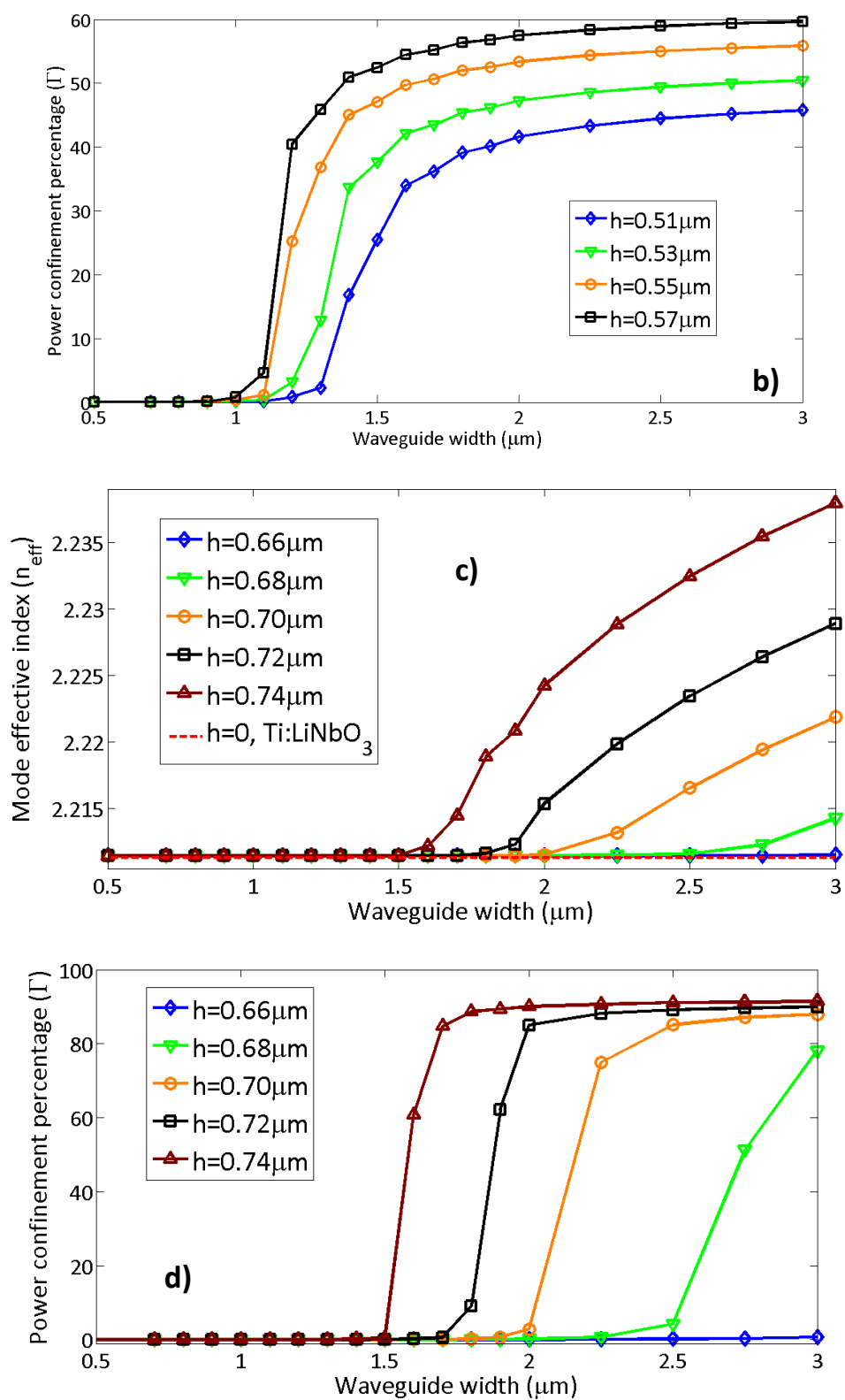
Figure 4.21. Continued.

At this middle layer thickness, the As_2S_3 waveguide has better confinement at the bottom boundary. Again, we plot the effective indices for several waveguide dimensions to find a suitable match for the waveguide height (Fig. 4.21c). At 0.66μm thickness, the power confinement is only 5% and it goes up to 78% at 0.68μm and 84% at 0.7μm (Fig. 4.21d).
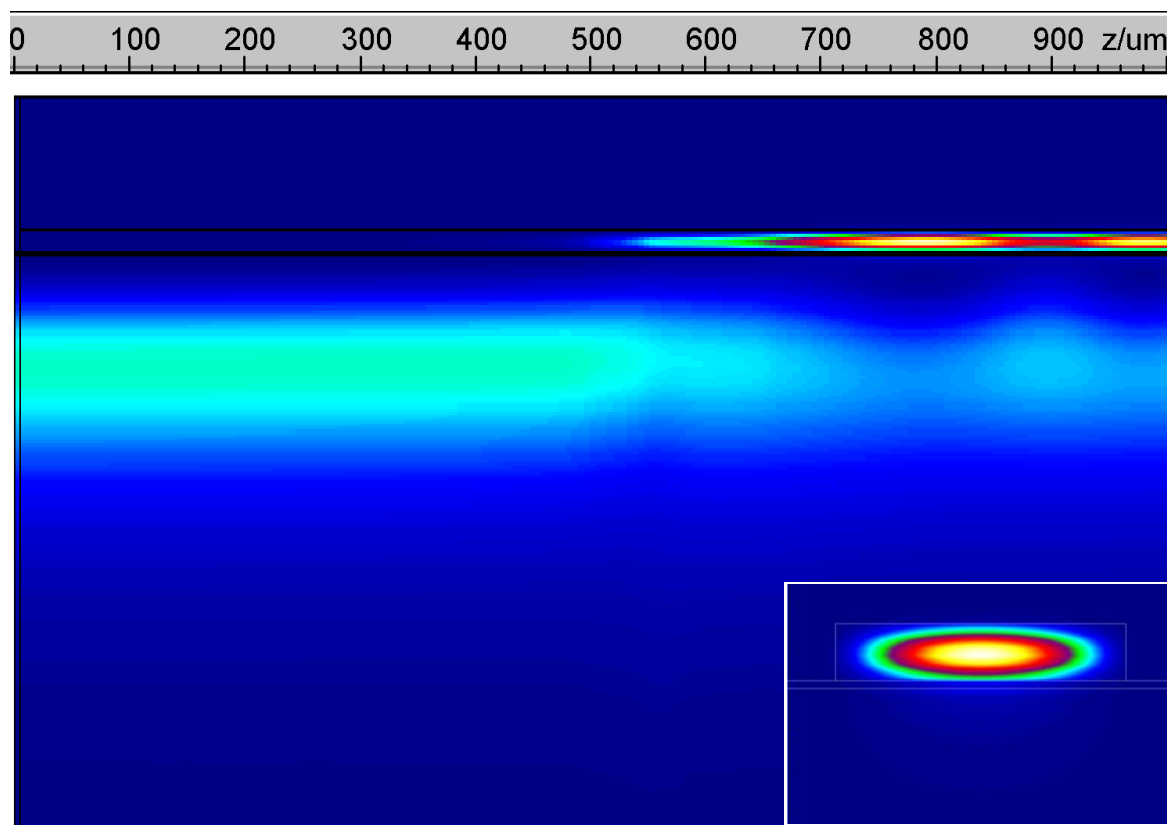
Figure 4.22. Side view of propagation of optical power through a of As_2S_3-on-Ti:LiNbO$_3$ taper with 100nm SiO$_2$ in between; in inset 2D modal intensity of 0th order mode captured at the end of the taper.

We have once more simulated the taper structure with an intermediate layer of 100nm (Fig. 4.22). The power transfer is a little later (around 500-550μm) and 22.2% of

the input power coupled up to the As_2S_3 overlay waveguide. The 2D intensity profile is captured as inset of 4.22 and the mode looks superbly confined in the lateral direction compared to figure 4.17a. The height can be varied to obtain more or less power coupling. The same more beating phenomenon is observed in this case as a result of 2 modes propagating simultaneously. Surprisingly, the modes are not leaky and electric fields go to zero at the bottom boundary. To confirm the lateral confinement, the electric fields are plotted for 3µm width and several thickness values (Fig. 4.23).
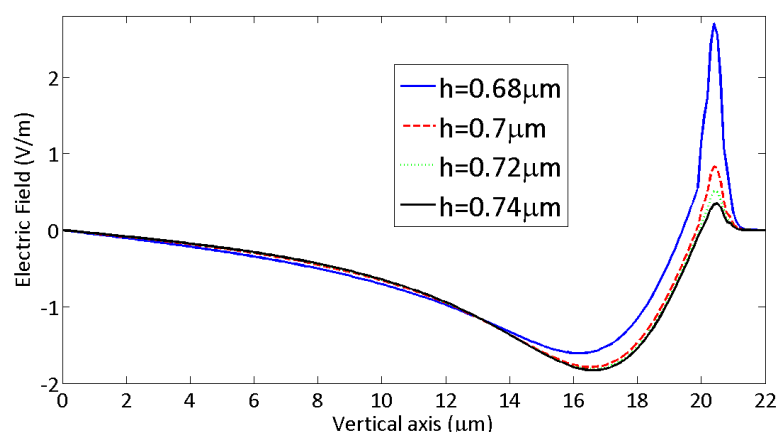
Figure 4.23. Electric field profiles of As_2S_3-on-Ti:$LiNbO_3$ waveguides with 0.68-0.7-0.72-0.74µm height and 3µm width, and additional 100nm SiO_2 as intermediate layer.

We have fabricated rings with middle taper with an addition of SiO_2 layer in between. The buffer layer thickness is chosen as 100nm and the As_2S_3 waveguide height as 7200Å. The taper length is 2.5mm and the circumference is 12.98mm that corresponds to 9.7GHZ FSR. The coupling (89.6%) to higher index As_2S_3 is confirmed although the roundtrip loss (8.27dB) is not improved much (Fig. 4.24).
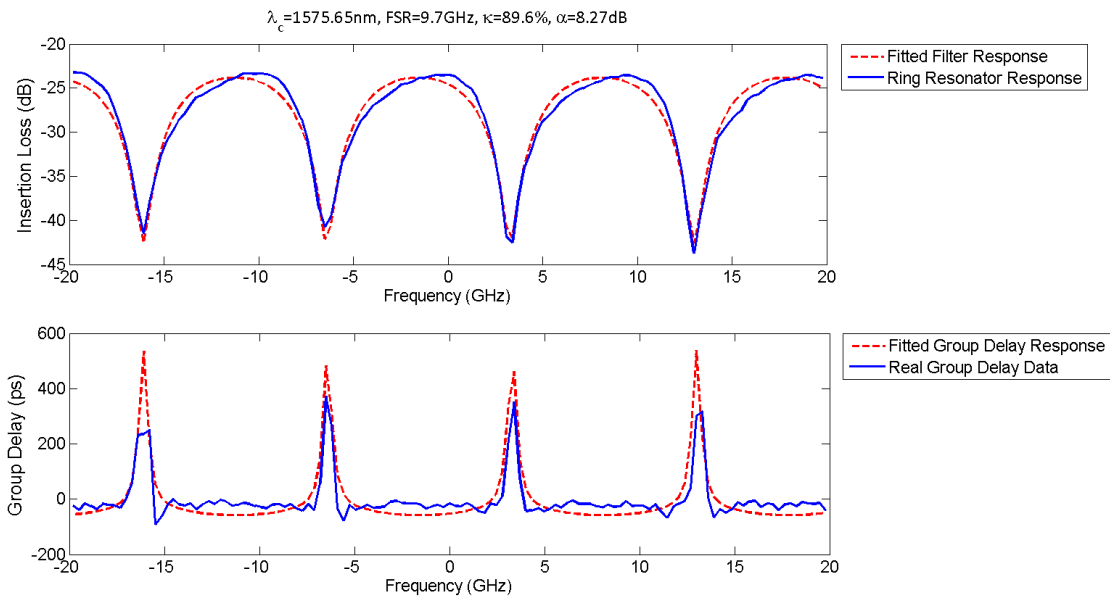
Figure 4.24. Resonance of a ring with buffer layer and its fitting at 1575.65nm center wavelength spanning 4 FSRs.

CHAPTER V

CONCLUSION

In order to compensate for the intrinsic absences of small size and high index contrast of titanium-diffused lithium-niobate waveguides, a chalcogenide glass material (As_2S_3) is vertically integrated on $LiNbO_3$ substrate to form optically guiding regions for main building blocks of integrated optical filters. The titanium metal diffusion creates a very small refractive index increase to a relatively large region of $LiNbO_3$ crystal. This region is very compatible in size to single mode optical fibers and the power coupling loss is less than 1dB for most waveguides. In addition to very small coupling loss, the optical path can be electro-optically tuned using electrodes to create small changes in refractive index and change the optical phase. Phase and amplitude modulators are two basic optical filters than can be realized using $Ti:LiNbO_3$ waveguides.

We have incorporated As_2S_3 with $Ti:LiNbO_3$ waveguides and used the prior's small size and high index contrast to our advantage to add a very key functionality to $LiNbO_3$ waveguide technology. Feedback filters of very small bending radii can now be realized on $LiNbO_3$ that cannot be achieved using regular titanium diffusion process. The incoming light is coupled up to As_2S_3 waveguide using a 2D taper structure that minimally perturbs the waveguide mode inside the diffused waveguide. The taper's dimensions (the As_2S_3 layer thickness, initial and the final width, and the taper length) determine the amount of coupling into the As_2S_3 waveguide.

Our first experiments to test the taper structure were on S-shaped bends where the diffused waveguide mode is transferred to the parallel diffused waveguide using an As_2S_3 S-bend [67]. Mode is coupled up and down to the s-bend using 2mm long taper structures. The thickness of the As_2S_3 layer is kept at 0.4µm to reduce the mode size and to confine some of the power in the overlay waveguide. The power extinction ratio between the through and cross ports of the S-bend is around ~23dB for 1.27° angle. This results proves the complete power transfer to the parallel diffused waveguide using the As_2S_3 overlay.

We later pursued fabrication of As_2S_3 ring resonators on Ti:$LiNbO_3$ waveguides to realize a key feature for many optical filters. The taper design is changed from middle taper to side taper design and the tapers are placed right next to the diffused waveguide to avoid the post-diffusion height created by the titanium diffusion process. The taper length is kept at 750µm and the radius at 290.8µm while the thickness is increased to 0.47µm. The mode is more confined in As_2S_3 waveguide (36%) and the whole As_2S_3-on-Ti:$LiNbO_3$ waveguide supports two modes. The co-propagating nature of overlay and diffused waveguide modes are observed along the taper using finite-difference method simulations. The ring resonator is in allpass configuration and the coupling percentage to As_2S_3 is 10.6% while the roundtrip loss is calculated as 2.08dB [71]. We have fitted real amplitude and group delay information out of Optical Vector Analyzer (OVA) to the estimated transfer function to extract coupling and roundtrip loss information.

In addition to the results from the two devices that are tested, the entire fabrication process on As_2S_3-on-Ti:LiNbO$_3$ is developed. Due to solubility of As_2S_3 in developer solution, we introduced a protective layer on chalcogenide glass to carry out photolithography on. We later established both lithography and reactive-ion etching recipes to obtain sidewall smoothness and prevent a positively angled frame. We improved the grainy looking surface on Ti-diffused areas due to Ti_xO_y formation during annealing process. The polishing of Ti:LiNbO$_3$ waveguides are enhanced to a much faster and better way to speed up the whole process flow. As_2S_3 deposition process is also implemented and modified to obtain consistent results.

REFERENCES

[1]   E. Consultants, "Optical modulators global market forecast & analysis," 2008.

[2]   E. A. J. Marcatili, "Bends in optical dielectric guides," *The Bell System Technical Journal,* vol. 48, pp. 2103-2132, 1969.

[3]   M. Heiblum and J. Harris, "Analysis of curved optical waveguides by conformal transformation," *IEEE Journal of Quantum Electronics,* vol. 11, pp. 75-83, 1975.

[4]   T. Tsuchizawa, K. Yamada, H. Fukuda, T. Watanabe, T. Jun-ichi*, et al.*, "Microphotonics devices based on silicon microfabrication technology," *Selected Topics in IEEE Journal of Quantum Electronics,* vol. 11, pp. 232-240, 2005.

[5]   G. Bourdon, G. Alibert, A. Beguin, B. Bellman, and E. Guiot, "Ultralow loss ring resonators using 3.5% index-contrast Ge-doped silica waveguides," *IEEE Photonics Technology Letters ,* vol. 15, pp. 709-711, 2003.

[6]   Z. Shengmei, C. Hui, and A. W. Poon, "Microring-resonator cross-connect filters in silicon nitride: rib waveguide dimensions dependence," *Selected Topics in IEEE Journal of Quantum Electronics,* vol. 12, pp. 1380-1387, 2006.

[7]   M. K. Chin, C. Youtsey, W. Zhao, T. Pierson, Z. Ren*, et al.*, "GaAs microcavity channel-dropping filter based on a race-track resonator," *IEEE Photonics Technology Letters,* vol. 11, pp. 1620-1622, 1999.

[8]   P. Suchoski and R. Ramaswamy, "Minimum-mode-size low-loss Ti: $LiNbO_3$ channel waveguides for efficient modulator operation at 1.3μm"*, IEEE Journal of Quantum Electronics,* vol. 23, pp. 1673-1679, 1987.

[9]   J. K. S. Poon, L. Zhu, G. A. DeRose, and A. Yariv, "Polymer microring coupled-resonator optical waveguides," *J. Lightwave Technol.,* vol. 24, p. 1843, 2006.

[10]   H. S. C. Vannahme, S. Reza, R. Ricken, V. Quiring, and W. Sohler, "Integrated optical Ti:$LiNbO_3$ ring resonator for rotation rate sensing" in *Proc. European Conference on Integrated Optics, Copenhagen, Denmark,* 2007.

[11]   J. L. Jackel, C. E. Rice, and J. J. Veselka, "Proton-exchange for high-index waveguides in $LiNbO_3$," *Applied Physics Letters,* vol. 41, pp. 607-608, 1982.

[12]   M. Majd, B. Schuppert, and K. Petermann, "90° S-bends in Ti:LiNbO$_3$ waveguides with low losses," *IEEE Photonics Technology Letters,* vol. 5, pp. 806-808, 1993.

[13]   T.-J. Wang, C.-H. Chu, and C.-Y. Lin, "Electro-optically tunable microring resonators on lithium niobate," *Opt. Lett.,* vol. 32, pp. 2777-2779, 2007.

[14]   A. Guarino, G. Poberaj, D. Rezzonico, R. Degl'Innocenti, and P. Gunter, "Electro-optically tunable microring resonators in lithium niobate," *Nat Photon,* vol. 1, pp. 407-410, 2007.

[15]   O. Mikami, J. Noda, S. Zembutsu, and S. Fukunishi, "Phase tuning in optical directional coupler by photostructural effect of chalcogenide glass film," *Applied Physics Letters,* vol. 31, pp. 376-378, 1977.

[16]   S. Zembutsu, J. Noda, and H. Iwasaki, "Light deflector using a chalcogenide amorphous loaded LiNbO$_3$ waveguide," *Appl. Opt.,* vol. 19, pp. 937-943, 1980.

[17]   J. A. Stratton, *Electromagnetic theory*. New York: McGraw-Hill book company, inc., 1941.

[18]   *FimmProp* from Photon Design *Inc*. http://www.photond.com, 2009.

[19]   W. S. Rodney, I. H. Malitson, and T. A. King, "Refractive index of arsenic trisulfide," *J. Opt. Soc. Am.,* vol. 48, pp. 633-635, 1958.

[20]   M. Fukuma, J. Noda, and H. Iwasaki, "Optical properties in titanium-diffused LiNbO$_3$ strip waveguides," *Journal of Applied Physics,* vol. 49, pp. 3693-3698, 1978.

[21]   J.-M. Liu, *Photonic devices*. New York: Cambridge, 2004.

[22]   A. S. Sudbo, "Film mode matching: a versatile numerical method for vector mode field calculations in dielectric waveguides," *Pure and Applied Optics: Journal of the European Optical Society Part A,* p. 211, 1993.

[23]   C. K. Madsen and J. H. Zhao, *Optical filter design and analysis: a signal processing approach*. New York: John Wiley & Sons, 1999.

[24]   D. Lide, *CRC Handbook of chemistry and physics, 88th Edition.Boca Raton, FL*: CRC Press/Taylor and Francis, 2007.

[25]   G. Griffiths and R. Esdaile, "Analysis of titanium diffused planar optical waveguides in lithium niobate," *IEEE Journal of Quantum Electronics,* vol. 20, pp. 149-159, 1984.

[26]   W. K. Burns, P. H. Klein, E. J. West, and L. E. Plew, "Ti diffusion in Ti : $LiNbO_3$ planar and channel optical waveguides," *Journal of Applied Physics,* vol. 50, pp. 6175-6182, 1979.

[27]   S. Korotky, W. Minford, L. Buhl, M. Divino, and R. Alferness, "Mode size and method for estimating the propagation constant of single-mode $Ti:LiNbO_3$ strip waveguides," *IEEE Journal of Quantum Electronics,* vol. 18, pp. 1796-1801, 1982.

[28]   R. C. Alferness and L. L. Buhl, "Electro-optic waveguide TE to TM mode converter with low drive voltage," *Opt. Lett.,* vol. 5, p. 473, 1980.

[29]   J. L. Jackel, V. Ramaswamy, and S. P. Lyman, "Elimination of out-diffused surface guiding in titanium-diffused $LiNbO_3$," *Applied Physics Letters,* vol. 38, pp. 509-511, 1981.

[30]   O. Eknoyan, A. S. Greenblatt, W. K. Burns, and C. H. Bulmer, "Characterization of $Ti:LiNbO_3$ deep waveguides diffused in dry and wet oxygen ambient," *Appl. Opt.,* vol. 25, pp. 737-739, 1986.

[31]   T. Nozawa, H. Miyazawa, and S. Miyazawa, "Water vapor effects on titanium diffusion into $LiNbO_3$ substrates," *Japanese Journal of Applied Physics,* vol. 29, p. 2180, 1990.

[32]   E. Zolotoyabko, Y. Avrahami, W. Sauer, T. H. Metzger, and J. Peisl, "High-temperature phase transformation in Ti-diffused waveguide layers of $LiNbO_3$," *Applied Physics Letters,* vol. 73, pp. 1352-1354, 1998.

[33]   C. E. Rice and R. J. Holmes, "A new rutile structure solid-solution phase in the $LiNb_3O_8$-TiO_2 system, and its role in Ti diffusion into $LiNbO_3$," *Journal of Applied Physics,* vol. 60, pp. 3836-3839, 1986.

[34]   V. Sivan, A. Mitchell, L. Bui, A. Holland, S. Bhargava*, et al.*, "Etching of lithium niobate using standard Ti indiffusion technique," *Applied Physics Letters,* vol. 91, pp. 231921-3, 2007.

[35]   R. Dahan, N. Croitoru, and S. Ruschin, "Studies on the relation between the diffusion process and optical properties in Ti-diffused planar optical waveguides," *Appl. Opt.,* vol. 30, pp. 4396-4401, 1991.

[36]   M. D. M. Tsirlin, "Some peculiarities of Ti in-diffusion in lithium niobate," *Crystal Research and Technology,* vol. 42, pp. 678-683, 2007.

[37]   C. Canali, C. De Bernardi, M. De Sario, A. Loffredo, G. Mazzi*, et al.*, "Effects of water vapor on refractive index profiles in Ti:LiNbO$_3$ planar waveguides," *Journal of Lightwave Technology,* vol. 4, pp. 951-955, 1986.

[38]   R. J. Holmes and D. M. Smyth, "Titanium diffusion into LiNbO$_3$ as a function of stoichiometry," *Journal of Applied Physics,* vol. 55, pp. 3531-3535, 1984.

[39]   S. Ramachandran and S. G. Bishop, "Low loss photoinduced waveguides in rapid thermally annealed films of chalcogenide glasses," *Applied Physics Letters,* vol. 74, pp. 13-15, Jan 4 1999.

[40]   J. F. Viens, C. Meneghini, A. Villeneuve, T. V. Galstian, E. J. Knystautas*, et al.*, "Fabrication and characterization of integrated optical waveguides in sulfide chalcogenide glasses," *Journal of Lightwave Technology,* vol. 17, pp. 1184-1191, Jul 1999.

[41]   Y. L. Ruan, W. T. Li, R. Jarvis, N. Madsen, A. Rode*, et al.*, "Fabrication and characterization of low loss rib chalcogenide waveguides made by dry etching," *Optics Express,* vol. 12, pp. 5140-5145, Oct 18 2004.

[42]   N. Hô, M. C. Phillips, H. Qiao, P. J. Allen, K. Krishnaswami*, et al.*, "Single-mode low-loss chalcogenide glass waveguides for the mid-infrared," *Optics Letters,* vol. 31, pp. 1860-1862, 2006.

[43]   J. Hu, N. Carlie, L. Petit, A. Agarwal, K. Richardson*, et al.*, "Demonstration of chalcogenide glass racetrack microresonators," *Opt. Lett.,* vol. 33, pp. 761-763, 2008.

[44]   R. G. DeCorby, N. Ponnampalam, M. M. Pai, H. T. Nguyen, P. K. Dwivedi*, et al.*, "High index contrast waveguides in chalcogenide glass and polymer," *Selected Topics in IEEE Journal of Quantum Electronics,* vol. 11, pp. 539-546, 2005.

[45]   A. Zakery, Y. Ruan, A. V. Rode, M. Samoc, and B. Luther-Davies, "Low-loss waveguides in ultrafast laser-deposited As_2S_3 chalcogenide films," *J. Opt. Soc. Am. B,* vol. 20, pp. 1844-1852, 2003.

[46]   J. S. W. Ing, J. H. Neyhart, and F. Schmidlin, "Charge transport and photoconductivity in amorphous arsenic trisulfide films," *Journal of Applied Physics,* vol. 42, pp. 696-703, 1971.

[47]   S. A. Campbell, *The science and engineering of microelectronic fabrication*, 2nd ed. New York: Oxford University Press, 2001.

[48]   M. K. Bahl, R. O. Woodall, R. L. Watson, and K. J. Irgolic, "Relaxation during photoemission and LMM Auger decay in arsenic and some of its compounds," *The Journal of Chemical Physics,* vol. 64, pp. 1210-1218, 1976.

[49]   P. A. Bertrand, "XPS study of chemically etched GaAs and InP," *Journal of Vacuum Science and Technology,* vol. 18, pp. 28-33, 1981.

[50]   B. J. Lindberg, K. Hamrin, G. Johansson, U. Gelius, A. Fahlman*, et al.*, "Molecular spectroscopy by means of ESCA II. sulfur compounds. correlation of electron binding energy with structure," *Physica Scripta,* vol. 1, pp. 286-298, 1970.

[51]   J. Heo, J. S. Sanghera, and J. D. Mackenzie, "A structural investigation of As_2S_3-Tl_2S glasses by XPS," *Journal of Non-Crystalline Solids,* vol. 101, pp. 23-30, 1988.

[52]   F. L. Pedrotti, L. S. Pedrotti, and L. M. Pedrotti, *Introduction to optics*, 3rd ed. Upper Saddle River, N.J.: Pearson Prentice Hall, 2007.

[53]   G. Boudebs, S. Cherukulappurath, M. Guignard, J. Troles, F. Smektala*, et al.*, "Linear optical characterization of chalcogenide glasses," *Optics Communications,* vol. 230, pp. 331-336, 2004.

[54]   C. Duk-Yong, S. Madden, A. Rode, W. Rongping, D. Bulla*, et al.*, "Fabrication of As_2S_3 planar waveguides with very low propagation loss," presented at the Lasers and Electro-Optics Society, 2007.

[55]   Y. Ruan, M.-K. Kim, Y.-H. Lee, B. Luther-Davies, and A. Rode, "Fabrication of high-Q chalcogenide photonic crystal resonators by e-beam lithography," *Applied Physics Letters,* vol. 90, pp. 071102-3, 2007.

[56]   A. J. v. Roosmalen, J. A. G. Baggerman, and S. J. H. Brader, *Dry etching for VLSI*. New York: Plenum Press, 1991.

[57]   C. Duk-Yong, S. Madden, A. Rode, W. Rongping, A. Ankiewicz*, et al.*, "Surface roughness in plasma-Etched As_2S_3 Films: its origin and improvement," *IEEE Transactions on Nanotechnology,* vol. 7, pp. 285-290, 2008.

[58]   Y. Shani, R. Alferness, T. Koch, U. Koren, M. Oron*, et al.*, "Polarization rotation in asymmetric periodic loaded rib waveguides," *Applied Physics Letters,* vol. 59, pp. 1278-1280, 1991.

[59]   W. W. Lui, T. Hirono, K. Yokoyama, and H. Wei-Ping, "Polarization rotation in semiconductor bending waveguides: a coupled-mode theory formulation," *Journal of Lightwave Technology,* vol. 16, pp. 929-936, 1998.

[60]   B. E. Little and S. T. Chu, "Theory of polarization rotation and conversion in vertically coupled microresonators," *IEEE Photonics Technology Letters,* vol. 12, pp. 401-403, 2000.

[61]   Y. Vlasov and S. McNab, "Losses in single-mode silicon-on-insulator strip waveguides and bends," *Opt. Express,* vol. 12, pp. 1622-1631, 2004.

[62]   W. Zhao, J. W. Bae, I. Adesida, and J. H. Jang, "Effect of mask thickness on the nanoscale sidewall roughness and optical scattering losses of deep-etched InP/InGaAsP high mesa waveguides," *Journal of Vacuum Science & Technology B: Microelectronics and Nanometer Structures,* vol. 23, pp. 2041-2045, 2005.

[63]   T. Suligoj, K. L. Wang, and P. Biljanovic, "Minimization of sidewall roughness in Si pillar-like structures by photolithography optimization," in *Electrotechnical Conference, 2002. MELECON 2002. 11th Mediterranean*, 2002, pp. 458-462.

[64]   F. P. Payne and J. P. R. Lacey, "A theoretical analysis of scattering loss from planar optical waveguides," *Optical and Quantum Electronics,* vol. 26, pp. 977-986, 1994.

[65]   T. Barwicz and H. A. Haus, "Three-dimensional analysis of scattering losses due to sidewall roughness in microphotonic waveguides," *Journal of Lightwave Technology,* vol. 23, pp. 2719-2732, 2005.

[66]   G. P. Christopher, K. Christian, F. Masafumi, P. Andreas, S. Thomas, *et al.*, "Radiation modes and roughness loss in high index-contrast waveguides," *Selected Topics in IEEE Journal of Quantum Electronics,* vol. 12, pp. 1306-1321, 2006.

[67]   M. E. Solmaz, D. B. Adams, S. Grover, W. C. Tan, X. Xia, *et al.*, "Compact Bends for achieving higher integration densities for LiNbO$_3$ waveguides," *IEEE Photonics Technology Letters,* vol. 21, pp. 557-559, 2009.

[68]   Q. Xu, B. Schmidt, S. Pradhan, and M. Lipson, "Micrometre-scale silicon electro-optic modulator," *Nature,* vol. 435, pp. 325-327, 2005.

[69]   M. Solmaz, R. Atkins, J. Gardner, and C. K. Madsen, "Vertically integrated As$_2$S$_3$ waveguides on lithium niobate waveguides," in *Proceedings of the SPIE on Infrared, Mid-IR, and Terahertz Technologies for Health and the Environment II*, Boston, MA, USA, 2007, pp. 676009-9.

[70]   K. T. Koai and P. L. Liu, "Modeling of Ti:LiNbO$_3$ waveguide devices. II. S-shaped channel waveguide bends," *Journal of Lightwave Technology,* vol. 7, pp. 1016-1022, 1989.

[71]   M. E. Solmaz, D. B. Adams, W. C. Tan, W. T. Snider, and C. K. Madsen, "Vertically integrated As$_2$S$_3$ ring resonator on LiNbO$_3$," *Opt. Lett.,* vol. 34, pp. 1735-1737, 2009.

[72]   R. V. Schmidt and I. P. Kaminow, "Metal-diffused optical waveguides in LiNbO$_3$," *Applied Physics Letters,* vol. 25, pp. 458-460, 1974.

[73]   W. Sohler, B. K. Das, D. Dey, S. Reza, H. Suche, *et al.*, "Erbium-doped lithium niobate waveguide lasers," *IEICE Trans Electron,* vol. E88-C, pp. 990-997, May 1, 2005 2005.

[74]   T. Kominato, Y. Hibino, and K. Onose, "Silica-based finesse-variable ring resonator," *IEEE Photonics Technology Letters ,* vol. 5, pp. 560-562, 1993.

[75]   B. E. Little, J. S. Foresi, G. Steinmeyer, E. R. Thoen, S. T. Chu, *et al.*, "Ultra-compact Si-SiO$_2$ microring resonator optical channel dropping filters," *IEEE Photonics Technology Letters,* vol. 10, pp. 549-551, 1998.

[76]   D. Rafizadeh, J. P. Zhang, S. C. Hagness, A. Taflove, K. A. Stair, *et al.*, "Waveguide-coupled AlGaAs / GaAs microcavity ring and disk resonators with high f inesse and 21.6-nm free spectral range," *Opt. Lett.,* vol. 22, pp. 1244-1246, 1997.

[77]   E. A. J. M. Bente, Y. Barbarin, J. H. den Besten, M. K. Smit, and J. J. M. Binsma, "Wavelength selection in an integrated multiwavelength ring laser," *IEEE Journal of Quantum Electronics,* vol. 40, pp. 1208-1216, 2004.

[78]   S. Yu, T. F. Krauss, and P. J. R. Laybourn, "Multiple output semiconductor ring lasers with high external quantum efficiency,", *IEE Proceedings-Optoelectronics,* vol. 144, pp. 19-22, 1997.

[79]   M.-S. Kwon and W. H. Steier, "Microring-resonator-based sensor measuring both the concentration and temperature of a solution," *Opt. Express,* vol. 16, pp. 9372-9377, 2008.

[80]   M. Sumetsky, R. S. Windeler, Y. Dulashko, and X. Fan, "Optical liquid ring resonator sensor," *Opt. Express,* vol. 15, pp. 14376-14381, 2007.

[81]   D. H. Jundt, "Temperature-dependent sellmeier equation for the index of refraction, n_e, in congruent lithium niobate," *Opt. Lett.,* vol. 22, pp. 1553-1555, 1997.

[82]   *FimmProp Manual*. Available: http://www.photond.com, 2009.

[83]   X.-H. Wang, *Finite element methods for nonlinear optical waveguides*. New York: Gordon and Breach, 1995.

[84]   M.-K. Chin, C.-W. Lee, and J. Shen, "Polarization-independent vertical coupler for photonics integration," *Opt. Express,* vol. 12, pp. 117-123, 2004.

VITA

Mehmet Ertugrul Solmaz received his Bachelor of Science degree in microelectronics from Sabanci University in Istanbul-Turkey in 2004. He was admitted to the Electrical and Computer Engineering Department of Texas A&M University in September 2004 and graduated in May 2010 with a Ph.D. degree. He is a proud photonics engineer and plans to pursue photonics related research in postdoctoral education and further along the road as a faculty member.

Dr. Solmaz may be reached at Texas A&M University, Electrical and Computer Engineering Department, College Station, TX, 77843-3128. His email is mesolmaz@gmail.com.